



**TÉCNICO**  
LISBOA

## **Additive Manufacturing of Metallic Implants**

**Miguel Ribeiro Pinto**

Thesis to obtain the Master of Science Degree in

### **Mechanical Engineering**

Supervisors: Prof. Maria Beatriz Cipriano de Jesus Silva

Dr. João Pedro Grossa Magrinho

#### **Examination Committee**

Chairperson: Prof. Rui Manuel dos Santos Oliveira Baptista

Supervisor: Dr. João Pedro Grossa Magrinho

Members of the Committee: Prof. Augusto Manuel Moura Moita de Deus

Prof. Maria de Fátima Reis Vaz

**November 2021**



## **Acknowledgements**

First and foremost, I would like to express my sincere gratitude towards my supervisors Professor Beatriz Silva and Doctor João Magrinho for an excellent guidance, transmission of knowledge and availability. Without your help and motivation, this challenge would have been much harder.

Additionally, I thank Professor Fátima Vaz with the help and knowledge on cellular materials and their applications.

Also, I thank Frederico Alves for always showing great availability on answering questions and clarifying any doubts in regard to Siemens NX software.

I want to thank to Doctor Pedro Lourenço and Engineer Luís Santos from the company Erofió, not only for the manufacturing of the specimens but also for the opportunity of visiting their industrial facilities.

At the same time, Engineer Nuno Fidelis has my thanks for the availability to visit Cenfimfe's installations.

A special thank you to all the people in the team PSEM for making me part of the accomplishment of building two incredible electric car prototypes.

I thank all my friends for their tireless support and understanding, specially to: José Lopes, João Cravidão, Filipe Alves and Diogo Roque.

Last but not least, the most special thank you is to my mother, father and brother that, even though I was far from home, never gave up or stopped encouraging me, and to my girlfriend Mariana for her patience and for always helping me when I most needed.



## **Resumo**

O número de fracturas em ossos está a aumentar todos os anos, devido ao aumento da obesidade e da esperança média de vida. O campo da engenharia de tecido ósseo tem vindo a desenvolver implantes de osso temporários feitos de metais biodegradáveis, nos quais a aplicação de estruturas treliçadas de ferro poderá vir a ser importante. Os recentes desenvolvimentos nas tecnologias de fabrico aditivo tornou o fabrico destas estruturas possível.

No trabalho desenvolvido na presente dissertação, um total de 5 topologias de células unitárias foram analisadas de forma a encontrar as que apresentavam propriedades mecânicas mais próximas do osso trabecular. Foram realizadas simulações numéricas em todas as topologias e as duas células unitárias que apresentavam as curvas tensão-extensão nominal mais próximas das do osso trabecular foram escolhidas para ser fabricadas: a cúbica (C) e a cúbica truncada (TC). Estas estruturas foram fabricadas através de fusão a laser em leito de pó (L-PBF) e foram testadas experimentalmente através de ensaios de compressão uniaxial, de forma a que os modelos numéricos pudessem ser avaliados em relação aos resultados experimentais.

A correlação entre os resultados numéricos e experimentais necessitou uma análise cuidada aos provetes obtidos por L-PBF que apresentaram algumas discrepâncias dimensionais entre as estruturas inicialmente desenhadas. Estas foram identificadas, medidas e realizaram-se novas simulações numéricas em modelos com dimensões mais próximas dos provetes.

Os resultados das novas simulações foram comparados com os resultados experimentais e verificou-se uma boa correlação entre os resultados, permitindo validar os modelos numéricos.

## **Palavras-Chave**

Implantes metálicos; Estruturas treliçadas; Fabrico Aditivo; Engenharia de tecido ósseo; Análise numérica

## **Abstract**

The number of bone fractures is increasing every year, due to the increasing life expectancy and obesity spread in the world. The bone tissue engineering field has been developing temporary bone implants made of biodegradable metals, in which the application of iron lattice structures could be very promising. Recent developments in the additive manufacturing technologies have also made possible the manufacturing of these structures.

Hence, in the present work, a total of five unit cell topologies were analysed in order to find the topology with the closest mechanical properties to the trabecular bone. Numerical simulations were performed on every topology and the two unit cell topologies that revealed to have the engineering curves closer to the trabecular bone were chosen to be manufactured: cubic (C) and truncated cube (TC). These lattice structures were manufactured by L-PBF and later experimentally tested by means of compression testing, so that the numerical models could be assessed against the experimental results.

The correlation between the numerical and experimental results required a careful analysis of the specimens obtained by L-PBF that revealed some geometric discrepancies between the initially designed structures. These discrepancies were identified and measured, and the numerical models were revised accordingly.

Finally, the numerical simulation results were compared with the experimental data and a good correlation was observed, validating the numerical models.

## **Keywords**

Metallic implants; Lattice structures; Additive Manufacturing; Bone tissue engineering; Numerical analysis

## Table of Contents

Acknowledgements.....	iii
Resumo .....	v
Abstract .....	vi
Table of Contents.....	vii
List of Figures .....	ix
List of Tables .....	xii
List of Symbols .....	xiii
Acronyms.....	xiv
1. Introduction .....	1
2. State of the Art .....	3
2.1. Cellular solids .....	3
2.1.1. Relative density.....	4
2.1.2. Bending- and stretch-dominated structures .....	5
2.1.3. Honeycombs and foams.....	8
2.1.4. Lattice structures.....	9
2.2. Biomedical environment.....	9
2.2.1. Bone properties.....	10
2.2.2. Bone implants .....	12
2.3. Biodegradable metals used for implants.....	14
2.3.1. Magnesium .....	15
2.3.2. Zinc.....	15
2.3.3. Iron.....	16
2.4. Additive Manufacturing .....	17
2.4.1. Generic AM process steps .....	18
2.4.2. Additive Manufacturing technologies .....	19
2.4.3. Comparison between AM processes for metals .....	21
2.4.4. Powder Bed Fusion manufacturing techniques .....	23
2.4.5. Manufacturability of metallic lattice structures using L-PBF .....	26
2.4.5.1. Basic design rules.....	26
2.4.5.2. Part orientation.....	28
2.4.5.3. PBF process parameters.....	32
2.4.6. Post processing of L-PBF components – hot isostatic pressing (HIP) .....	34
2.5. L-PBF applied to medical industry.....	35
3. Methodology .....	41
3.1. Unit cell design .....	41
3.2. Numerical Modelling .....	42
3.2.1. Element type selection .....	47
3.2.2. Relative density analysis .....	49
3.2.3. Topology analysis .....	52

3.3.	Experimental work .....	57
3.3.1.	Compression tests .....	59
4.	Results and discussion .....	61
4.1.	Numerical analysis of the full models .....	61
4.2.	Numerical analysis of the topologies .....	65
4.2.1.	Cubic and Truncated Cube topologies .....	65
4.2.2.	Truncated Octahedron, Rhombicuboctahedron and Rhombitruncated Cuboctahedron topologies .....	66
4.2.3.	Comparison with the trabecular bone .....	68
4.3.	Experimental work results .....	69
4.3.1.	Compression test specimens .....	69
4.3.2.	Compression tests results .....	71
4.3.3.	Experimental and numerical assessment .....	73
5.	Conclusions and Further work .....	77
5.1.	Conclusions .....	77
5.2.	Further work .....	78
	References .....	80
	Appendix A – Correction of the force-displacement experimental curves .....	86



## List of Figures

Figure 2.1 – (a) Typical cellular structure; (b) idealized open cell [18] .....	3
Figure 2.2 – (a) Open cell solid; (b) close cell solid [20] .....	4
Figure 2.3 – Design variables of a cellular material that influence its properties [18].....	4
Figure 2.4 – Distinction between cellular solid and solid with isolated pores [21].....	5
Figure 2.5 – (a) Bending-dominated structure; (b) and (c) stretch-dominated structures [19].....	6
Figure 2.6 – Typical compressive stress-strain curves for (a) stretch-dominated and (b) bending- dominated structure [19] .....	7
Figure 2.7 – Types of mechanical failure in cells: (a) bending of the struts; (b) collapse of the cell edges due to bending of the struts, typical of ductile materials; (c) collapse of the cell edges by elastic buckling, typical of elastomeric materials; (d) brittle fracture of the cell edges, typical of ceramics [18] .	7
Figure 2.8 – Examples of honeycombs: (a) aluminium; (b) paper-phenolic [17].....	8
Figure 2.9 – Open cell stochastic aluminium foams [24] .....	8
Figure 2.10 – Lattice structures with different cell units: (a) Kelvin/ Truncated Octahedron; (b) Rhombicuboctahedron; (c) Cubic [25] .....	9
Figure 2.11 – Cortical and trabecular bone [40] .....	10
Figure 2.12 – Typical stress-strain curve for cortical and trabecular bone under compression, adapted from [42] .....	11
Figure 2.13 – Illustration of the ideal relationship between mechanical integrity and corrosion of bone implants during the healing process [7] .....	13
Figure 2.14 – Necessary and sufficient conditions for being regarded as BM [63] .....	14
Figure 2.15 – Distribution of global AM market share by industries in 2017 [81].....	17
Figure 2.16 – Main steps for a general AM process, adapted from [85].....	18
Figure 2.17 – 7 families of AM: (a) Binder jetting; (b) Directed energy deposition; (c) Material extrusion; (d) Material jetting; (e) Powder bed fusion; (f) Sheet lamination; (g) Vat photopolymerization [87] .....	20
Figure 2.18 – Taxonomy of the current main metal AM processes [76] .....	21
Figure 2.19 – Comparison of strengths and weaknesses of metal AM processes [76].....	22
Figure 2.20 – Schematic illustration of a generic PBF process [19] .....	23
Figure 2.21 – Heating and melting phases in EBM [91].....	24
Figure 2.22 – Several scanning strategies used in PBF processes: (a) stripes; (b) islands; (c) countour only [93].....	25
Figure 2.23 – Different scanning strategies across several layers [95] .....	26
Figure 2.24 – Holes and internal channels basic rules to follow [79].....	26
Figure 2.25 – Ni718 manifold showing buckling effect [79].....	27
Figure 2.26 – Bike frame component showing buckling in a) and very high length-to-height ratio part in b) [79].....	27
Figure 2.27 – Schematic illustration of overhanging struts and support structures for metallic scaffolds [89] .....	28
Figure 2.28 – Build orientation of lattice structures in L-PBF [89] .....	28
Figure 2.29 – Overhang angle between build platform and part [79] .....	29
Figure 2.30 – Solution to avoid supports in case of 90° overhangs [79].....	29
Figure 2.31 – Impact of different part positions and orientations on support structures [79] .....	30
Figure 2.32 – Tree support and wall support designs for an impeller [79].....	30
Figure 2.33 – Typical surface defects on L-PBF fabricated parts [79].....	31
Figure 2.34 – Part distortion (left) and separation of the part from supports (right) [79].....	32
Figure 2.35 - Aluminium lattice structure [95].....	32
Figure 2.36 – Defects found in parts produced by L-PBF technology [79] .....	33
Figure 2.37 – Process parameters in L-PBF [19] .....	33
Figure 2.38 – Hot Isostatic Pressure: (1) as-built part by L-PBF; (2) pressure chamber; (3) herated gas [102] .....	35
Figure 2.39 – Process flow from patient's anatomical data acquisition to the final CAD model of the implant [103].....	36
Figure 2.40 – (a) CAD model of the surgical implant, based on CT-scan data; (b) biomodel and customized implant for craniofacial reconstruction surgery fabricated by L-PBF [104] .....	36

Figure 2.41 – (a) Hip implant manufactured by L-PBF; (b) micro CT-scan assessment of the implant lattice structure [9].....	37
Figure 2.42 – Reconstructions and 3D model of the metacarpophalangeal head of a (a) healthy control and (b) a RA patient, where the red circle marks the characteristic erosion in a RA patient; (c) sectional view of CAD model of the implant, where lattice internal structure is visible [105].....	38
Figure 2.43 – Iron lattice structure [60] .....	38
Figure 2.44 – Graded topological designs: (a) top view and longitudinal cross sections of CAD models of dense-in (left) and dense-out (right); (b) top view and longitudinal cross sections of micro- ..... CT reconstructions of the AM porous iron specimens, adapted from Li et al. [39] .....	39
Figure 3.1 – (a) enclosed pore by surrounding cells, (b) enclosed pore inside the cell [35].....	41
Figure 3.2 – Unit cells selected to be analysed: (a) cubic; (b) truncated octahedron; (c) truncated cube; (d) cuboctahedron; (e) rhombicuboctahedron; (f) rhombitruncated cuboctahedron.....	42
Figure 3.3 – Node 5866 selected to perform the convergence analysis on the effective stress .....	44
Figure 3.4 – Convergence analysis of the effective stress on node 5866 of C-0.57 .....	45
Figure 3.5 – CTETRA elements: (a) CTETRA4 and (b) CTETRA10 [110] .....	47
Figure 3.6 – Reaction force convergence analysis of the mesh with CTETRA4 elements.....	48
Figure 3.7 – Reaction force convergence analysis of the mesh with CTETRA10 elements.....	49
Figure 3.8 – Lattice structures used in the relative density analysis: (a) C-0.57; (b) C-0.64; (c) C-0.70 .....	49
Figure 3.9 – Relative density analysis compared to trabecular bone properties.....	51
Figure 3.10 – Lattice structures 2 x 2 x 2: (a) C–0.57; (b) TC–0.50; (c) TO–0.33; (d) RCO–0.28; (e) RTCO–0.33 .....	52
Figure 3.11 – Effective strain in the elements of the Mesh 3 of C-0.57 .....	53
Figure 3.12 – Effective strain in the elements of the Mesh 3 of TC-0.50.....	54
Figure 3.13 – Effective strain in the elements of the Mesh 7 of TO-0.33.....	55
Figure 3.14 – Effective strain in the elements of the Mesh 7 of RCO-0.28.....	56
Figure 3.16 – Effective strain in the elements of the Mesh 8 of RTCO-0.33.....	57
Figure 3.16 – Schematic illustration of a test specimen, according to ISO 13314:2011: (a) rectangular specimen and (b) cylindrical specimen [112] .....	58
Figure 3.17 – X Line 2000R from General Electrics [113] .....	58
Figure 3.18 – Hydraulic testing machine <i>Instron SATEC 1200</i> .....	60
Figure 4.1 – Mid planes where symmetry boundary conditions can be imposed, adapted from [115]..	62
Figure 4.2 – Illustration of the C-0.57 structures analysed: (a) full model; (b) half model; (c) quarter of a model .....	62
Figure 4.3 – Reaction force-displacement curves obtained from the full, half and quarter of a model .	63
Figure 4.4 – Convergence analysis of the effective stress on node 308633 of C-0.57 .....	64
Figure 4.5 – Convergence analysis of the reaction force in the C-0.57 lattice structure .....	65
Figure 4.6 – Effective strain in the elements of the lattice structure: (a) C-0.57 and (b) TC-0.50.....	66
Figure 4.7 – Effective strain in the elements of the lattice structure: (a) TO-0.33, (b) RCO-0.28 and (b) RTCO-0.33 .....	67
Figure 4.8 – Engineering curves from every topology compared to trabecular bone .....	68
Figure 4.9 – Test specimens: (a) Cubic specimens C1, C2 and C3; (b) Truncated cube specimens TC1, TC2 and TC3.....	69
Figure 4.10 – Specimens from the topologies selected: (a) cubic and (b) truncated cube .....	70
Figure 4.11 – Defects found on the lattice structure of topology: (a) C and (b) TC; (c) shows the average strut size measured for each topology.....	70
Figure 4.12 – Compression test specimens after being tested .....	71
Figure 4.13 – Experimental results for the compression tests of the cubic (C) specimens .....	72
Figure 4.14 – Experimental results for the compression tests of the truncated cube (TC) specimens .	72
Figure 4.15 – Comparison between numerical and experimental results for the C-0.57 lattice structure .....	73
Figure 4.16 – Comparison between numerical and experimental results for the TC-0.50 lattice structure .....	74
Figure 4.17 – Comparison between numerical and experimental results for the C-0.70 lattice structure .....	75
Figure A.1 – Displacement-force curve of the dry-run test.....	86

Figure A.2 – Force-displacement curve for specimen C1, with and without the correction of the displacement .....86

## List of Tables

Table 2.1 – Mechanical characteristics of human bone [43].....	11
Table 2.2 – Comparison between the biodegradable metals used for implants [66].....	15
Table 2.3 – Advantages and disadvantages of magnesium [66].....	15
Table 2.4 – Advantages and disadvantages of zinc [62,70].....	16
Table 2.5 – Advantages and disadvantages of iron [12,66].....	16
Table 2.6 – Main advantages and disadvantages of AM technology [82].....	18
Table 2.7 – Comparison between metal AM processes [66].....	22
Table 2.8 – L-PBF advantages and disadvantages [66].....	23
Table 2.9 – EB-PBF advantages and disadvantages [66].....	24
Table 2.10 – L-PBF vs E-PBF, adapted from [92].....	25
Table 2.11 – Standard roughness of parts made by L-PBF against conventional machining, adapted from [79].....	31
Table 2.12 – Effect of process parameters [99].....	34
Table 3.1 – Effective stress values obtained for the selected node 5866 through the several refinements of the topology C-0.57 and the associated relative error.....	45
Table 3.2 – Reaction Force values obtained for each iteration on the different meshes and relative error across the several refinements, along with the average relative error.....	46
Table 3.3 – Mesh with CTETRA4 characteristics and solving computation time.....	48
Table 3.4 – Mesh with CTETRA10 characteristics and solving computation time.....	48
Table 3.5 – Cubic unit cells and model characteristics for the preliminary relative density analysis.....	50
Table 3.6 – C-0.57 mesh characteristics and solving computation time.....	50
Table 3.7 – C-0.64 mesh characteristics and solving computation time.....	50
Table 3.8 – C-0.70 mesh characteristics and computation solving time.....	51
Table 3.9 – Comparison between Mesh 3 of each cubic topology.....	51
Table 3.10 – Unit cells and model characteristics for the preliminary topology analysis.....	53
Table 3.11 – TC-0.50 mesh characteristics and computation solving time.....	53
Table 3.12 – TO-0.33 mesh characteristics and computation solving time, (*) indicates solving times of simulations performed on the desktop PC.....	54
Table 3.13 – RCO-0.28 mesh characteristics and computation solving time, (*) indicates solving times of simulations performed on the desktop PC.....	55
Table 3.14 – RTCO-0.33 mesh characteristics and computation solving time, (*) indicates solving times of simulations performed on the desktop PC.....	56
Table 3.15 – Summary of the chosen mesh characteristics for each topology and computation solving times, .....(*) indicates solving times of simulations performed on the desktop PC.....	57
Table 3.16 – Main characteristics of the X Line 2000R from General Electric [113].....	58
Table 3.17 – Manufacturing parameters for the specimens [113].....	59
Table 4.1 – Unit cells and model characteristics for the full model analysis.....	61
Table 4.2 – Mesh characteristics and computation solving time for the full, half and quarter of model, (*) indicates solving times of simulations performed on the desktop PC.....	63
Table 4.3 – C-0.57 mesh characteristics and computation solving time, (*) indicates solving times of simulations performed on the desktop PC.....	64
Table 4.4 – Effective stress values obtained for the selected node 308633 through the refinements of the quarter of the full lattice structure C-0.57 and the associated relative error.....	64
Table 4.5 – C-0.57 and TC-0.50 mesh characteristics and computation solving times, (*) indicates solving times of simulations performed on the desktop PC.....	66
Table 4.6 – TO-0.33, RCO-0.28 and RTCO-0.33 mesh characteristics and computation solving times, (*) indicates solving times of simulations performed on the desktop PC.....	67
Table 5.1 – Comparison between designed strut dimensions and the struts from the specimens.....	70
Table 5.2 – Displacement performed in each of the specimens.....	71
Table 5.3 – Mesh characteristics and computation solving time for coarser meshes using 316 stainless steel, (*) indicates solving times of simulations performed on the desktop PC.....	73
Table 5.4 – C-0.70 mesh characteristics and computation solving time, (*) indicates solving times of simulations performed on the desktop PC.....	75

## List of Symbols

### Latin Symbols

$b$	Number of struts in a unit cell
$E$	Energy density
$h$	Hatch spacing
$j$	Number of frictionless joints in a unit cell
$M$	Maxwell number
$M_S$	Solid mass
$p$	Porosity
$P$	Laser power
$t$	Layer thickness
$\bar{t}$	Average specimen's strut dimension
$v$	Scan speed
$V_S$	Solid volume
$V_T$	Total volume

### Greek Symbols

$\bar{\epsilon}$	Effective strain (von Mises strain)
$\rho_s$	Density of the base material (solid)
$\rho^*$	Density of the cellular material
$\bar{\rho}$	Relative density
$\sigma_Y$	Yield strength of the material
$\bar{\sigma}$	Effective stress (von Mises stress)
$\Delta\bar{\sigma}$	Relative error across meshes

## Acronyms

2D	Two-Dimensional
3D	Three-Dimensional
3DP	3D Printing
3SP	Scan, Spin and Selectively Photocure
AM	Additive Manufacturing
ASTM	American Society for Testing and Materials
BC	Boundary Condition
BJ	Binder Jetting
BM	Biodegradable Metal
BTE	Bone Tissue Engineering
CAD	Computer-Aided Design
CAE	Computer Aided Engineering
CAGR	Compound Annual Growth Rate
CLIP	Continuous Liquid Interface Production
CNC	Computer Numerical Control
CT	Computer Tomography
DED	Directed Energy Deposition
DLP	Digital Light Processing
DMLS	Direct Metal Laser Sintering
EBM	Electron Beam Melting
EB-PBF	Electron Beam Powder Bed Fusion
FDM	Fused Deposition Modelling
FEA	Finite Element Analysis
FEM	Finite Element Method
FFF	Fused Filament Fabrication
HIP	Hot Isostatic Pressing
LENS	Laser Engineered Net Shaping
LMD	Laser Metal Deposition
LOM	Laminated Object Manufacture

L-PBF	Laser Powder Bed Fusion
MJF	Multi-Jet Fusion
MJM	Multi-Jet Modeling
MRI	Magnetic Resonance Imaging
OA	Osteoarthritis
PBF	Powder Bed Fusion
RA	Rheumatoid arthritis
SCP	Smooth Curvature Printing
SDL	Selective Deposition Lamination
SHS	Selective Heat Sintering
SLA	Stereolithography Apparatus
SLM	Selective Laser Melting
SLS	Selective Laser Sintering
SM	Subtractive Manufacturing
STL	Standard Tessellation Language
THA	Total Hip Arthroplasty
TOPS	Topologically Ordered Porous Structure
TOPS	Topologically Ordered Porous Structures
UAM	Ultrasonic Additive Manufacturing
WAAM	Wire + Arc Additive Manufacturing





## 1. Introduction

The number of bone fractures is increasing everyday due to a number of reasons [1], such as the continuous increase in life expectancy in the world [2] and the spread of obesity [3]. According to the international osteoporosis foundation, more than 8.9 million bone fractures occur every year and, it is estimated that around 2050, hip fractures will have increased by 310% and 240% for men and women, respectively, when compared with rates of 1990 [1]. Due to this reason and the fact that when a bone fracture reaches a critical size, the body and the bone lose the ability to completely heal on its own [4], and medical treatment is required for a full recovery.

One of the most recent and emergent areas of study that is now being used for bone regeneration, is bone tissue engineering (BTE). This new biomedical field applies principles of engineering and sciences to develop methods to synthesize and/or regenerate bones, such as the development of orthopaedic bone implants [5,6]. These are divided into two groups: permanent joint replacements and temporary fracture fixation devices. Currently, there is particular interest in the application of temporary bone implants in such a way that during the healing period they maintain their mechanical integrity, while progressively corroding and allowing to be replaced by the growing tissue, so that by the end of healing process the implant has been completely absorbed by the body [7]. This could overcome several limitations of permanent implants, such as chronic inflammation, physical irritation, stress shielding and even, the possibility to avoid the need of a second surgical procedure to remove the implant [5,8].

Lattice structures are 3D cellular materials that show promising potential in the biomedical sector because of their permeable porous structures that, contrarily to fully dense (bulk) metallic implants, allow the flow of fluids through their structure, which can not only result in improved osseointegration, but also reduce stress shielding [9,10].

For this type of application, there have been proposed degradable biomaterials from the families of polymers, ceramics and metals [8]. Biodegradable polymers have been widely accepted as very suitable, due to their degradability, biocompatibility and ease of processability. However, alongside ceramic materials, polymers' poor mechanical properties restrict their application in load-bearing implants for BTE. For this reason, there is growing interest in the use of biodegradable metals for biomedical applications and, currently, a great part of the research is focused on the development of biodegradable metal implants [7].

The most studied biodegradable metals are magnesium (Mg), zinc (Zn) and iron (Fe) [11]. Among these, Mg has the best biocompatibility, its mechanical properties are the closest to human bone but its corrosion rate is too high; Zn has a corrosion rate close to ideal for biodegradable applications but low mechanical properties; and Fe has the highest mechanical strength, is the easiest to manufacture but has a corrosion rate too low [12].

The use of iron lattice structures in temporary bone implant applications could put together the best qualities of each. The porosity of lattice structures could not only accelerate the degradation rate of the iron, due to the increase in surface area, but also lower the mechanical properties of the iron to

match those of bone, avoiding problems such as stress shielding, which is caused by an uneven load distribution across the bone due to the larger stiffness of the implant when compared to the bone [13,14].

The manufacturing of these type of structures in metal is not possible by any conventional method, due to their complexity [15]. Only recent developments in additive manufacturing (AM) techniques have made it possible [16], by technologies such as laser powder bed fusion (L-PBF) and electron beam powder bed fusion (EB-PBF).

The aim of this dissertation is to mechanically evaluate which iron open cell lattice structure topology has the closest mechanical properties to the trabecular bone. For this, finite element analysis (FEA) and experimental compression tests were performed.

The present dissertation is structured as follows:

Chapter 1 introduces the motivation and objectives of this dissertation, by highlighting the current increase in bone fractures and importance of developing biodegradable iron implants.

Chapter 2 is the state of the art, which begins by introducing the concept of cellular solids, their most important mechanical properties and their categories. Afterwards, the properties of the bone are presented along with the main characteristics that bone implants should have for better bone regeneration applications, diving particularly on the application of biodegradable metal implants, giving special attention to iron. After this, an extensive research on the additive manufacturing (AM) technology is presented, with particular focus on powder bed fusion (PBF) processes and the manufacturability aspect of iron lattice structures by this technology. Finally, a literature review is done on the application of metal bone implants with lattice structures fabricated by laser powder bed fusion (L-PBF) on the biomedical industry.

Chapter 3 corresponds to the methodology, where an overview on the materials and methods is given, including the unit cell topology selection, some preliminary numerical simulations for the determination of some parameters and the selection of the ideal element size for the generation of the mesh for each topology. The experimental work is also described.

In Chapter 4 the results of the numerical simulations of the several topologies are presented, followed by a comparison with the trabecular bone. The choice of the topologies for the experimental specimens is justified, the experimental results are presented, and the validation of the numerical model is discussed.

At last, in Chapter 5, conclusions about the work performed on this dissertation are described and some remarks on further research are also presented.

## 2. State of the Art

In this chapter, an explanation on what cellular solids are and their classification is given, along with their characteristic mechanical properties, and with particular interest in lattice structures. After that, the importance of bone implants in bone regeneration applications is explained, as well as the advantages in the use of biodegradable metals in bone implants, especially iron. An overview on the current development of AM technologies is given, diving deep trying to find the most suitable AM process to fabricate iron lattice structures, which is L-PBF. Lastly, a literature review is done on the application of L-PBF to fabricate lattice structures with biomedical applications, finishing in the current development on iron lattices produced by L-PBF.

### 2.1. Cellular solids

A cellular solid is “one made up of an interconnected network of solid struts or plates which form the edges and faces of cells” [17], which simply put, means an assembly of cells with solid edges or faces, packed together to fill space; and can be more easily understood as foams and lattices [18]. These kind of structures, shown in Figure 2.1 (a), are created when an isotropic compact solid material is converted into another with an anisotropic foam-like structure [15] and are quite common in nature, such as in wood, cork, sponge and even cancellous bone [18]. An example of what an idealized cell look like is shown in Figure 2.1 (b).

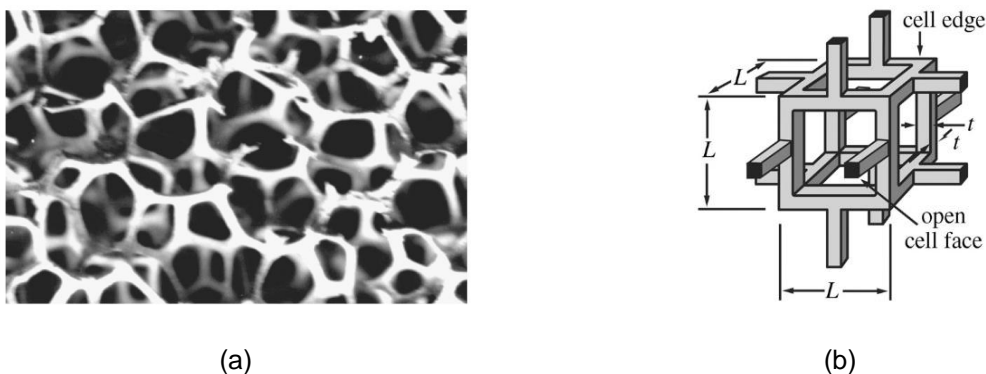


Figure 2.1 – (a) Typical cellular structure; (b) idealized open cell [18]

This type of materials has the ability to behave as structures on the small scale while behaving as homogeneous materials when the macroscopic scale is considered, meaning that there is a length-scale separation between the lattice and the macroscopic scales. As a consequence of this, their macroscopic behaviour can be described in terms of effective homogeneous properties – like an effective elastic modulus – that are highly dependent on the base material and on the small scale unit cell design parameters [19].

Cellular materials can be classified, accordingly to their cells, into two-dimensional (2D) and three-dimensional (3D): 2D cellular materials comprise the honeycombs and the 3D ones involve foams and lattices. In three dimensions there is also a distinction between open cell solids, that allow

interconnection between the cells through their open faces - Figure 2.2 (a) - and close cell when the faces of the cells are closed, sealing off the connection between cells [17] - Figure 2.2 (b).

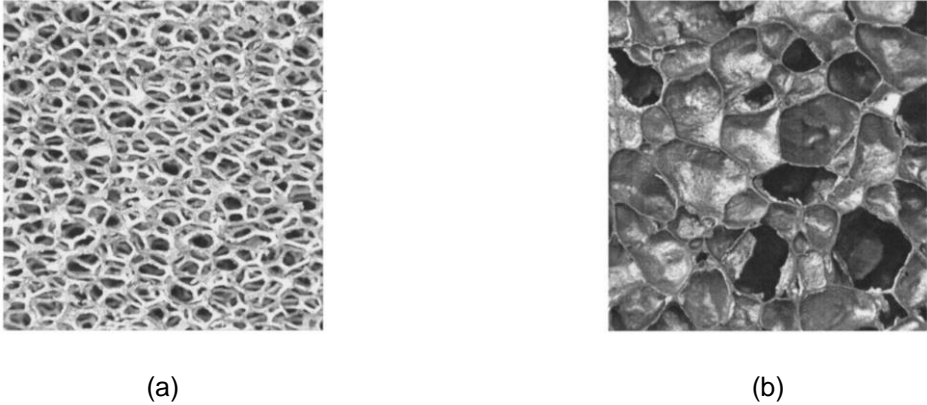


Figure 2.2 – (a) Open cell solid; (b) close cell solid [20]

Properties of cellular materials are mainly influenced by three factors [18], shown in Figure 2.3:

- 1) Properties of the base material;
- 2) Topology and shape of the cell edges and faces;
- 3) Relative density of the foam.

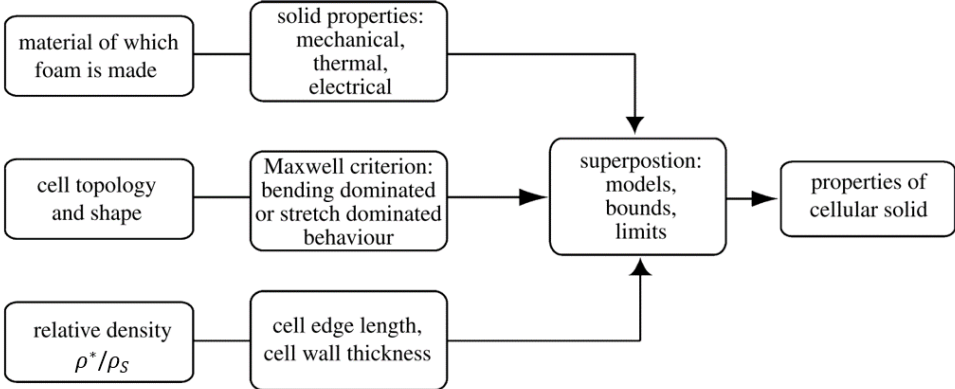


Figure 2.3 – Design variables of a cellular material that influence its properties [18]

**2.1.1. Relative density**

Relative density ( $\bar{\rho}$ ) is the single most important parameter of cellular materials, to which any property can be related to. It is defined as the ratio between the density of the cellular material  $\rho^*$  to the density of the base material (solid)  $\rho_S$  [17]:

$$\bar{\rho} = \frac{\rho^*}{\rho_S} \tag{2.1}$$

Simply put, relative density essentially defines how much solid material is present in the overall volume occupied by the cellular material, therefore it is a volume fraction of a solid and, according to Gibson [21], can also be calculated using a ratio of volumes:

$$\bar{\rho} = \frac{\rho^*}{\rho_s} = \frac{M_s}{V_T} \cdot \frac{V_s}{M_s} = \frac{V_s}{V_T} \quad (2.2)$$

where  $M$  and  $V$  stand for mass and volume, respectively; while subscripts  $S$  and  $T$  mean solid and total, respectively.

The fraction of pore space in the foam that is complement to unit of the relative density is its porosity ( $p$ ), calculated as [17]:

$$p = 1 - \bar{\rho} \quad (2.3)$$

Furthermore, cellular solids are cellular structures that have a relative density less than 0.3, while structures with higher values than 0.8 are considered as solids with isolated pores [21], as seen in Figure 2.4, below.



Figure 2.4 – Distinction between cellular solid and solid with isolated pores [21]

At first, one may suppose that cell size should also be an important parameter (and actually, it can be), but cell shape and topology is a much more important parameter on defining the cellular material properties, as will be explained further [18].

### 2.1.2. Bending- and stretch-dominated structures

According to Ashby [18], the classification of a unit cell as a bending- or a stretch-dominated structure is a very useful criterion that allows to predict the mechanical behaviour of these cellular materials when subjected to loads. In a brief way, when the struts of a unit cell with rigid connected joints bend as a result of an external load, the structure is defined as bending-dominated – Figure 2.5 (a); if on the contrary, the struts are mainly loaded axially with some experiencing tensile forces when the connection in the joints is rigid, the structure is defined as stretch-dominated – Figure 2.5 (b) and (c). Another way of looking at it is by imagining if the rigid junctions between the struts was replaced with pins: when compressed, the bending-dominated structure – Figure 2.5 (a) – becomes a mechanism because it collapses due to rotation of the struts about the joints, while stretch-dominated structures – Figure 2.5 (b) and (c) – simply becomes a truss frame.

This classification can be expressed mathematically using the Maxwell's stability criterion [22], which is a simple and important theory about rigidity – “the condition for a pin-jointed frame (meaning one that is hinged at its joint) made up of  $b$  struts and  $j$  frictionless joints, like those in Figure 2.5, to be

both statically and kinematically determinate (meaning that it is rigid and does not fold up when loaded) is“ [18], in two dimensions and three dimensions represented by Equations (2.4) and (2.5), respectively:

$$M = b - 2j + 3 \quad (2D) \tag{2.4}$$

$$M = b - 3j + 6 \quad (3D) \tag{2.5}$$

where  $M$  is the Maxwell number.

According to this criterion, the mechanical behaviour of a given structure can be predicted: if  $M < 0$ , as in Figure 2.5 (a), the frame is a mechanism, thus a bending-dominated structure; while if  $M \geq 0$ , as in Figure 2.5 (b) and (c), the frame ceases to be a mechanism, becoming a stretch-dominated structure when subjected to load [18].

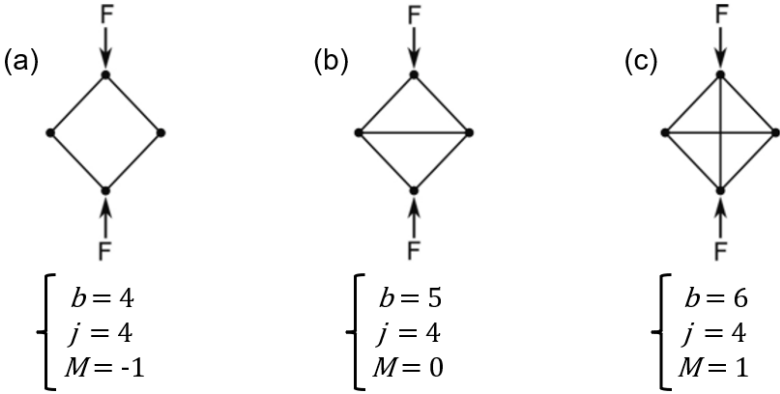


Figure 2.5 – (a) Bending-dominated structure; (b) and (c) stretch-dominated structures [19]

Generally speaking, stretch-dominated structures have a much higher structural efficiency than bending-dominated structures, since the struts from the former are almost exclusively loaded axially (either in tension or compression) and slender structures are much stiffer when stretched than when bent. Ashby [18] also states that for a given mass, stretch-dominated structures are extremely stiff and strong, while although bending-dominated structures have less stiffness and are not as strong, they are able to absorb energy very well when compressed.

The mechanical behaviour from each type of structure can be understood by observing their compression stress-strain curves, in Figure 2.6. Both curves can be divided into three parts: a linear elastic regime (1), which lasts until the struts yield either due to bending or stretching – Figure 2.7 (a) and (b); a plateau regime (2), during which the cells progressively start to collapse because of buckling, brittle crushing or yielding – Figure 2.7 (c) and (d) – mainly depending on the base material and unit cell shape; and lastly, the densification phase (3), which corresponds to the geometric effect of opposite sides of the cells being forced against each other and further bending or buckling are not possible, which causes a strain induced increase in relative density [18,19].

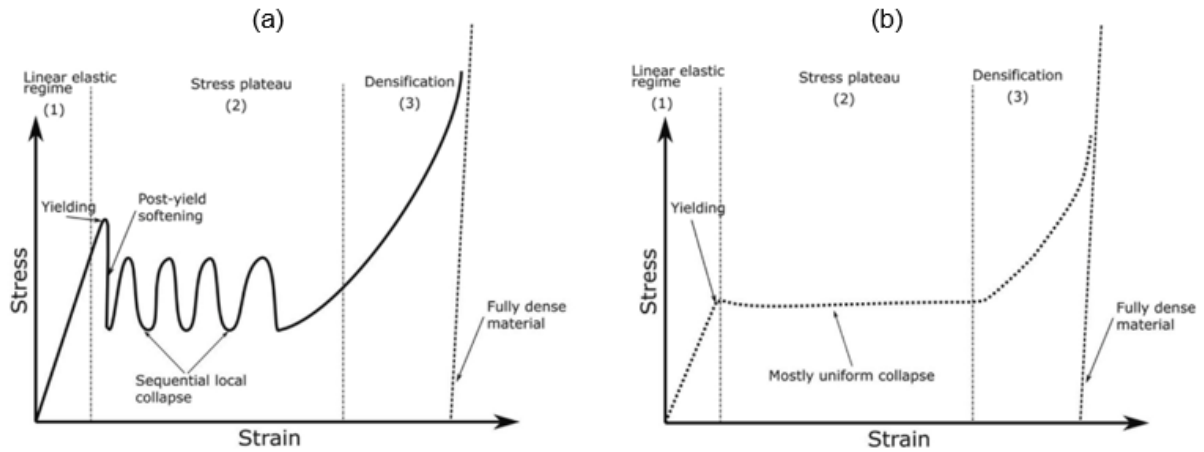


Figure 2.6 – Typical compressive stress-strain curves for (a) stretch-dominated and (b) bending-dominated structure [19]

As can be seen in Figure 2.6, stress-strain curves of stretch-dominated structures are typically characterized by higher initial stiffness and yield strength than a bending-dominated structure of the same mass. Post-yield softening can also be observed due to sudden failure by buckling or brittle crushing of a layer of cells, while the successive peaks and valleys during the plateau consist in the progressive failure of the other layers. This means that although stretch-dominated structures may be stiffer and stronger, they are prone to sudden failures and are not the most suitable to absorb deformation energy. In opposition to this, bending-dominated structures have a much softer transition from the linear elastic regime to the plateau, which is long and flat due to the bending of the struts and thus, much more reliable at dissipating deformation (or absorbing) energy [18].

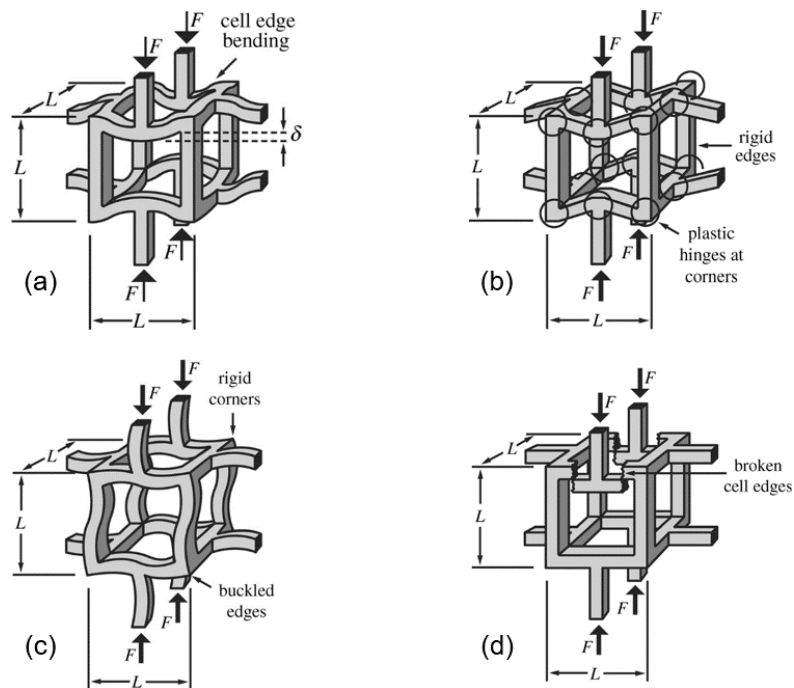


Figure 2.7 – Types of mechanical failure in cells: (a) bending of the struts; (b) collapse of the cell edges due to bending of the struts, typical of ductile materials; (c) collapse of the cell edges by elastic buckling, typical of elastomeric materials; (d) brittle fracture of the cell edges, typical of ceramics [18]

Summarizing, stretch-dominated structures have very high stiffness and strength, while bending-dominated have low stiffness and strength but provide good energy absorption.

**2.1.3. Honeycombs and foams**

Honeycombs are the simplest cellular materials and owe their name to the way their structures resemble honeycombs built by honeybees. These structures consist in a 2D array of polygons which pack to fill a plane area, just like the hexagon cells of the bee [17]. This type of materials has been applied to several different fields, such as aerospace industry as a core of sandwich panels and in automobile industry as efficient impact attenuators, due to their high strength parallel to their cell walls and energy absorption properties, in conjunction with their lightweight structure [23]. They are a prime choice as cores for sandwich panels and most of them are made of aluminium and polymers and are formed by periodic hexagonal cellular structures [15], as can be seen in Figure 2.8.

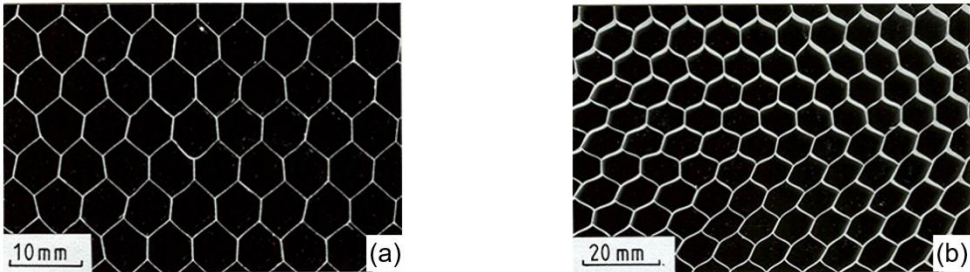


Figure 2.8 – Examples of honeycombs: (a) aluminium; (b) paper-phenolic [17]

Foams are 3D cellular materials that have, in general, a non-periodic or random (stochastic) structure (as can be seen in Figure 2.9), which is also their main drawback. Because they are generally obtained by a manufacturing process that allows a very limited control on the cell size and cell-wall thickness [19], their structure is very heterogeneous, being strong in some places and weak in others, while the weaker regions end up dragging down both stiffness and strength. Therefore, it is very hard to achieve control over the mechanical and biological properties of these materials.

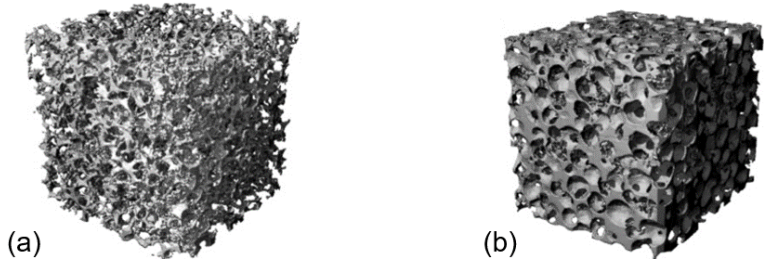


Figure 2.9 – Open cell stochastic aluminium foams [24]

Ashby [18] stated that most foams, whether their cells are open or closed, show a bending-dominated mechanical behaviour when subjected to loads, which means that their strength and stiffness fall far below the levels that would be expected of a stretch-dominated structure, at a given density. Although, besides these properties, foams have the ability to accommodate large strains, which make them suitable for applications such as in cushioning, packaging and energy absorbing.



#### 2.1.4. Lattice structures

Lattice structures are 3D cellular materials that have a well determined periodic geometry that is obtained by continuously repeating unit cells connected to each other. This type of geometry is completely determined by a small number of design parameters, such as strut dimensions, relative density and unit cell shape or topology, for example Kelvin in Figure 2.10 (a), Rhombicuboctahedron in Figure 2.10 (b) and Cubic in Figure 2.10 (c).

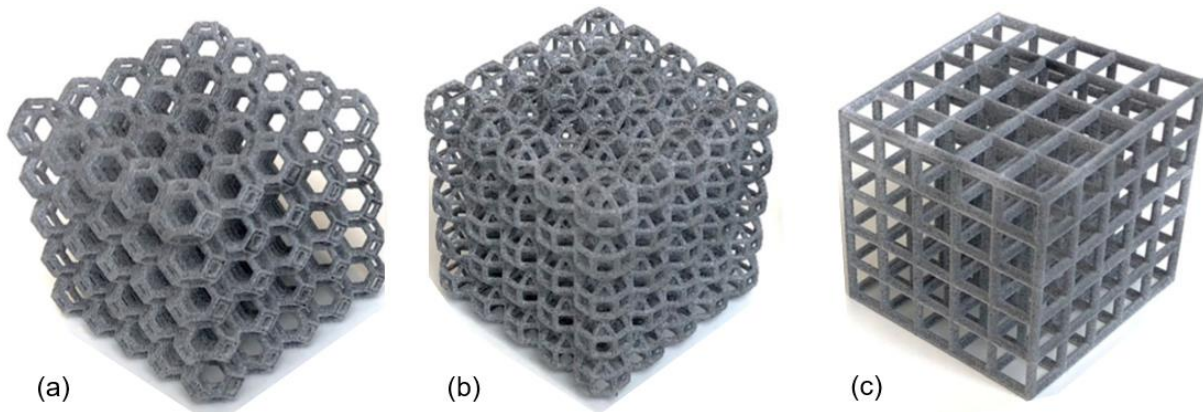


Figure 2.10 – Lattice structures with different cell units: (a) Kelvin/ Truncated Octahedron; (b) Rhombicuboctahedron; (c) Cubic [25]

In this way, having a more controllable structure opens the possibility to better control its mechanical properties, which ideally allows to specifically tailor them for each application needs. This is why lattice structures are also often called architected cellular materials or topologically ordered porous structures (TOPS), especially when they are formed by struts and nodes. By only changing the geometry or topology of the unit cell [26,27], the strut dimensions and orientation [27,28], or even the relative density [17,27], while keeping the same material, it is possible to obtain mechanical properties in a range of far extremes, such as stiffness, strength, permeability, etc [19].

Contrarily to foams, lattice structures have a well determined periodic geometry that cannot be obtained by the usual manufacturing processes used in foams or by any conventional method, due to their complexity [15]. Only recent developments in AM technologies have made the production of complex topologies that were not feasible by conventional methods possible [16], as will be further explained in section 2.4.

This type of structures shows promising potential in the biomedical sector because, when compared to fully dense (bulk) metallic implants, orthopaedic prostheses with a porous structure that is permeable and allows the flow of fluids (open cell lattice structures) can result in improved osseointegration and reduced stress shielding [9,10], concepts that will be explored further in the next section.

## 2.2. Biomedical environment

The increase in life expectancy in the world (and consequent aging of the population) [2,8] together with the spread of obesity [3] and lack of calcium [29], are some of the reasons that are causing the number of bone fractures to be increasing each year [1]. According to the international osteoporosis

foundation, more than 8.9 million bone fractures occur every year around the world. Furthermore, it is estimated that, around 2050, hip fractures will increase by 310% and 240% for men and women, respectively, when compared with rates of 1990 [1].

Bones' remarkable self-healing capabilities are very well known [30], however when a defect reaches a critical size (around 25mm) the body loses the ability to completely heal on its own [4,31] and, usually, additional medical treatment is required to achieve full recovery. For instance, if a defect is located in a place where the bone has load-bearing responsibilities, bone grafts with initial strong or, at least, bone-like mechanical properties are required to repair the damage [32,33]. But, in the end, the treatment of the bone defect is highly dependent on the patient's age, health and the size and location of the damaged tissue [32].

There are several treatments used for bone regeneration, such as: autografts (which is the best choice, nowadays [34]), in which bone is taken from the same person's body; allografts, in which bone tissue is taken from a living or a deceased donor (other than the patient); and, most recently, the emergence of bone tissue engineering (BTE), that applies principles of engineering and sciences to develop methods to synthesize and/or regenerate bone (like bone implants), which restore, maintain or improve this tissue's functions *in vivo* [5,6,35]. The successful application of BTE can avoid the major drawbacks related to the other treatment options: in the autograft technique there is a supply limitation, risk of donor passing away in the process, the resorption is variable, high rate of failure in specific body locations and the need of a second surgery; while problems associated with allografts are the transmission of pathogens and the possibility of rejection by the recipient's body [36,37].

### 2.2.1. Bone properties

Bone is a natural composite material that contains about 45-60% minerals, 20-30% matrix and 10-20% water, by weight [38]. Every human bone shows a gradual change in porosity from a compact outer shell to a more spongy and airy inner layer [39], which allows to identify the two different structures in what the bone consists: cortical and trabecular bone, shown in Figure 2.11.

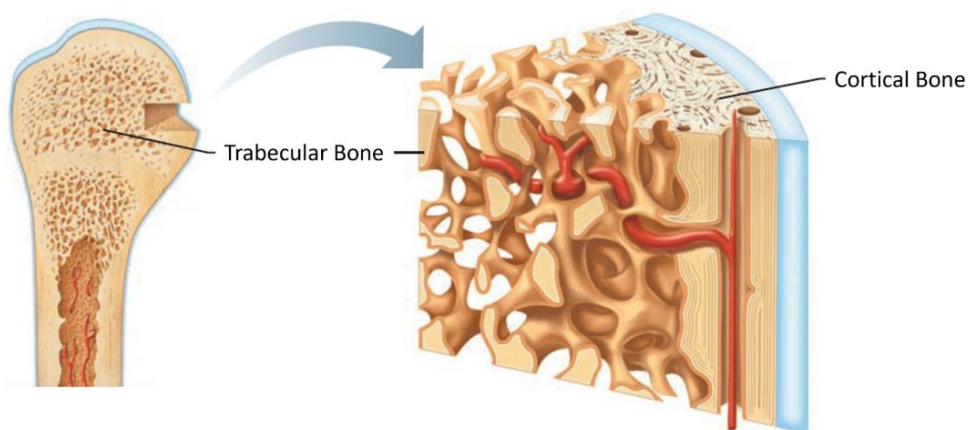


Figure 2.11 – Cortical and trabecular bone [40]

Cortical bone, also known as compact or dense bone, is the dense outer layer of the bone and has around less than 10% porosity, whereas for trabecular bone, also known as cancellous or spongy bone, corresponds to the inner part of the bone and has a porous cellular structure in which the porosity usually ranges between 50-90 [6]. This difference can be measured in terms of apparent density, which corresponds to the mass of the bone divided by the bulk volume of the test specimen including. The cortical bone has an apparent density equal to  $1.85 \text{ g/cm}^3$ , while in the trabecular bone the value ranges between  $0.1$  and  $1.0 \text{ g/cm}^3$  [41]. This property has a great influence on the compressive stress-strain behaviour, as can be seen in Figure 2.12.

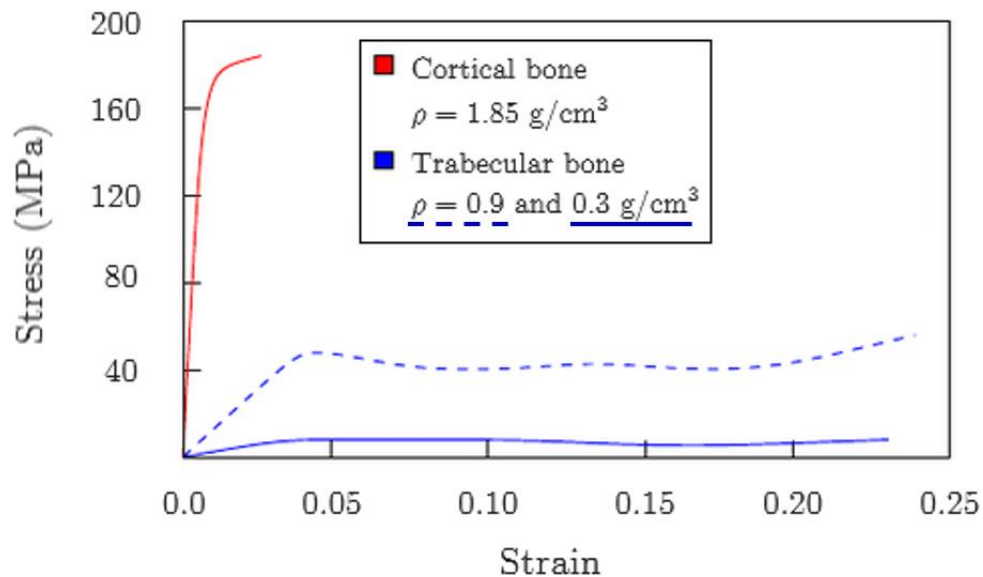


Figure 2.12 – Typical stress-strain curve for cortical and trabecular bone under compression, adapted from [42]

A summary of the bone properties is shown on Table 2.1, below.

Table 2.1 – Mechanical characteristics of human bone [43]

<b>Cortical bone</b>			
Density [ $\text{g/cm}^3$ ]	~1.5–2		
Porosity [%]	~3–12		
	Load direction	Strength [MPa]	Modulus of elasticity [MPa]
Compressive properties	Longitudinal	~190–245	~14–28
	Transverse	~30–170	–
Tensile properties	Longitudinal	~130–190	~7–25
	Transverse	~40–60	–
<b>Trabecular bone</b>			
Density [ $\text{g/cm}^3$ ]	0.2–0.6		
Porosity [%]	~30–95		
	Strength [MPa]		Modulus of elasticity [MPa]
Compressive properties	~1–12		~0.1–0.4
Tensile properties	~ 2		~6–14

### 2.2.2. Bone implants

Since the occurrence of bone fractures is increasing, as already mentioned above, in order to improve patient's quality of life, the development of reliable bone implants is now more important than ever before. So, to meet the requirements of each patient and provide the best bone implants to repair bones with load-bearing functionalities, there are some major characteristics they should present:

1. Full anatomical match with the complex morphology of the damaged bone [44,45];
2. Mechanical properties close to the bone tissue intended to regenerate, so that stress shielding issues may be avoided [46–48]. Stress shielding is a phenomenon that is caused by an uneven load distribution across the bone due to the larger stiffness of the implant with respect to that of the adjacent bone. The resultant lack of biomechanical stimulation for bone remodelling leads to bone resorption and consequent implant loosening [13,14,49];
3. Biodegradable properties, in such a way that the implant has the ability to retain the necessary mechanical support functions during the whole regeneration process (from the implant deterioration till the bone recovery) [7,50], decrease the chance of infection and also reduce the chance of a new surgery [51];
4. Biocompatible properties, which correspond to the ability of the implant being able to be in contact with human tissues without causing any unacceptable degree of harm to the body, meaning that it should be non-toxic and also have a positive effect when interacting with living cells, preventing undesirable infections [52,53]. Osteoinductive and osteoconductive properties that promote the formation of bone are also appreciated [5];
5. A topological design or material, for instance, that promote the nutrient exchange and vascularization, stimulating bone regeneration (like open cell lattices with interconnected pores) [44,54].

Orthopaedic bone implants are mostly used for structural reinforcement, as an artificial bone, and are divided into two groups: permanent joint replacements, such as hip, knee, ankle, shoulder, elbow, wrist and finger joints, which are expected to last in patient body throughout the rest of their life span; and temporary fracture fixation devices, which include plates, screws, pins, wires and intramedullary nails used to fix broken or fractured bones, and should last just long enough to let bones heal [55]. Although there is extensive research on materials used in load-bearing and permanent implants, the same is not true for temporary implants.

Ideally, any bone implant should maintain its mechanical integrity during the necessary healing period, while progressively corroding and allowing to be replaced by the growing tissue [7,8], as in the representation shown in Figure 2.13.

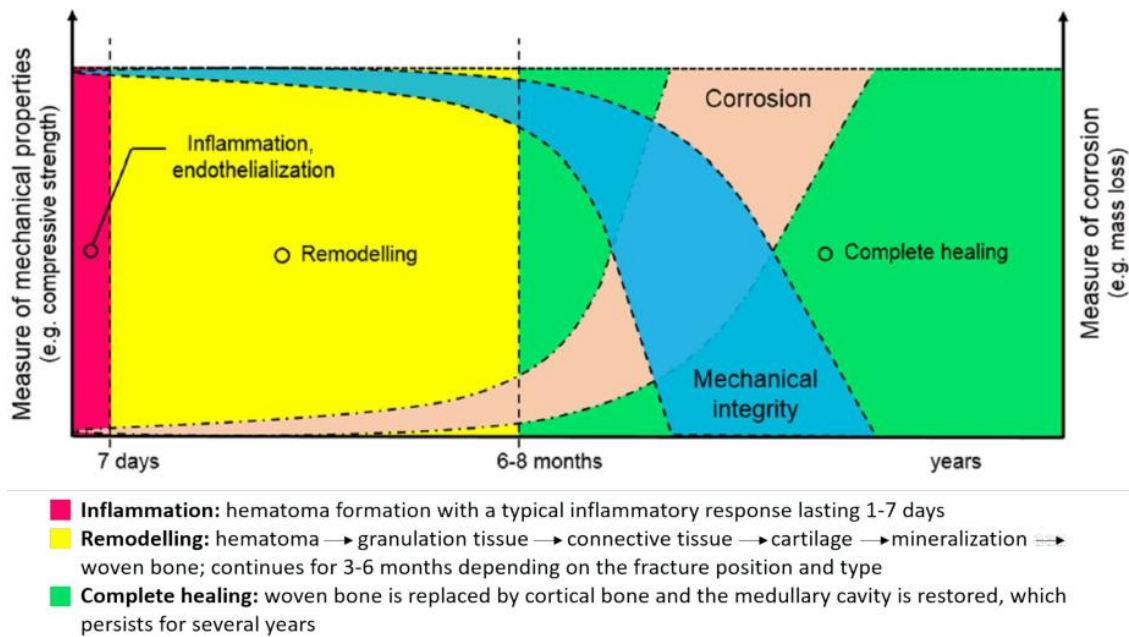


Figure 2.13 – Illustration of the ideal relationship between mechanical integrity and corrosion of bone implants during the healing process [7]

The areas of bone regeneration and temporary body implants are continuously evolving, and a development of special interest is the employment of degradable materials in human implants. It has been found that in certain applications degradable implants can overcome many limitations of permanent devices, such as prolonged physical irritation, thrombus formation, chronic inflammation, stress shielding, long-term migration of the implant or lack of integration into the host tissue, and second surgical procedure to remove the implant (common with non-degradable implants), which can bring health wise benefits for the patients, as well as holding economic advantages [5,8,56].

The study of innovative degradable biomaterials is very interesting and materials from the families of polymers, ceramics, and metals have been proposed [8]. Biodegradable polymers have been widely used and accepted as one of the most suitable materials for scaffolds due to their degradability, biocompatibility and ease of processability. However, alongside ceramic foams, polymers' poor mechanical properties restricted their applications in bone tissue engineering, as they could not achieve the sufficient level of required strength to match bone properties. On the contrary, the inherent high strength, high wear resistance, high ductility and ability to absorb high strain energy owned by metals, make them very suitable for BTE applications such as joint replacement, bone plates, screws, among others [11,12,57,58].

For this reason, there is growing interest in the use of biodegradable metals for biomedical applications and, currently, most of the research is focused on the development of biodegradable metal implants [7]. This development is a complex problem because it combines engineering and medical requirements [59], in such a way that the degradation parameters need to be carefully controlled for the material to be completely degraded and resorbed in the appropriate amount of time, just like it was shown in Figure 2.13.

### 2.3. Biodegradable metals used for implants

Biodegradable metals (BMs) have gained a lot of importance in the area of bone tissue engineering, mainly due to their mechanical and biodegradable properties that allow *in vivo* degradation, where the degradation products are metabolised and assimilated by the cells and/or tissues [60–62]. The definition of “biodegradable metals” is identical to that of “absorbable metallic materials” in ASTM-F3160 and, according to that definition, only metals or alloys with both 100% biodegradability and biocompatibility are eligible as potential biodegradable metals, regardless of mechanical support, as can be seen in Figure 2.14 [63]. Therefore, the introduction of these metals has, in some way, led to a change of paradigm in the field of metal implants from preventing corrosion to its direct application [7].

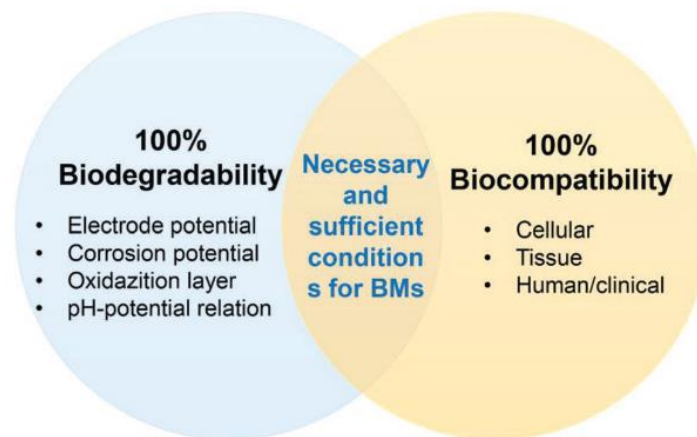


Figure 2.14 – Necessary and sufficient conditions for being regarded as BM [63]

Thus, BMs constitute a new class of biomaterials mainly intended for temporary medical implants applications [7], such as in human tissues/organs that have the ability to regenerate themselves, like bones. Unlike nondegradable metals, which are a better choice for teeth and joints that do not have self-healing capabilities and are suitable for permanent medical implants applications [64]. In this way, biodegradable metal implants are expected to completely degrade in the human body after the tissue healing process is successfully completed [65], which will avoid the need of a second surgery when working as temporary implants, reducing costs and patients' pain [62].

Bone grafting is a field of study where nondegradable metals like titanium (Ti) alloys have been used and the introduction of BMs would make a great impact. Despite the remarkable regenerative capabilities of the bone in response to mechanical stimuli, larger complicated defects can delay or impair the healing process and require external help to promote bone repair [5]. Although Ti alloy implants can withstand the load, transfer some mechanical stimuli to the bone and promote bone growth, they cannot be absorbed and may end up becoming barriers to the complete reconstruction of the bone. Consequently, biodegradation is considered a necessary feature for optimal bone grafting, not only because the degradation itself provides space for bone growth but it also increases bioactivity [64].

The most studied biodegradable metals are magnesium (Mg), zinc (Zn) and iron (Fe) [11]. Among these, Mg has the best biocompatibility and its mechanical properties are the closest to human bone as a bulk metal; Zn has a corrosion rate close to ideal for biodegradable applications, falling

between that of Mg and Fe; and Fe has the highest mechanical strength and is the easiest to manufacture [12]. A comparison between some of the characteristics of these materials is presented in Table 2.2, below.

Table 2.2 – Comparison between the biodegradable metals used for implants [66]

<b>Characteristics</b>	<b>Mg</b>	<b>Zn</b>	<b>Iron</b>
Melting Point (°C)	650	420	1150–1600
Yield Strength (MPa)	≈ 150	50–120	130
Tensile Strength (MPa)	≈ 250	100–200	350
Elastic Modulus (GPa)	≈ 40	≈ 100	200
Vickers Hardness (HV)	100	30	30-80
Corrosion Resistance	Poor	Good	Good
Biocompatibility	Excellent	Good	Good

### 2.3.1. Magnesium

Magnesium (Mg) is a light metal that has a relatively high mechanical strength, possibly replacing aluminium in some applications [66]. However, even though its very high corrosion rate in physiological environments may reduce its potential use in some implants [67], it makes it a suitable choice for magnesium-based biodegradable materials, which could make a second surgery for implant removal unnecessary, as mentioned before. The main advantages and disadvantages of magnesium are presented in Table 2.3.

Table 2.3 – Advantages and disadvantages of magnesium [66]

<b>Advantages</b>	<b>Disadvantages</b>
Low density	Flammable
Good machinability	Poor corrosion resistance
Light weight	High cost
Excellent in vivo compatibility	Low elastic modulus
Fully bioresorbable	Moderate strength

Although magnesium scaffolds have been manufactured for bone regeneration [68], there are two mainly processing challenges for their fabrication using AM processes: severe evaporation and high chemical reactivity [64], which are triggered when high thermal energy is applied during the melting phase of the process, resulting in high porosity parts. These manufacturing difficulties added to the fact that the degradation rate is faster than the healing rate of the host tissue [65,69], resulting in rapid loss of mechanical strength, makes them mostly unsuitable for scaffold applications [12].

### 2.3.2. Zinc

Zinc (Zn) is a very important trace element in the human body and is often used in industry for surface treatment of steel. In the medical field, it has been used in cardiovascular stents and dental



implants, for instance [66]. By alloying elements, such as Mg, Ca, Sr, Li, and Cu, it is possible to increase the strength of zinc [70]. The main advantages and disadvantages of Zn are presented in Table 2.4.

Table 2.4 – Advantages and disadvantages of zinc [62,70]

<b>Advantages</b>	<b>Disadvantages</b>
Accuracy	Low toughness
High impact strength	Brittle
Durable	
Cost-effective	
Fully bioresorbable	
Good biocompatibility	

Although the corrosion rate may be close to ideal for zinc and its alloys, although their high density and poor mechanical properties may be improved by alloying other elements, Zn has a much higher evaporation tendency than Mg, resulting in severe spatter and porosity during laser welding [71]. In this way, it is easy to understand that the evaporation is even more severe when dealing with long-time lasting laser melting, as in AM fabrication [64], which reveals to be a very big challenge and fair to assume that is, for now, unsuitable for scaffold applications when manufactured by AM processes, just like magnesium.

### 2.3.3. Iron

Iron (Fe) is the most common element on the planet by mass, as well as in the human body [66]. Fe shows good biocompatibility and has better mechanical properties than the other biodegradable metals considered (Mg and Zn). However, the degradation rate has revealed to be too slow and its elastic modulus is too high when compared to the human bone. This large difference in stiffness is prone to promote the occurrence of stress shielding effects when iron is used on implants [72].

In this way, the current research on Fe-based biodegradable metals is mainly focused on three objectives: acceleration of the degradation rate; enhancing the mechanical properties; and improving biocompatibility [62]. The main advantages and disadvantages of Fe are presented in Table 2.5.

Table 2.5 – Advantages and disadvantages of iron [12,66]

<b>Advantages</b>	<b>Disadvantages</b>
High ductility	Slow degradation rate
Easy to manufacture	Too high stiffness
Good weldability	

One of the solutions that was found to be suitable to increase the degradation rate of iron without undermining its biocompatibility and mechanical properties was the use of alloying elements such as manganese, palladium, silver, phosphorous and silicon [73]. However, the stiffness of the developed iron-based materials was still too high. Another solution that could overcome these disadvantages is the fabrication of porous structures, which can not only increase the degradation rate due to its increased



surface area but also decrease the stiffness of the parts [72]. For instance, iron porous structures with porosities in the range of 45.6-86.9% lower the compressive modulus to the range of 218-854 MPa, which is now comparable with the values in trabecular bone [12].

Currently, literature on porous iron as a scaffold material is still very limited [74] and with the development of AM technologies it has become possible to manufacture metal lattice structures. Iron does not have the problems of evaporation that either Mg and Zn have, which makes it a much more suitable material to be processed by these technologies and later be used as a temporary implant.

## 2.4. Additive Manufacturing

Industry is currently undergoing the 4<sup>th</sup> Industrial Revolution, which is described as the digitalization of the manufacturing sector and involves some key characteristics, such as cyber-physical systems and market-places, smart robots and machines, the use of big data, among others [75]. One of the main technologies of this revolution is additive manufacturing (AM), which started by creating plastic prototypes for engineers and designers [76].

Additive manufacturing (AM), which is also known as 3D printing, rapid prototyping or free-form fabrication, is the “process of joining materials to make parts from 3D model data, usually layer upon layer, as opposed to subtractive manufacturing and formative manufacturing methodologies”, according to the standard ISO/ASTM 52900:2015 [77]. In this way, as AM is based on the general principle of successive addition of material, it becomes possible to reduce or even eliminate tooling processes, which promises to reduce part cost not only by reducing material waste but also by enabling short production cycles [78,79].

According to the 2021 AMPOWER report [80], the overall metal and polymer material AM market was valued at EUR 7.17 billion in 2020 and is expected to grow at an average rate of 20% every year until 2025 (CAGR), which makes up to a EUR 17.83 billion market valuation in 2025. Different AM technologies have now been used in various industrial sectors and the increasing use of 3D printed parts in the medical sector over the recent years translates as it being the 5<sup>th</sup> most important in the world, representing 11% of the total market share, according to the Wohlers report of 2017 [81], and is shown in Figure 2.15.

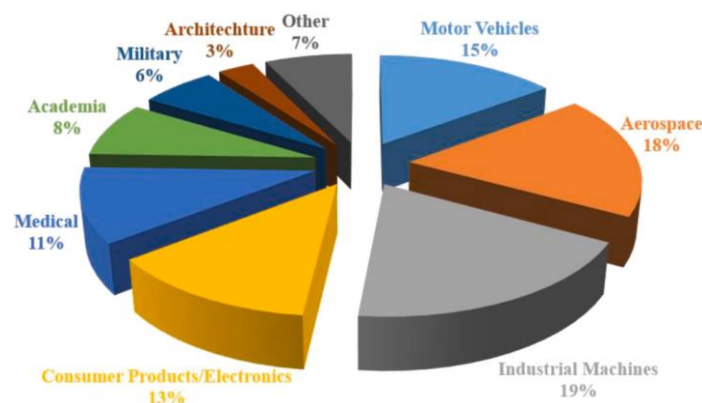


Figure 2.15 – Distribution of global AM market share by industries in 2017 [81]

The main features of this manufacturing process are referred in Table 2.6.

Table 2.6 – Main advantages and disadvantages of AM technology [82]

Advantages	Disadvantages
<ul style="list-style-type: none"> <li>• Production cost minimization</li> <li>• Nearly net shape production</li> <li>• Production of unique and complex shapes (design freedom)</li> <li>• Reduced part assembly necessity</li> <li>• Material waste minimisation</li> <li>• Short time to market (reduced lead time)</li> <li>• Tooling and fixturing elimination</li> <li>• Reduced scrap</li> </ul>	<ul style="list-style-type: none"> <li>• High first time buy cost of AM equipment, material and software</li> <li>• Low reliability regarding mass production</li> <li>• Lack of global certifications and standardisations</li> <li>• Limited component size and building volume</li> <li>• Low production speed compared to subtractive manufacturing processes</li> <li>• Costly for high-volume production</li> <li>• Limited material option</li> <li>• Metallurgical defects, e.g. porosity and hot cracking</li> <li>• Unsatisfactory dimensional accuracy</li> </ul>

#### 2.4.1. Generic AM process steps

The fabrication of a component by AM technologies follows 7 main steps [79,83–85], shown in Figure 2.16. Each step is described below.



Figure 2.16 – Main steps for a general AM process, adapted from [85]

1. 3D-Modeling: a 3D model of the part is created using CAD software or by reverse engineering, using a 3D object scanner;
2. STL file creation/ conversion: CAD model is converted to a STL file that describes the external closed surfaces of the original model (tessellation, which constitutes the basis for the calculation of the slices);
3. STL transfer to AM machine and manipulation: STL file is transferred to the AM machine and then to a slicing software, where part orientation and support structures are defined, as well as the slicing of the model into digital slices;
4. Machine Setup: Consumables are loaded and build parameters, such as power, scanning speed and layer thickness, are defined;
5. Build: Production of the parts layer by layer and generation of control data;
6. Part removal: part and its support structures are removed from the build platform;
7. Post processing: once taken out of the build platform, parts may require machining, support structures to be removed, polishing or even heat treatment before they are ready to use.

#### 2.4.2. Additive Manufacturing technologies

According to the standard ISO/ASTM 52900:2015 [77], the classification of AM processes is structured in 7 major additive manufacturing families. Below are the definitions, with reference to the typical materials used in each one of them and some alternative nomenclature that is still used [77,86]:

1. **Binder Jetting (BJ)**: a liquid bonding agent is selectively deposited to join powder materials across several layers – Figure 2.17 (a) → polymers, metals and ceramics (powders). Binders include organic and inorganic materials.  
Alternative nomenclature: 3D Printing (3DP); ExOne; Voxeljet.
2. **Directed Energy Deposition (DED)**: focused thermal energy (laser, electron beam or an electric arc) is used to fuse material by melting as the material is being deposited – Figure 2.17 (b) → metals (wire or powder).  
Alternative nomenclature: Laser Metal Deposition (LMD); Laser Engineered Net Shaping (LENS).
3. **Material Extrusion**: the material is selectively dispensed through a nozzle or orifice – Figure 2.17 (c) → polymers and metal filled polymers (wire).  
Alternative nomenclature: Fused Filament Fabrication (FFF); Fused Deposition Modeling (FDM).
4. **Material Jetting**: droplets of build material are selectively deposited – Figure 2.17 (d) → polymers (including photopolymers and waxes).  
Alternative nomenclature: Polyjet; Projet; Smooth Curvatures Printing (SCP); Multi-Jet Modeling (MJM).
5. **Powder Bed Fusion (PBF)**: thermal energy (laser or electron beam) selectively fuses regions of a powder bed – Figure 2.17 (e) → polymers, metals and ceramics (powders).

Alternative nomenclature: Selective Laser Sintering (SLS); Direct Metal Laser Sintering (DMLS); Selective Laser Melting (SLM); Electron Beam Melting (EBM); Selective Heat Sintering (SHS); Multi-Jet Fusion (MJF).

6. **Sheet lamination:** sheets of material are stacked and laminated to form an object – Figure 2.17 (f) → polymers (paper and plastic sheets) and metals (metal foils/tapes).

Alternative nomenclature: Laminated Object Manufacture (LOM); Selective Deposition Lamination (SDL); Ultrasonic Additive Manufacturing (UAM).

7. **Vat photopolymerization:** liquid photopolymer in a vat is selectively cured by light-activated polymerization – Figure 2.17 (g) → UV-curable photopolymer resins.

Alternative nomenclature: Stereolithography Apparatus (SLA); Digital Light Processing (DLP); Scan, Spin and Selectively Photocure (3SP); Continuous Liquid Interface Production (CLIP).

Besides these 7 families, it should be noted that there is also a concept of hybrid additive manufacturing, where an AM process (usually, DED) is combined with CNC machining, which allows to merge the additive and subtractive processes into a single machine that can optimize the advantages of both processes. An example of this concept is the AMBIT deposition system, by Hybrid Manufacturing Technologies [86] and another is the Large Additive/Subtractive Integrated Modular Machine (LASIM) project, which aimed to combine Wire + Arc Additive Manufacturing (WAAM) with other processes such as machining, in-line NDT and cold-working [76]. From now on, only the standard names will be used so that it becomes easier to follow and avoid confusion.

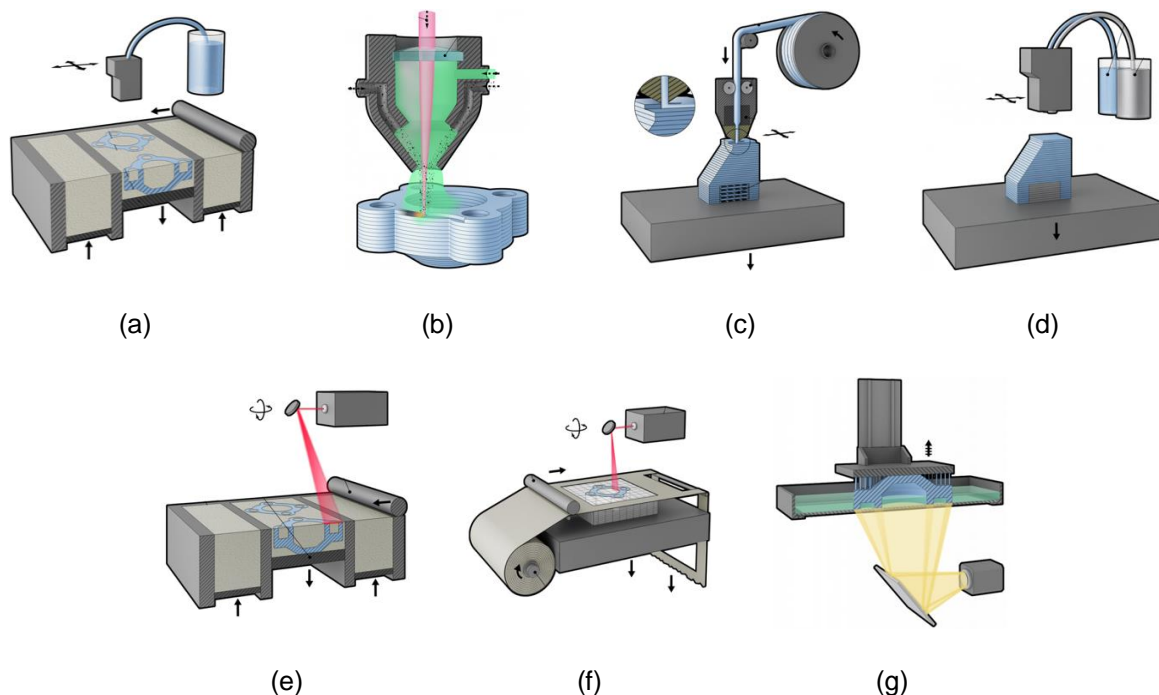


Figure 2.17 – 7 families of AM: (a) Binder jetting; (b) Directed energy deposition; (c) Material extrusion; (d) Material jetting; (e) Powder bed fusion; (f) Sheet lamination; (g) Vat photopolymerization [87]

Among the above-mentioned standardized AM families and as can be partially seen on Figure 2.18, the ones that have the ability and are most suited to process metals are the following: binder jetting (BJ), powder bed fusion (PBF) – which includes laser powder bed fusion (L-PBF) and electron beam powder bed fusion (EB-PBF), directed energy deposition (DED) and material extrusion with metal filled polymers, by material extrusion [66].

To execute an AM process and with particular focus on metal, three main constituents are required [78]:

- **Heat source** – mainly borrowed from the welding world, can be power beams (laser or electron) or electric arcs from welding torches, or even the combination of both.
- **Raw material** – currently, powder or wire is fed into the system.
- **Manipulator** – the motion system that traces the tool path defined for each layer, which can be CNC gantries, robotic arms, amongst others.

The choice available in each of these constituents and their combination allows the creation of a wide range of metal AM processes. In Figure 2.18 are shown the combinations that resulted in the most relevant AM technologies that have in sight the production of metal parts, which include processes from both the PBF (Selective Laser Melting and Electron Beam Melting) and DED (Direct Laser Fabrication, Sciaky and Wire+Arc Additive Manufacturing) families.

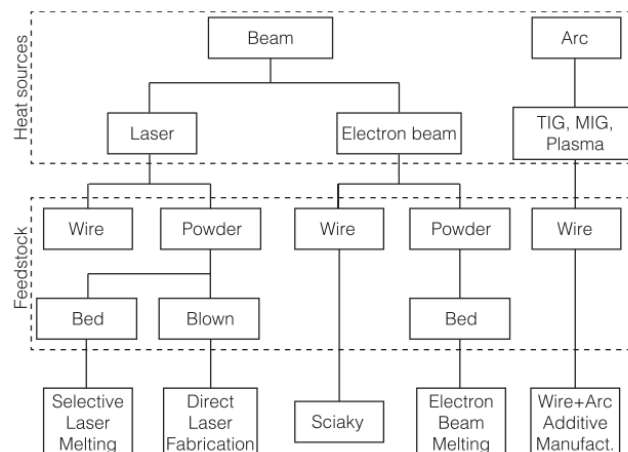


Figure 2.18 – Taxonomy of the current main metal AM processes [76]

### 2.4.3. Comparison between AM processes for metals

Before deciding on an AM process several factors must be taken into account, since all of them have their own distinct characteristics, strengths and weaknesses that make them naturally more suitable for certain applications and, generally, do not directly compete against each other. For instance, arc-based techniques are not capable of manufacturing small size features but are the ideal choice for building large components, as opposed to PBF, that although may allow the production of very complex geometries, the need of a controlled atmosphere to prevent oxidation and powder contamination, does not allow very large parts to be manufactured [78].

A comparison between some of the characteristics of different AM techniques that should be considered while deciding on which AM technique might be better for a desired application are presented in Table 2.7.

Table 2.7 – Comparison between metal AM processes [66]

Characteristic	BJ	L-PBF	EB-PBF	DED	Material extrusion
Parts complexity	Average	Complex	Average	Simple	Simple
Resolution	High	High	Average	Low	Low
Productivity	High	High	Average	Low	Low
Surface finish	High	Average	Average	Poor	Poor
Mechanical properties	Average	High	Average	Average	Poor
Printing speed	Fast	Low	Average	Average	Average
Porosity	High	Minimal	Average	High	Minimal
Accuracy	Low	High	High	High	Low
Corrosion resistance	Low	High	High	Average	Average

As already mentioned before, among the processes present in Table 2.7, the most suited and relevant to the production of metal parts are the ones that belong to the PBF and DED families. A more visual and intuitive comparison between these two families can easily be seen in the spider diagram below, Figure 2.19.

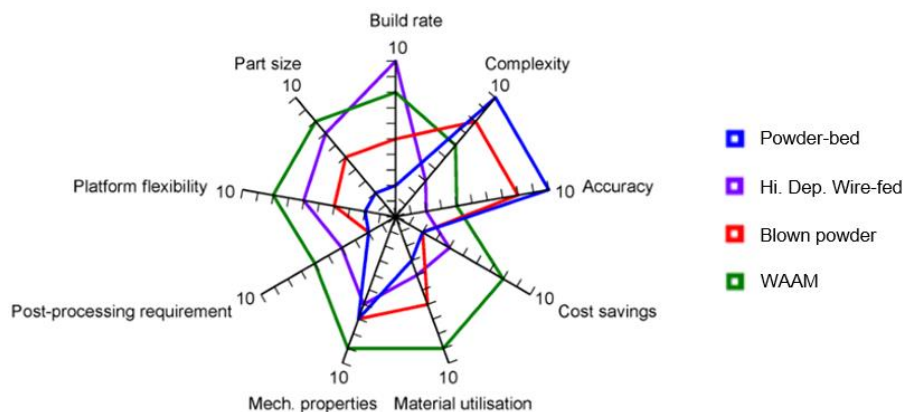


Figure 2.19 – Comparison of strengths and weaknesses of metal AM processes [76]

Most metallic parts that are used in the medical sector have complex shapes and in many cases porous structures are used, since these promote the fixation in the body by means of osseointegration [66]. Therefore, by looking at Figure 2.19 one can understand why 90% of metallic cellular materials have been fabricated using powder bed fusion [88], as it is the technique that allows the most complexity and accuracy of all AM processes. Considering how complex lattice structures are and the supporting role of the powder bed during the fabrication process, PBF techniques have been receiving the most of the attention from the research community as well as the most engineering work in this field [19]. As the

objective of this work is to fabricate metallic (iron) lattice structures, the PBF processes are the most suitable and will be further analysed.

#### 2.4.4. Powder Bed Fusion manufacturing techniques

As stated before, PBF is an AM process in which a heat source is used to melt and fuse selective regions of pre-placed metal powder on a bed [76]. Depending on its primary heat source, PBF processes can be divided into two main categories [19]: laser PBF (L-PBF) and electron beam PBF (EB-PBF).

L-PBF process takes place within an inert atmosphere chamber, using argon or nitrogen as shielding gas, for instance. The process begins by spreading a thin layer of the metal powder on the bed. Then, a focused laser beam is used to melt and fuse the metallic powders of one layer together. Afterwards, the build platform is lowered in the Z direction by a predetermined thickness and the process is repeated again until the required part is completely built [19,66,89]. A schematic illustration of a PBF process can be seen in Figure 2.20.

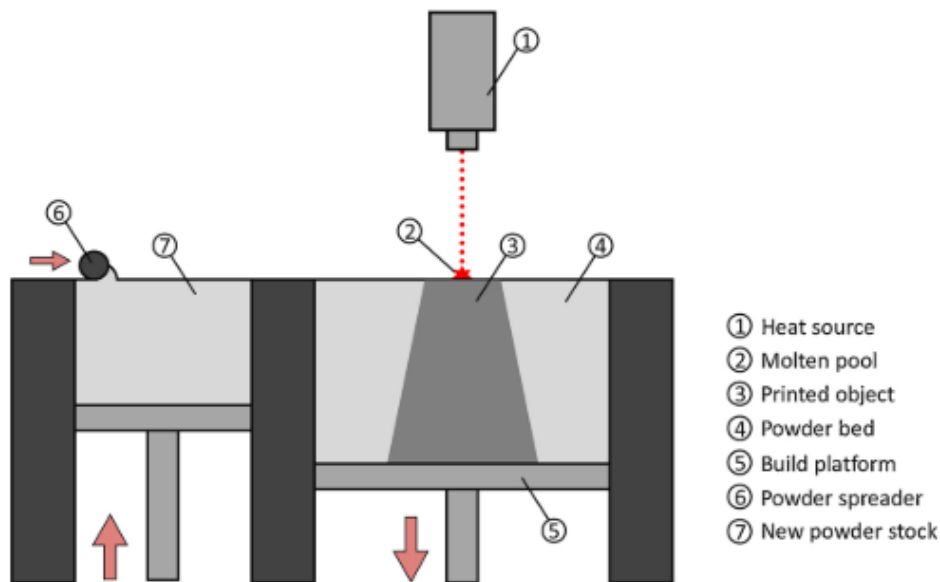


Figure 2.20 – Schematic illustration of a generic PBF process [19]

The main advantages and disadvantages of L-PBF are shown in Table 2.8, below.

Table 2.8 – L-PBF advantages and disadvantages [66]

Advantages	Disadvantages
Medium productivity	High price
Very complex shapes (thin walls, hidden holes, porous structures)	Corrosion sensitive
Excellent mechanical properties of the 3D object	Lower scan speed than EBM
Good repeatability	Parts have stresses that require a post heat treatment
Medium to high surface quality	It requires build structures because of the weight of the metallic parts and distortion at high temperature



Although ideal materials to process are pure metals, other alloys can also be used in L-PBF, such as stainless steel, CoCr alloys, titanium alloys and aluminium [90].

EB-PBF uses a similar sequence of steps to L-PBF but with an electron beam as the heat source and also, instead of within an inert chamber, this process takes place in a high vacuum atmosphere chamber at very high temperatures. Besides these, the main difference to L-PBF in the sequence of steps is that EB-PBF includes a two-step sequence for each layer [19]. First, each layer of powder is heated – Figure 2.21 (a) – by scanning the electron beam several times across the layer, in order to slightly sinter the powder particles to prevent instabilities, such as electro-static charging and repulsion of the powder particles; after this, the region defined by the slice geometry is melted using an additional pass. This melting phase is usually completed by hatching, where the direction of the beam changes in each line and layer by layer by 90°, see Figure 2.21 (b). In order to enhance the surface quality a strategy called quasi-multi-beam is also employed, where the contours of each layer are molten quasi simultaneously, see Figure 2.21 (c) [91]. Due to each layer of powder being sintered, faster scanning speeds are usually allowed in EB-PBF.

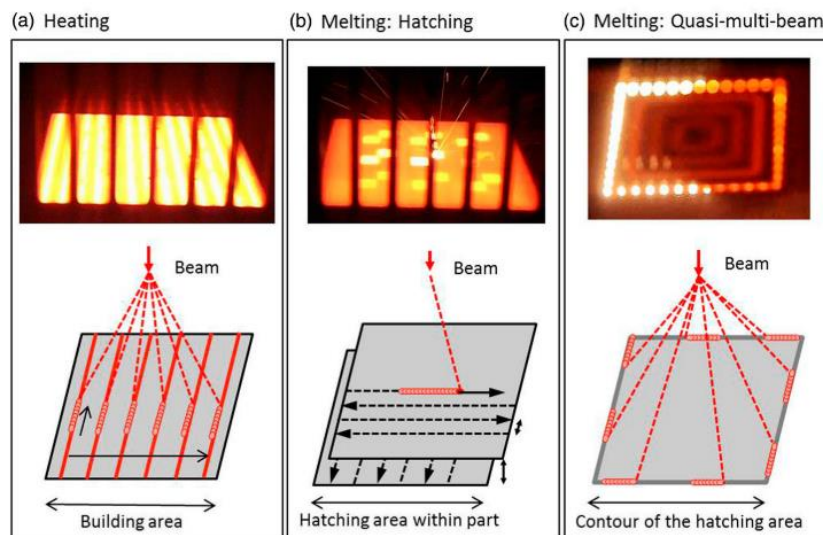


Figure 2.21 – Heating and melting phases in EBM [91]

The main advantages and disadvantages of EB-PBF can be seen in Table 2.9, below.

Table 2.9 – EB-PBF advantages and disadvantages [66]

Advantages	Disadvantages
<ul style="list-style-type: none"> <li>Possibility of working at elevated temperatures</li> <li>Better protection against contamination</li> <li>Low level of residual stresses</li> <li>Absence of shrinkage, no thermal post-processing</li> <li>Freedom of design, because of fewer supports</li> <li>Allows stacking parts and obtaining meshes</li> </ul>	<ul style="list-style-type: none"> <li>High fatigue</li> <li>Danger for electrostatic charge of the powder</li> <li>Only conductive alloys can be obtained</li> <li>Rough finish the requires polishing (depending on process conditions)</li> </ul>



Materials frequently employed in this process include titanium alloys, CoCr alloys, stainless steel and Inconel [90].

A critical understanding of the capabilities and limitations of each of these two techniques is essential to select the right process for a target application. A comparison between the process parameters of both PBF processes is summarized in Table 2.10.

Table 2.10 – L-PBF vs E-PBF, adapted from [92]

Process parameter	L-PBF	EB-PBF
Energy source	Laser beam	Electron beam
Pre-heating (°C)	Up to 250	Up to 1100
Processing atmosphere	Protective gas (Argon or Nitrogen)	Vacuum (supported by Helium)
Powder size (µm)	15 – 45	45 – 105
Layer thickness (µm)	20 – 50	50 – 100
Dimensional accuracy (µm)	100 – 200	400 – 500
Surface quality, Ra (µm)	5 - 10	25 – 35
Geometry complexity	High	Intermediate
Melting rates (cm <sup>3</sup> /h)	7 – 70	55 – 80

In both processes, several scanning strategies can be implemented to scan each layer of the sliced geometry in order to homogenize the temperature distribution along the part surface and through previous layers, minimizing residual stresses. The most common scanning patterns used include unidirectional, bidirectional, spiral, zigzag and cross-wise and, in addition, these patterns can be applied in islands or stripes, as is shown in Figure 2.22 [19].

These scanning patterns influence porosity level, microstructure, surface roughness and heat build-up in the finished metal components [79].

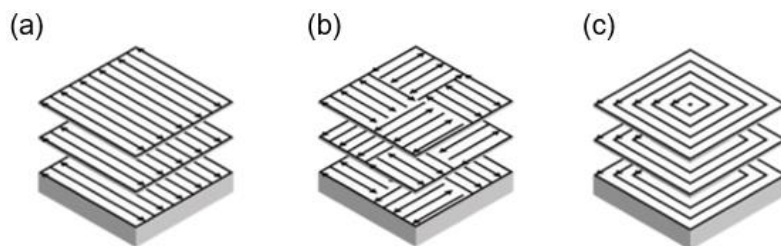


Figure 2.22 – Several scanning strategies used in PBF processes: (a) stripes; (b) islands; (c) contour only [93]

Besides the scanning strategies, several scanning configurations are possible on each layer and, usually, subsequent layers include a rotation of the direction of the scan vector hatch, for instance, a rotation of 67° – Figure 2.23 (e) – is commonly used as it allows a good heat distribution through the layers [94], among other of these strategies.

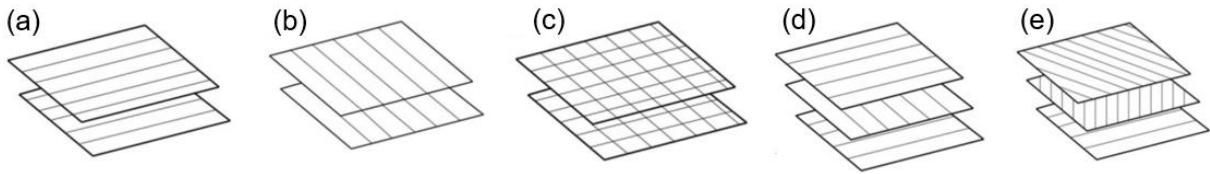


Figure 2.23 – Different scanning strategies across several layers [95]

Although both PBF processes allow a relatively good control on pore size, pore geometry and porosity of metallic scaffolds when compared to the other AM techniques, currently, the forming accuracy of L-PBF is higher than that of EB-PBF, mainly due to the laser spot size being smaller than the electron beam, the powder size in L-PBF being smaller as well as the layer thickness, which helps in decreasing the dimensional deviation between the designed and the as-built geometry [64].

For this reason and as concluded by Yu Qin et al. [64], L-PBF is the ideal AM process for manufacturing biodegradable metal implants, as it allows better control of complex geometries and detailed features of porous structures, which is very needed to obtain components according to the customized design based on clinical requirements.

#### 2.4.5. Manufacturability of metallic lattice structures using L-PBF

L-PBF technique offers exceptional flexibility regarding part design and possible geometries but, although it allows customized products of virtually any geometry to be manufactured, there are some limitations. In order to explore this technology to its full potential there are some design rules that must be taken into consideration.

##### 2.4.5.1. Basic design rules

These design guidelines are valid for L-PBF processes are specified below [79].

###### 1) Holes and internal channels

Currently, the recommended minimum standard hole size is 0.4 mm. Holes and channels that have a diameter below 10 mm usually don't require support structures – Figure 2.24 (on the left) – but above that value support structures become necessary – Figure 2.24 (in the centre), which may be difficult to remove if the channels are nonlinear. A way to avoid these support structures would be to redesign the channel profile, in order to minimize the overhanging areas, as can be seen in Figure 2.24 (on the right) by making use of an ellipse profile instead of a circular one.

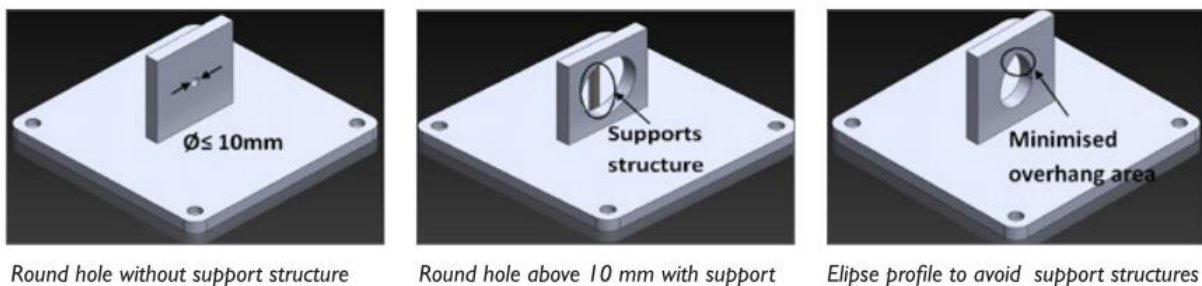


Figure 2.24 – Holes and internal channels basic rules to follow [79]

Another approach could be to functionally integrate the supports in the design, so that there would be no need to removing them.

### 2) Minimum wall thickness

The minimum wall thickness can vary depending on the machine, powder used and material, but usually 0.2 mm is the recommended. If wall sections are too thin or not supported, there is a possibility of buckling happening in the surface of the wall, as can be seen in Figure 2.25.



Figure 2.25 – Ni718 manifold showing buckling effect [79]

### 3) Maximum length-to-height ratio

The length-to-height ratio should not exceed 8:1, otherwise there is a chance to again have buckling effect on the surface of the part, as seen in Figure 2.26a). If the part has a reasonable section or supporting geometry, it's possible to build as a higher width-to-ratio, as shown in Figure 2.26b).

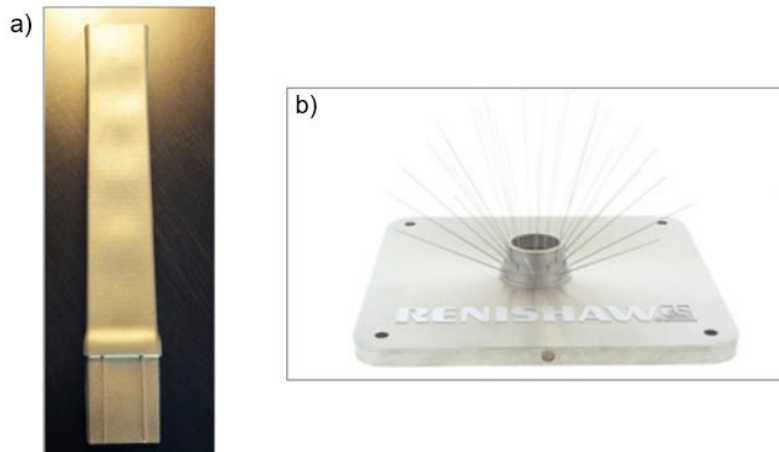


Figure 2.26 – Bike frame component showing buckling in a) and very high length-to-height ratio part in b) [79]

### 4) Minimum strut diameter and lattice structures

Manufacturability of complex lattice structures is highly dependent on the design characteristics of the scaffolds intended to fabricate, such as strut dimensions and unit cell shape. The minimum strut diameter recommended is usually 0.15 mm [79] and, although sacrificial support structures may be added to support overhanging structures (in order to prevent deformations), they can be very difficult or even impossible to remove from the interior of complex cellular lattice structures without destroying the

component [89], as shown in Figure 2.27. This adds considerable constraints on manufacturing versatility, defeating the purpose of using a cellular design by sacrificing the design freedom and geometrical capabilities of AM manufacturing [95]. For these reasons, self-supporting lattice structures are particularly of interest [96].

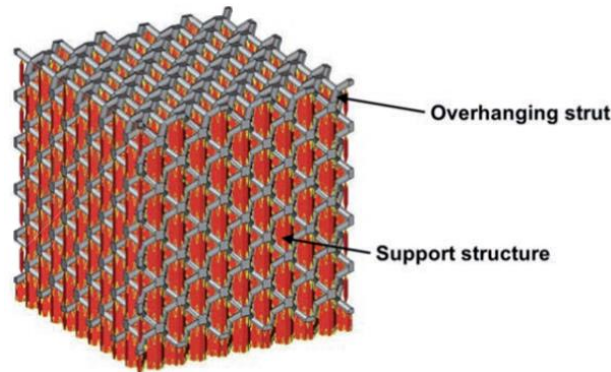


Figure 2.27 – Schematic illustration of overhanging struts and support structures for metallic scaffolds [89]

#### 2.4.5.2. Part orientation

Finding the best suitable orientation of a part in the powder bed, shown in Figure 2.28, is a very important point of attention for both quality and cost. In fact, part orientation influences the build time, quantity of supports, surface roughness and residual stresses and will help achieve [79]:

- The shortest build time, by minimising the number of layers and part height.
- The minimal amount of supports, resulting in less material consumed.
- Easy access to the supports that need to be removed, so that it can be done without difficulty.
- The best possible surface quality, minimizing the staircase effect.
- The least amount of residual stresses in order to avoid part distortion.

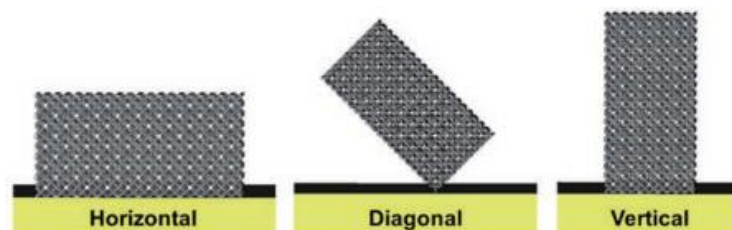


Figure 2.28 – Build orientation of lattice structures in L-PBF [89]

In this way, several rules must be considered.

##### 1) Overhangs

An overhanging structure is a portion of a component that is not supported during building, either by solidified material or a substrate on the bottom side and as so, the melt pool created by the laser beam is only supported by loose powder. From this definition, it becomes clear that what makes a part of a component an overhang is highly dependent on the orientation chosen to this during the manufacturing process [95]. An important rule is to avoid having a too low overhang angle (Figure 2.29) between the build platform and part. When this angle is below  $45^\circ$ , support structures are required to

avoid poor surface roughness as well as distortion and warping, which can even lead to build failure because the warped and curled area may prevent the spreading of a new layer of powder [79].

The poor surface quality results from building directly onto loose powder, instead of using a support structure as a building scaffold. The stresses derived from the quick cooling of the melted area cause the material to curl upwards. If supports were used, they would not only act as an anchor to tie parts down to the build plate but also as way of dissipating the excessive heat, preventing this upward curl by reducing the stress generated in the overhanging area. It should also be noted that the very poor surface consists of melted and partially melted powder, consequence of the sinterization of loose powder particles surrounding the focal point together.

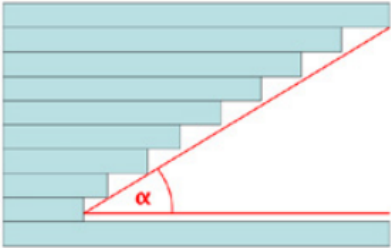


Figure 2.29 – Overhang angle between build platform and part [79]

A strategy used to avoid the use of supports in case of 90° overhangs is to create a 45° chamfer below the overhang area, as shown in Figure 2.30, below.

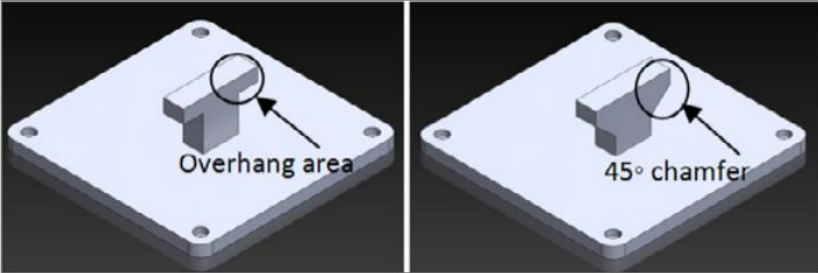


Figure 2.30 – Solution to avoid supports in case of 90° overhangs [79]

2) Support structures

Support structures serve several different purposes, such as supporting the part in case of overhangs, strengthening the fixation of the part to the building platform, dissipating excess heat away (stress relieving) and preventing warping or complete build failure.

Both the position and orientation of the part on the build platform have major influence in the overall need and nature of the supporting structures, thus determining in large scale the final quality of the build and subsequent post-processing operations. In Figure 2.31 is shown an example on how different part positions and orientations influence the location and importance of support structures.



Figure 2.31 – Impact of different part positions and orientations on support structures [79]

In some cases, the removal of the support structures may be impossible, although its orientation may also be the best in terms of processing, so a compromise must be reached.

Apart from the functions already mentioned, supports shall also be optimized in a way that they have minimal weight and can be easy to remove mechanically after building operation. There are many support designs possible and to choose from and in the impeller example, shown in Figure 2.32, two support designs were evaluated by Fraunhofer IFAM: a tree support design with many struts (top left) and wall supports with one wall for each blade (top right). In this case, the latter one revealed to be superior by both allowing better post processing and also improving stability during fabrication.

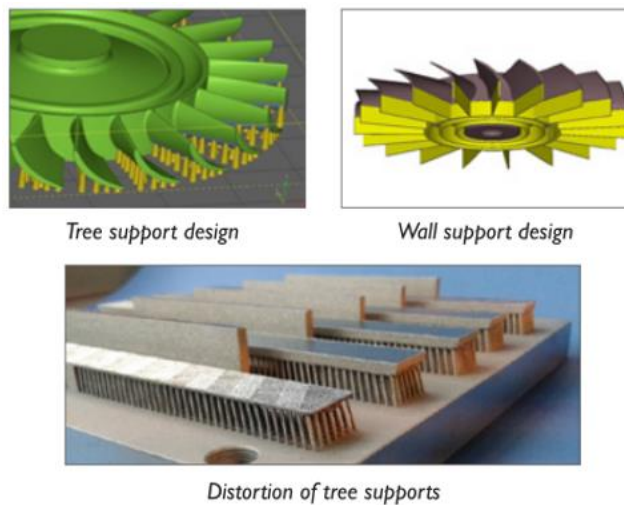


Figure 2.32 – Tree support and wall support designs for an impeller [79]

### 3) Surface roughness



In as built state, surface roughness ( $R_z$ ) is averaging between 25 and 40  $\mu\text{m}$  in parts made by L-PBF, but lower values can be obtained if post-processing techniques such as shot peening and polishing are used. For example, if the surface of the part is polished, it is possible to achieve values of surface roughness as low as 0.1  $\mu\text{m}$ , as can be seen in Table 2.11. It should also be noted that the polishing process efficiency is highly affected by part design complexity.



Table 2.11 – Standard roughness of parts made by L-PBF against conventional machining, adapted from [79]

Achievable roughness average Rz in $\mu\text{m}$																					
	0.04	0.06	0.10	0.16	0.25	0.40	0.63	1.0	1.6	2.5	4.0	6.3	10	16	25	40	63	100	160	250	
Turning																					
Milling																					
Polishing																					
PBF – as built																					
PBF – after shot - peening																					
PBF – after polishing																					

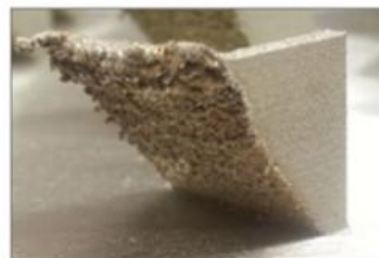
  

	Average Range
	Less Frequent Range

Typical surface defects that highly influence the surface quality of the final part and should be avoided at all costs are: the staircase effect (Figure 2.33, on the left), which can easily be observed on curved surfaces where the surface angle increases a lot along each layer and is very much due the layer by layer fabrication [89]; and poor down-skin surface roughness (Figure 2.33, on the right), which is directly linked to the fact that the heat generated to melt the powder particles is not dissipated fast enough on down-facing surfaces and loose powder particles end up sticking to the surface of the parts, especially on overhangs where supports are not used.



*Staircase effect*



*Poor down-skin surface roughness*

Figure 2.33 – Typical surface defects on L-PBF fabricated parts [79]

#### 4) Thermal stress and warping

As mentioned before, warping is caused by thermal stresses derived from the rapid cooling of the melted area by the laser beam, which induce big thermal gradients. The warped area can then lead to part distortion (Figure 2.34, on the left), which can result in bad junctions between supports and even separation of the part from the supports (Figure 2.34, on the right) and, ultimately, may cause the complete failure of the build by preventing a new layer of powder to be deposited.

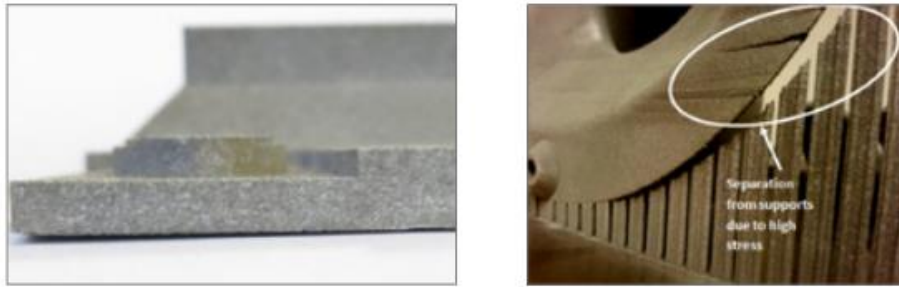


Figure 2.34 – Part distortion (left) and separation of the part from supports (right) [79]

An example where a metal lattice structure was manufactured with the desired geometry and internal features in a single fabrication step using L-PBF, and part orientation revealed to be crucial is shown in Figure 2.35. This particular cubic lattice structure was possible to obtain without the need of any support structures by orienting the component with an angle of  $45^\circ$  with respect to the building platform [95].

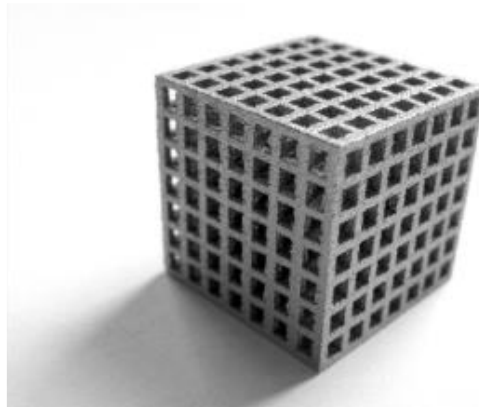


Figure 2.35 - Aluminium lattice structure [95]

### 2.4.5.3. PBF process parameters

Material properties of components obtained with AM processes are very particular and are usually superior to the properties obtained with investment casting processes and inferior or sometimes close to conventional wrought parts [79].

Parts produced using AM processes usually show key characteristics such as: a fine micro-structure, due to the very rapid solidification process; a slight anisotropy in Z direction that cannot be avoided like in X and Y by adjusting laser scanning strategies, because it's due to the superposition of the layers, resulting in slightly lower mechanical properties; and a few small residual porosities, specially below the surface. Like in parts made by investment casting, post processing by hot isostatic pressing (HIP) can be used to achieve full density [79].

Residual stresses and poor surface roughness are typical defects found in components obtained by AM that have already been mentioned before, but there are other defects that should be named, such as unmolten powder particles, lack of fusion, pores, cracks and inclusions - Figure 2.36. These usually happen if incorrect part orientation, build strategy or process parameters are chosen.



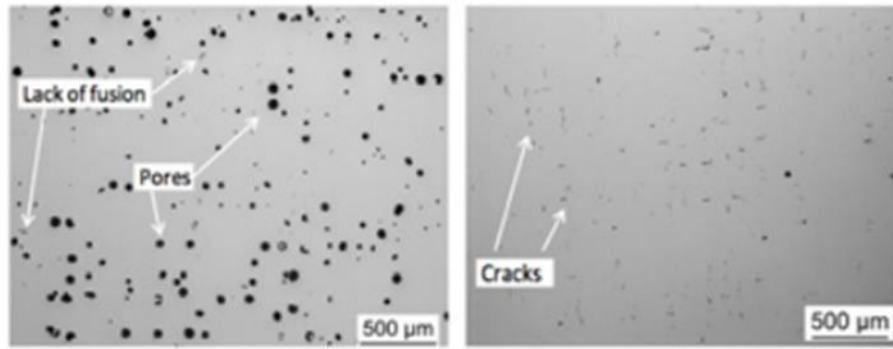


Figure 2.36 – Defects found in parts produced by L-PBF technology [79]

Choosing the right process parameters is of extreme importance in order to be able to obtain parts with high mechanical strength and the appropriate fatigue behaviour. Therefore, it is important to find a set of laser parameters that guarantees the fabrication of high-density parts with very good surface quality, minimising defects as much as possible.

In laser processes such as L-PBF, energy density is a key factor that is described as the average energy per volume of material and can be expressed by equation (2.6) [97]:

$$E = \frac{P}{v \cdot h \cdot t} \quad (2.6)$$

where  $P$  represents laser power,  $v$  is scan speed,  $h$  is hatch spacing and  $t$  is layer thickness. In the one hand, it is necessary that the energy density applied is enough to melt the powder particles of the layer being processed and the previous one, to assure proper joining across successive layers and avoid lack of fusion and porosity. In the other hand, excessive energy can cause vaporisation of the material creating defects called keyholes, reducing material density [79,98]. All these process parameters are represented in Figure 2.37 and a summary of the effects each one of them has is in Table 2.12.

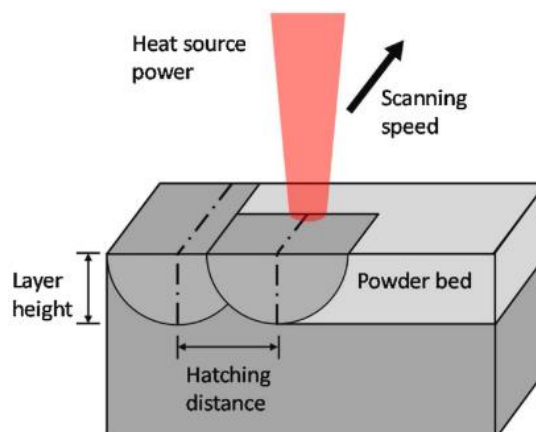


Figure 2.37 – Process parameters in L-PBF [19]

Table 2.12 – Effect of process parameters [99]

Parameter	Effect on increasing parameter
Laser power	Width and height increase Dilution increases Better bonding with previous layers
Scan speed	Reduced track width, track height and bonding with previous layer Refined grains and enhanced strength
Powder feed rate	Increase in track height Enhanced deposition rate
Laser spot size	Increases minimum feature size
Hatch distance or spacing	Increased porosity
Layer thickness	Roughness increases and stair-stepping effect

Furthermore, manufacturability of cellular lattice structures is also very dependent on these process parameters and the interaction among them [89]. For instance, if the laser power applied during the fabrication of lattices is too high, it can not only lead to the formation of thicker struts than the designed due to melt pools differing from the desired cross section, but also increase powder adhesion on the struts [100].

#### 2.4.6. Post processing of L-PBF components – hot isostatic pressing (HIP)

Post processing operations of AM parts can include machining, shot peening, grinding, polishing, surface and heat treatments, among others. When dealing with metal lattice structures, two categories of density (or porosity) can be mentioned: one referring to designed pores, which are purposely fabricated according to the desired geometric structure; and the other refers to processing pores, which are unexpected and random separated cavities caused by inappropriate processing conditions and jeopardize the performance of the lattice structures [64].

Hot isostatic pressing (HIP), shown in Figure 2.38, is a post processing technique that is very commonly used on parts made by L-PBF for densification, to prevent and eliminate residual porosities, the so-called processing porosities that in porous scaffolds are located inside struts [101]. This process consists in exposing as-built parts to temperatures up to 2000°C and high gas pressures up to 200MPa, conditions that can eliminate defects and internal porosity and, ideally, 100% densification is achievable. Depending on the material, HIP parameters, such as specific temperature, pressure and hold times can be customized and post HIP heat treatment is usually required for the majority of components in order to reach full material properties [79].

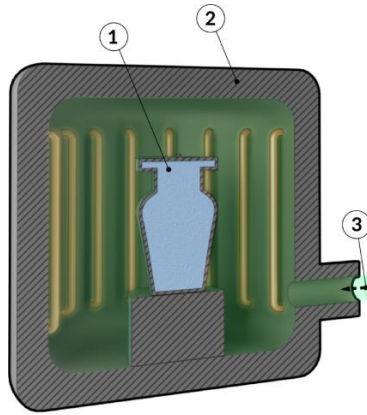


Figure 2.38 – Hot Isostatic Pressure: (1) as-built part by L-PBF; (2) pressure chamber; (3) herated gas [102]

In addition to the already mentioned benefits, due to the elimination of the microporosity this process can significantly improve fatigue life, impact toughness, creep strength and ductility, while also decreasing anisotropy along the building direction (Z axis) [79,101].

## 2.5. L-PBF applied to medical industry

According to the current development and as said before, AM technologies are now suitable to produce very complex nearly finished parts, not only prototypes, as initially. Looking directly at the medical sector, it is now possible to conceive some sort of personalized medicine, like customization, design and production of patient-particular parts, since virtually any geometry can be manufactured. For instance, with AM it is possible to obtain customized implants according to patient's specifications fairly quickly [103]. Some other relevant improvements this technology could bring to the medical sector are [66]:

- Production of lightweight implants.
- Improvement in the strength of implants.
- Surface quality excellence.
- Reduction of manufacturing times.
- Cost savings.

The process of manufacturing custom made implants starts with acquiring patient's anatomical data, which is obtained with resort to scanning processes and medical imaging techniques, such as magnetic resonance imaging (MRI) and radiography (X-ray). This raw scanning data is then reconstructed through medical image processing to obtain a 3D model, to which can be added later specific AM designed features [103]. This process flow is shown in Figure 2.39 and after this, the final CAD of the model is finished and ready to be printed.

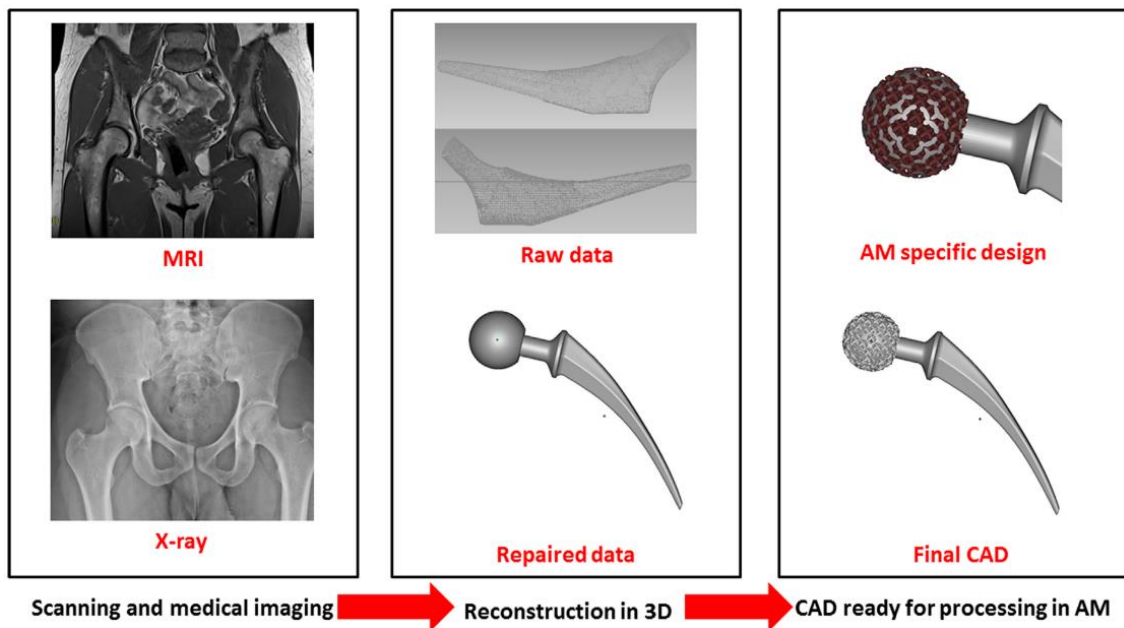


Figure 2.39 – Process flow from patient’s anatomical data acquisition to the final CAD model of the implant [103]

Jardini et al. [104], fabricated a customized TiAl4V cranial implant for a surgical reconstruction of a very large cranial defect, showed in Figure 2.40 (b). The anatomy of the defect was obtained using a series of computer tomography (CT) data and, with the help of a CAD software, a model of the implant was designed - Figure 2.40 (a). After this, the prosthetic implant was manufactured using L-PBF. The duration of the surgical procedure to place the implant into the patient lasted around 3 hours, while if non-customized implants had been used, it should have taken approximately 6 hours to finish a similar surgery, due to manually having to formulate the reconstruction plate during the operation. The use of customized implants resulted in a significant reduction in the duration of the surgery, since it allowed preoperative planning of correct geometrical and anatomical details [104].

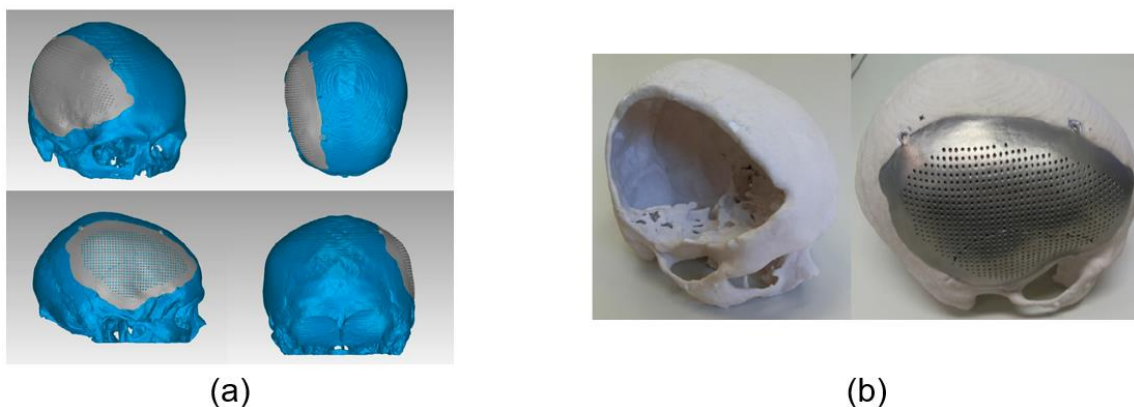


Figure 2.40 – (a) CAD model of the surgical implant, based on CT-scan data; (b) biomedical and customized implant for craniofacial reconstruction surgery fabricated by L-PBF [104]

Sajad Arabnejad et al. [9], fabricated a fully porous titanium femoral stem for hip replacement (shown in Figure 2.41), following total hip arthroplasty (THA), which is a procedure commonly used to relieve pain, restore function and improve the quality of life for patients with compromised hip joints. In this case, a finite element model was generated by processing, once again, CT-scan data from the

patient femoral bone. This model was used to make a topology optimization and obtain an interior 3D lattice structure of the implant with a tetrahedron based unit cell, by simulating the bone loaded under equivalent physiological loading and boundary conditions. The resultant geometry was then printed using L-PBF and this porous micro-architecture inside the implant allowed to achieve a greater than 75% bone resorption secondary to stress shielding, while respecting bone in-growth requirements at the implant interface, when compared to a fully solid implant [9].

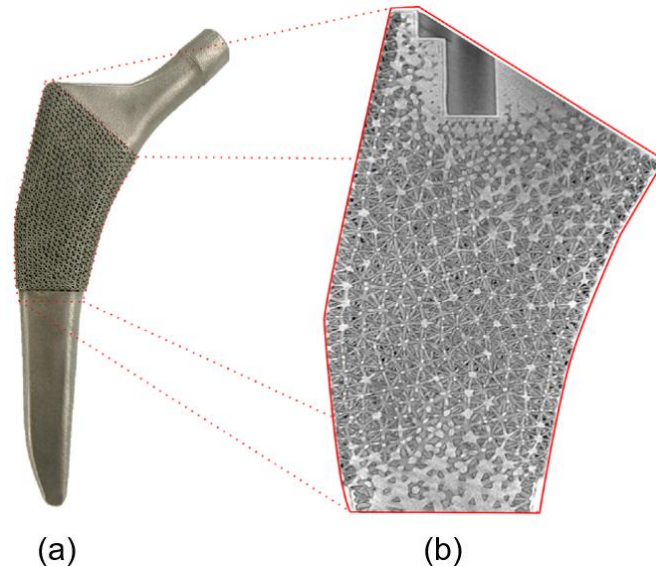


Figure 2.41 – (a) Hip implant manufactured by L-PBF; (b) micro CT-scan assessment of the implant lattice structure [9]

Simon Merkt [105] fabricated patient-tailored finger implants for patients suffering from rheumatoid arthritis (RA) or degenerative diseases like osteoarthritis (OA). Figure 2.42 (a) and (b) clearly show the bone erosions on the metacarpophalangeal of a patient suffering from long-term RA, when compared to a healthy control.

Similar to the previous cases, to better characterize and visualize these bone changes, high-resolution CT was used and the data obtained was reconstructed into 3D models, using CAD software. After that, they were 3D printed using L-PBF. One of the main reasons why standard implants tend to have a poor long-term outcome is the lack of individuality, which can be solved using the mentioned process. L-PBF also allows the manufacturing of implants with improved functionality, such as the introduction of an internal lattice structure while keeping the joint's surface unchanged, as can be seen on Figure 2.42 (c), adapting the stiffness of the implant to meet the stiffness of the bone. As a result, stress shielding is lowered and fatigue limits are improved, which ultimately improves the quality of life of patients suffering from these RA and OA diseases [105].

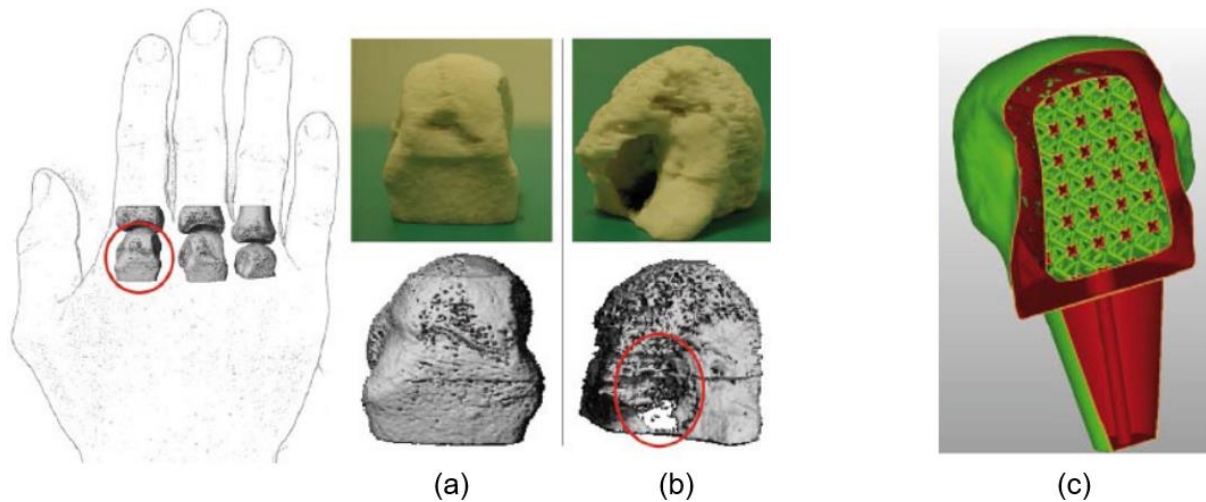


Figure 2.42 – Reconstructions and 3D model of the metacarpophalangeal head of a (a) healthy control and (b) a RA patient, where the red circle marks the characteristic erosion in a RA patient; (c) sectional view of CAD model of the implant, where lattice internal structure is visible [105]

The case studies above showed the need of efficient and validated data acquisition in order to reconstruct the orthopaedic implants with accurate fit via L-PBF. As can be seen, L-PBF has already been successfully used in the fabrication of permanent metal implants with lattice structures. However, in terms of biodegradable metal implants there is still a lot to be explored.

The current study of biodegradable Fe in the medical industry has been focused on the application to vascular stents, but the development of AM technology may promote its further use in orthopaedic applications in the shape of porous scaffolds or lattice structures [39] because, as it has been mentioned in sections 2.1.4 and 2.3.3, the increased surface area this type of geometries provide can improve and accelerate the low degradation rate that iron presents.

Li et al. [60], demonstrated for the first time how L-PBF could be used in the manufacturing of iron lattice structures, by being able to obtain a precisely controlled topology with fully interconnected pores, shown in Figure 2.43.



Figure 2.43 – Iron lattice structure [60]

*In vitro* degradation tests were conducted over a period of 28 days, where it was verified that the elastic modulus and yield strength of the specimen decreased by 7% and 5%, respectively and its weight reduced by 3.1%. Even after the degradation tests, the mechanical properties of the lattice



structures still remained within the values reported for trabecular bone. It was found that there were different mechanisms of biodegradation behaviour on the periphery and in the centre of the cylindrical specimens, which suggests that the topological design is a very important factor in adjusting the biodegradation behaviour of AM porous iron.

Later, in a new study, Li et al. [39] explored the permeability, dynamic biodegradation behaviour mechanical properties and cytocompatibility of functionally graded porous iron lattice structures, also manufactured by L-PBF, shown in Figure 2.44.

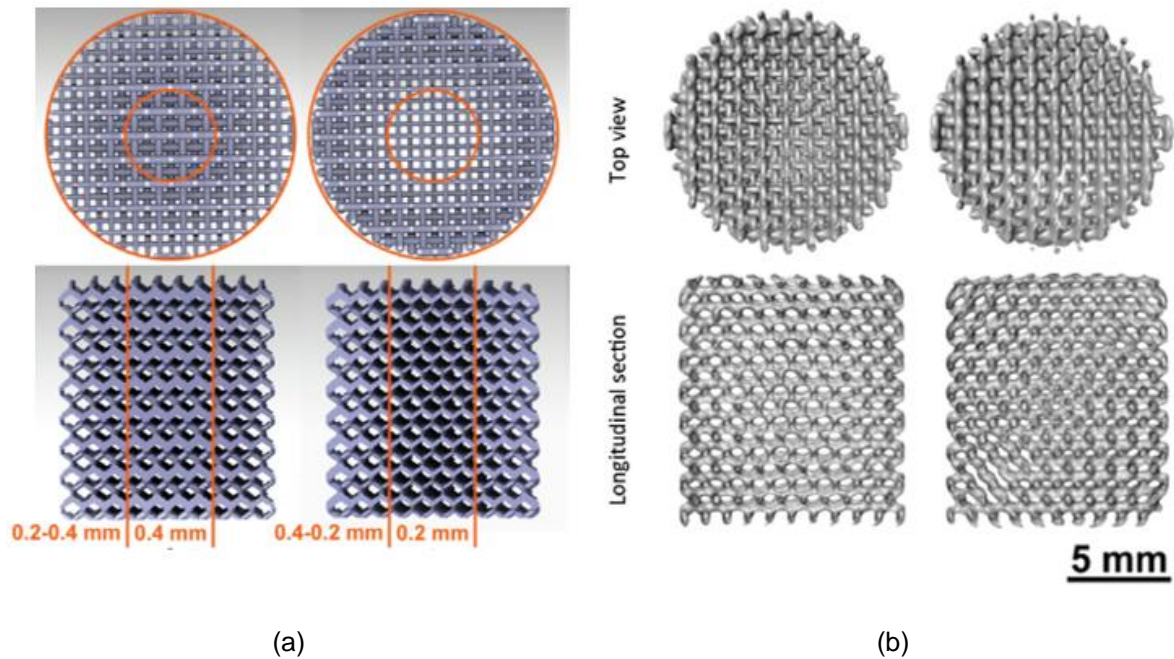


Figure 2.44 – Graded topological designs: (a) top view and longitudinal cross sections of CAD models of dense-in (left) and dense-out (right); (b) top view and longitudinal cross sections of micro-CT reconstructions of the AM porous iron specimens, adapted from Li et al. [39]

It was found that after 4 weeks of *in vitro* biodegradation, the mechanical properties of the specimens remained within the range of values reported for trabecular bone. Besides, these iron specimens lost 5 to 16% of their weight, which falls into the desired range of biodegradation rates for bone substitution materials, confirming the hypothesis of the first study that topological design could accelerate the biodegradation of slowly degradation metals, like iron.

These findings show that with appropriate topological design, iron-based lattice structures hold a great potential to become a new generation of functional and degradable biomaterials for orthopaedic applications, while becoming a highly attractive candidate for the development of future temporary bone implants.





### 3. Methodology

According to the literature review (section 2.3), iron (Fe) is one of the most promising biodegradable metals to be used in bone implants and thus, Fe will be the material to be further explored in this dissertation.

The present work aims to find the unit cell topologies of lattice structures with the closest mechanical properties to those of bone for a given relative density, based on the polyhedrons chosen by Chantarapanich et al. [35] as the most suitable for tissue engineering, among 119 polyhedrons. For this, finite element analyses (FEA) were performed, followed by experimental compression tests to assess the numerical model of the lattice structures.

In this chapter, the design of the lattice structures, as well as the numerical and the experimental procedures will be described.

#### 3.1. Unit cell design

Six types of cellular structures were designed from different unit cells, which were selected based on the previous work of Chantarapanich et al. [35]. This work presented an evaluation of a library of 119 polyhedrons (for open- and close-cellular scaffolds) for tissue engineering based on three criteria: (1) manufacturability by AM, in which polyhedrons containing excessive geometric details were eliminated; (2) geometric and mechanical strength considerations, where polyhedrons that accumulated high stresses in the junctions between unit cells were eliminated; (3) geometric considerations, in regards to whether the geometry resulting from the polyhedrons assembly had enclosed pores or not, shown in Figure 3.1 (a) and (b), which can make the removal of material after the fabrication using AM not possible.

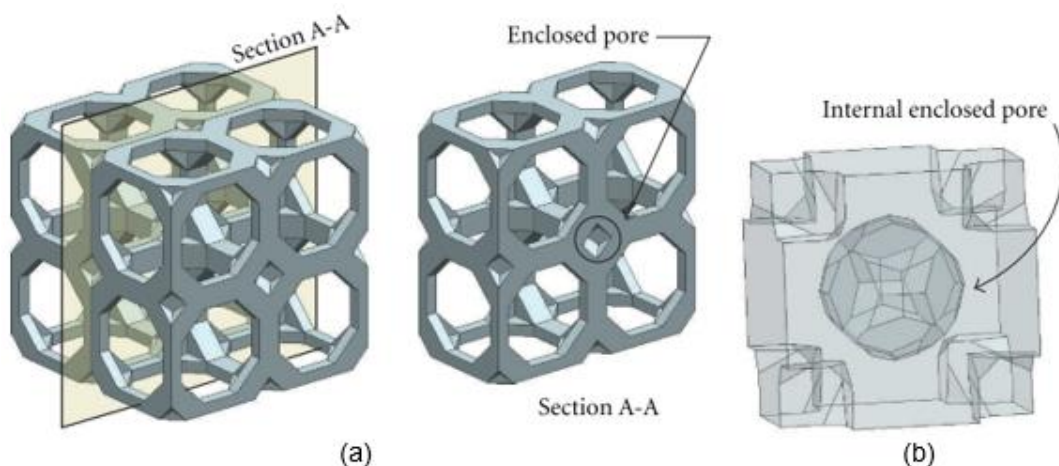


Figure 3.1 – (a) enclosed pore by surrounding cells, (b) enclosed pore inside the cell [35]

As discussed in section 2.2, open cell lattice structures bring several advantages and are especially desirable in iron bone implant applications because the increased surface area could result in an increase in the degradation rate and to better mimic the bone strength. So, the six unit cell topologies selected are the most suitable open cell polyhedrons according to Chantarapanich et al. [35]

analysis: cubic (C), cuboctahedron (CO), truncated cube (TC), truncated octahedron (TO), rhombicuboctahedron (RCO) and rhombi-truncated cuboctahedron (RTCO), presented in Figure 3.2.

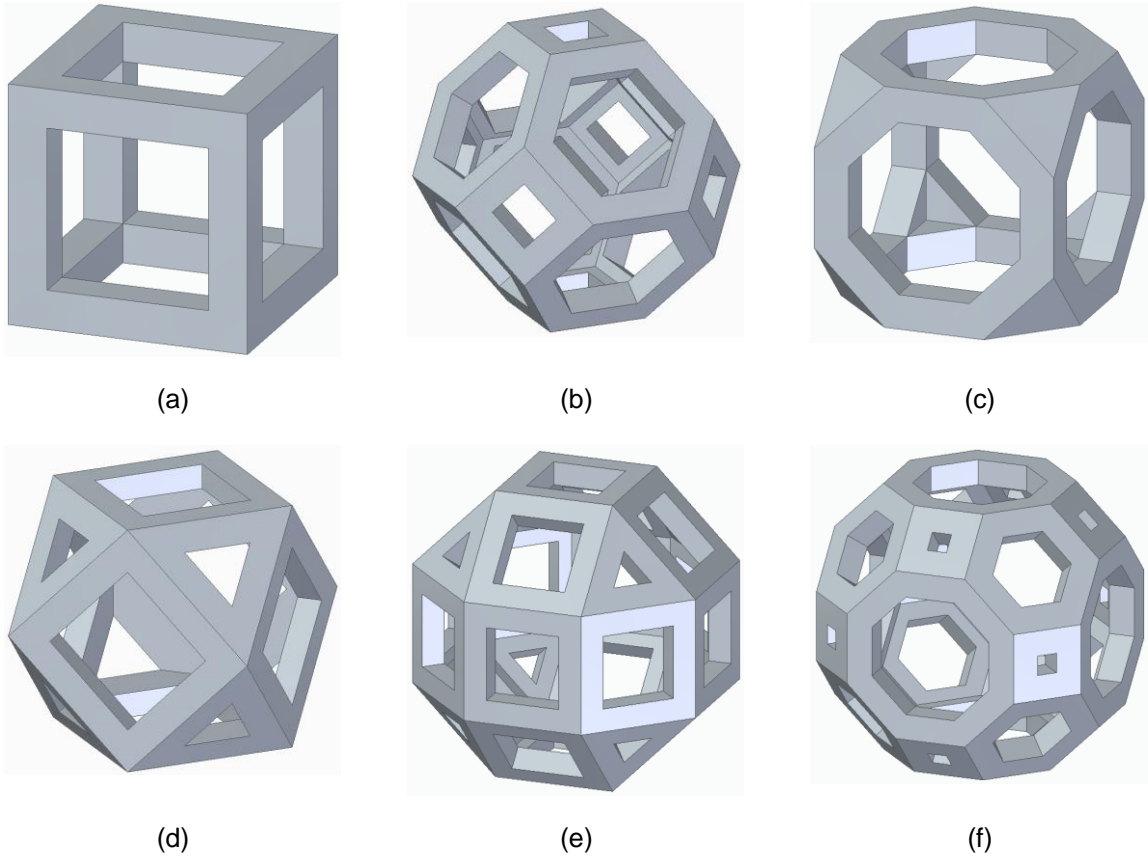


Figure 3.2 – Unit cells selected to be analysed: (a) cubic; (b) truncated octahedron; (c) truncated cube; (d) cuboctahedron; (e) rhombicuboctahedron; (f) rhombitruncated cuboctahedron

Each unit cell was designed to have a size of  $3.5 \times 3.5 \times 3.5 \text{ mm}^3$ , similar to Sharma et al. [12], so that the total size of the lattice structure would always be the same after replicating the unit cell as many times as wanted in each of the three directions, regardless of the topology.

The design of the unit cells presented in Figure 3.2 was successfully performed using the CAD software Solid Edge 2020. However, for the design of the cuboctahedron (CO) topology, an error of “zero wall thickness” occurred that did not allow to replicate the CO unit cell in every direction, in order to get the lattice structure. It was tried to design the structure using different methodologies and software, with no success. For this reason, the CO topology will be further left out of the analysis, as it was not possible to correctly obtain a lattice structure out of its unit cell.

In short, the topologies considered in the following work were the cubic (C), truncated cube (TC), truncated octahedron (TO), rhombicuboctahedron (RCO) and rhombitruncated cuboctahedron (RTCO).

### 3.2. Numerical Modelling

The numerical simulations of the compression tests were performed using the software Siemens NX, version 1904. The program solver *Simcenter Nastran* uses the finite element method (FEM) to do the necessary calculations and the type of solution selected was the *SOL 106 Nonlinear Statics – Global*

*Constraints*, which uses an implicit formulation that is applicable to static, quasi-static and nonlinear buckling analysis. This solution was chosen because material nonlinearity effects become quite considerable when structures are subjected to displacements as large as the pretended [106].

The program's finite element formulation for equilibrium equations is based on a variational principle that when applied to a functional  $\Pi$ , represents a total potential of a continuum by [106]:

$$\Pi = U - W \quad (3.1)$$

where  $U$  is the strain energy of the system and  $W$  is the potential energy of the external loads.

When considering a three-dimensional continuum for a nonlinear problem, as is the case for the pretended simulations, the stationarity condition results in [106]:

$$\int_V \sigma_{ij} \delta \varepsilon_{ij} dV = \int_V b_i \delta u_i dV + \int_V t_i \delta u_i dS + \sum_i p_i \delta u_i \quad (3.2)$$

where the dots and  $\delta$  represent infinitesimal increments and arbitrary variations, respectively. The left-hand side portrays variations in the strain energy, while the right-hand side expresses the variations in the external work which may be due to body forces  $b_i$  (such as gravity load), traction forces  $t_i$  at the boundary surface (such as pressure loads), and concentrated forces  $p_i$ .

The yield criteria chosen was the von Mises yield criterion, which states that yielding begins when the elastic distortion energy exceeds a critical value and is given by [107]:

$$(\sigma_x - \sigma_y)^2 + (\sigma_y - \sigma_z)^2 + (\sigma_z - \sigma_x)^2 + 6(\tau_{xy}^2 + \tau_{yz}^2 + \tau_{xz}^2) = 2\sigma_Y^2 \quad (3.3)$$

where  $\sigma_Y$  refers to the yield strength of the material.

The boundary conditions considered for each simulation were a *simply supported constraint* at the base of the structure ( $Z=0$ ), where the Z axis translation is fixed while all other 5 degrees of freedom are free, and an *enforced displacement constraint* on the top face of the lattice, which applies a set displacement value in the Z direction.

For the simulation of each lattice structure, a mesh refinement was performed so that reliable and accurate results were obtained. The convergence analysis considered the convergence of the effective stress,  $\bar{\sigma}$  (von Mises stress), given by equation (3.4) [107], for a given node of the mesh along the several refinements and the convergence of the reaction force response in the base of each lattice to the enforced displacement on the top face. The values obtained for the effective strain,  $\bar{\varepsilon}$  (von Mises strain), given by equation (3.5 [107], will also be further analysed for the different topologies.

$$\bar{\sigma} = \frac{\sqrt{2}}{2} \sqrt{(\sigma_x - \sigma_y)^2 + (\sigma_y - \sigma_z)^2 + (\sigma_z - \sigma_x)^2 + 6(\tau_{xy}^2 + \tau_{yz}^2 + \tau_{xz}^2)} \quad (3.4)$$

$$\bar{\varepsilon} = \frac{3}{\sqrt{2}} \sqrt{(\varepsilon_x - \varepsilon_y)^2 + (\varepsilon_y - \varepsilon_z)^2 + (\varepsilon_z - \varepsilon_x)^2 + \frac{3}{2}(\gamma_{xy}^2 + \gamma_{yz}^2 + \gamma_{xz}^2)} \quad (3.5)$$

The material considered for the numerical simulations was pure iron (Fe), which is commercially available with 99.8% purity, from *Goodfellow Inc.*, Cambridge, UK. The mechanical properties of this material were previously assessed by Neves [74], who performed uniaxial tensile tests according to ASTM E8/E8M – 21 [108], *Standard Test Methods for Tension Testing of Metallic Materials*, and uniaxial compression tests following ASTM E9-19 [109], *Standard Test Methods of Compression Testing of Metallic Materials*, with the intent of obtaining the mechanical characterization of this material. The Ludwik-Hollomon curve obtained and used in the numerical simulations is:

$$\bar{\sigma} = 984\bar{\varepsilon}^{0.229} \text{ MPa} \quad (3.6)$$

To illustrate the convergence analysis, the topology C-0.57 (lattice structure that has cubic unit cells with a strut of 0.57 mm) was considered. This lattice structure consisted of 2 x 2 x 2 unit cells with a relative density of 25%. For these simulations, an enforced displacement of 1 mm, divided in 20 iterations of 0.05 mm each was imposed, corresponding to a total engineering strain of 14.29%.

The node in the successive generated meshes for this topology that was selected to obtain the effective stress value is shown in Figure 3.3.

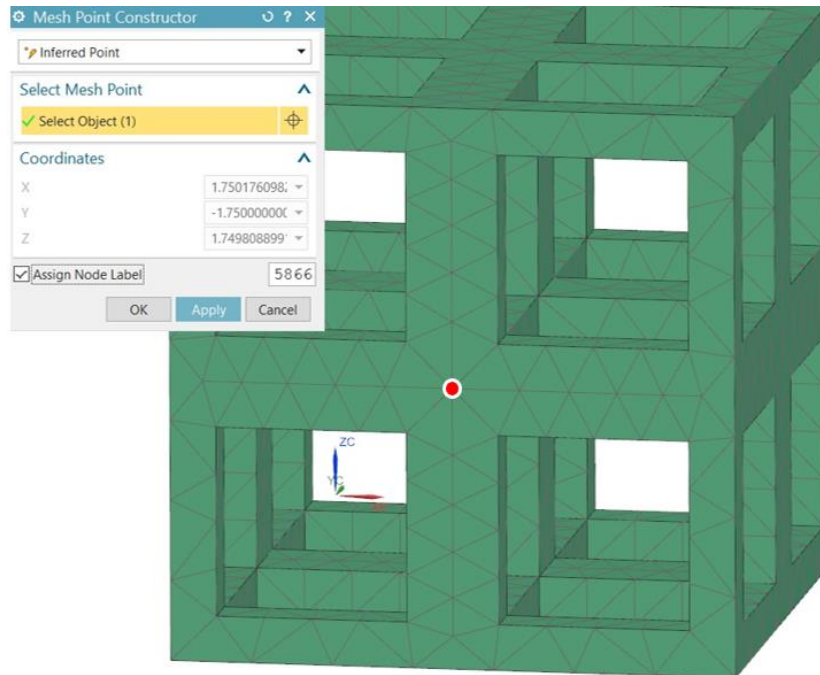


Figure 3.3 – Node 5866 selected to perform the convergence analysis on the effective stress

In Table 3.1 are presented the successive values obtained for the effective stress through the several refinements, along with the relative error in percentage calculated using the equation:

$$\Delta\bar{\sigma} = \left| \frac{\bar{\sigma}_{i+1} - \bar{\sigma}_i}{\bar{\sigma}_i} \right| \times 100\% \quad (3.7)$$

where  $\bar{\sigma}$  refers to the effective stress and the subscript  $i$  refers to the mesh number.

It is due to equation (3.7) that the last row of the relative error is not filled in Table 3.1 and further tables alike, as there is no effective stress value obtained for the node after the last mesh that could allow to proceed to its calculation.

Table 3.1 – Effective stress values obtained for the selected node 5866 through the several refinements of the topology C-0.57 and the associated relative error

Node ID - 5866	Element size [mm]	Effective stress [MPa]	Relative error [%]
Mesh 1	1.00	357.795	2.85
Mesh 2	0.50	347.582	0.19
Mesh 3	0.30	348.255	0.97
Mesh 4	0.25	344.873	0.83
Mesh 5	0.23	347.740	-

As can be seen, the variation of the result obtained from the Mesh 3 to the Mesh 4 is close to 0.97%, which is already very negligible. The values of the effective stress presented above were plotted to obtain Figure 3.4.

In Figure 3.4 is presented the convergence analysis of the effective stress, in regard to the chosen node 5866, along the successive refinements.

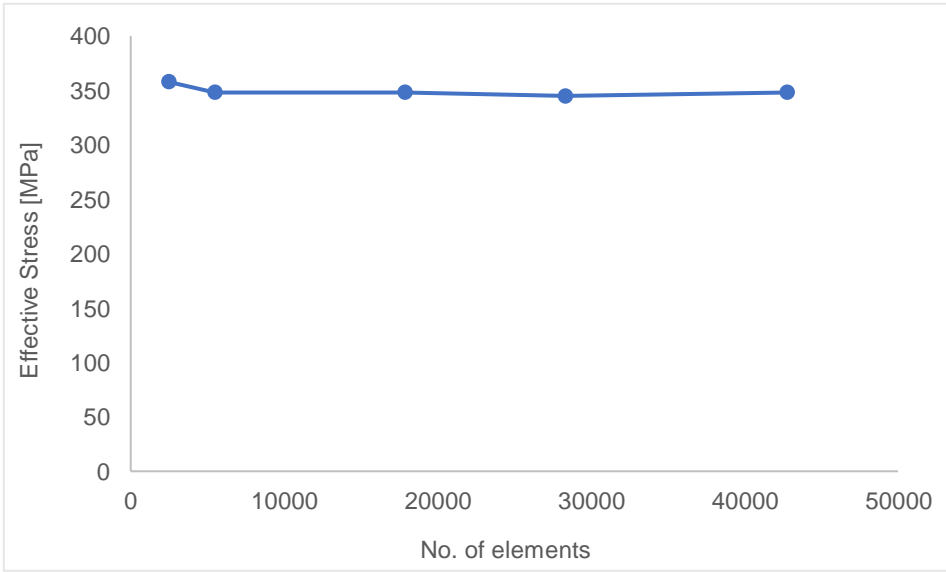


Figure 3.4 – Convergence analysis of the effective stress on node 5866 of C-0.57

In Table 3.2 are presented the successive values obtained for the reaction force in the base of the lattice structure through the several iterations and across refinements, along with the relative error in percentage. An average of the relative error from refinement to refinement was calculated and is presented in the last row of this table. As can be see, the mean variation of the values obtained for each iteration from the Mesh 3 to the Mesh 4 is around 0.21%.

Table 3.2 – Reaction Force values obtained for each iteration on the different meshes and relative error across the several refinements, along with the average relative error

Displacement [mm]	Mesh 1	Relative error [%]	Mesh 2	Relative error [%]	Mesh 3	Relative error [%]	Mesh 4	Relative error [%]	Mesh 5
	Force [N]		Force [N]		Force [N]		Force [N]		Force [N]
0.00	0.0	0.00	0.0	0.00	0.0	0.00	0.0	0.00	0.0
0.05	1818.6	6.71	1940.8	0.82	1956.6	0.42	1948.4	0.00	1948.4
0.10	1920.7	6.47	2045.0	1.19	2069.3	0.25	2064.2	0.22	2068.6
0.15	1968.5	7.02	2106.8	1.49	2138.2	0.17	2134.6	0.20	2138.9
0.20	2006.9	7.56	2158.6	1.87	2198.9	0.25	2193.4	0.16	2197.0
0.25	2047.7	7.78	2206.9	1.99	2250.8	0.26	2245.0	0.21	2249.6
0.30	2093.1	7.90	2258.5	1.85	2300.3	0.24	2294.8	0.25	2300.6
0.35	2136.8	7.96	2306.9	1.93	2351.3	0.29	2344.6	0.27	2350.9
0.40	2179.5	8.00	2353.9	1.91	2398.8	0.25	2392.9	0.27	2399.5
0.45	2219.1	8.17	2400.4	1.90	2446.0	0.29	2439.0	0.30	2446.4
0.50	2256.6	8.30	2443.9	1.88	2489.8	0.27	2483.2	0.28	2490.2
0.55	2296.7	8.25	2486.1	1.83	2531.7	0.21	2526.5	0.25	2532.8
0.60	2334.2	8.35	2529.2	1.77	2573.9	0.17	2569.6	0.25	2575.9
0.65	2373.6	8.38	2572.5	1.67	2615.5	0.15	2611.5	0.27	2618.6
0.70	2414.5	8.37	2616.7	1.54	2656.9	0.17	2652.3	0.29	2660.0
0.75	2453.9	8.38	2659.6	1.48	2698.9	0.21	2693.2	0.30	2701.4
0.80	2491.1	8.41	2700.5	1.48	2740.5	0.20	2734.9	0.30	2743.2
0.85	2526.4	8.48	2740.8	1.49	2781.6	0.20	2776.1	0.28	2783.9
0.90	2563.2	8.51	2781.4	1.46	2822.1	0.19	2816.6	0.26	2823.8
0.95	2600.8	8.52	2822.5	1.41	2862.2	0.18	2857.0	0.23	2863.6
1.00	2637.6	8.59	2864.0	1.33	2902.2	0.18	2896.8	0.23	2903.5
		8.27		1.6		0.21		0.26	

In Figure 3.7, the force-displacement values presented in the Table 3.2 were plotted to show the convergence analysis of the reaction force response in the base of the lattice structure to the enforced displacement on the top face.

After examining Figure 3.4 and Figure 3.7, along with Table 3.1 and Table 3.2, one can see that any further refinement beyond the Mesh 3 does not bring any more certainty or level of accuracy, as the curves are already overlapped. Besides, the associated computation cost of pushing for a more refined mesh would not be worth it, because it can be confidently said that both the values of effective stress and reaction force have converged.

For this reason, the results from the Mesh 3 were chosen as representative of the structural reaction for this topology, as they showed the optimum balance between accuracy of results and computational time cost.

Most of the preliminary analysis, such as the element type selection, relative density and part of the topology analysis, were performed on a laptop equipped with an Intel i7-4710HQ CPU (2.5 GHz)

and 12GB of RAM, while the later topology analyses of the most complex structures and the full models were performed on a desktop PC, equipped with an Intel i7-6950X CPU (3.0 GHz) and 128GB of RAM.

### 3.2.1. Element type selection

To discretize the lattice structures 3D elements, commonly referred to as solid elements, were used due to the complexity of the topologies. The CTETRA elements that were chosen and are shown in Figure 3.5, are four-sided solid (tetrahedral) elements that may have two variations: one with four vertex nodes, shown in blue in Figure 3.5 (a), forming the element CTETRA4 (with only 4 grid points); and another with up to six additional mid-side nodes, shown in green in Figure 3.5 (b), forming the element CTETRA10 with 10 grid points, in total. In the last one mentioned, all 10 nodes should be included as the accuracy of the element will decrease if some but not all the mid-edge grid points are used [110].

*Simcenter Nastran* (solver) calculates the element stresses ( $\sigma_x, \sigma_y, \sigma_z, \tau_{xy}, \tau_{yz}, \tau_{zx}$ ), necessary for the calculation of the effective stress, at the centre of the element and at the Gauss points, which are then extrapolated to obtain the stresses at the corner grid points [110].

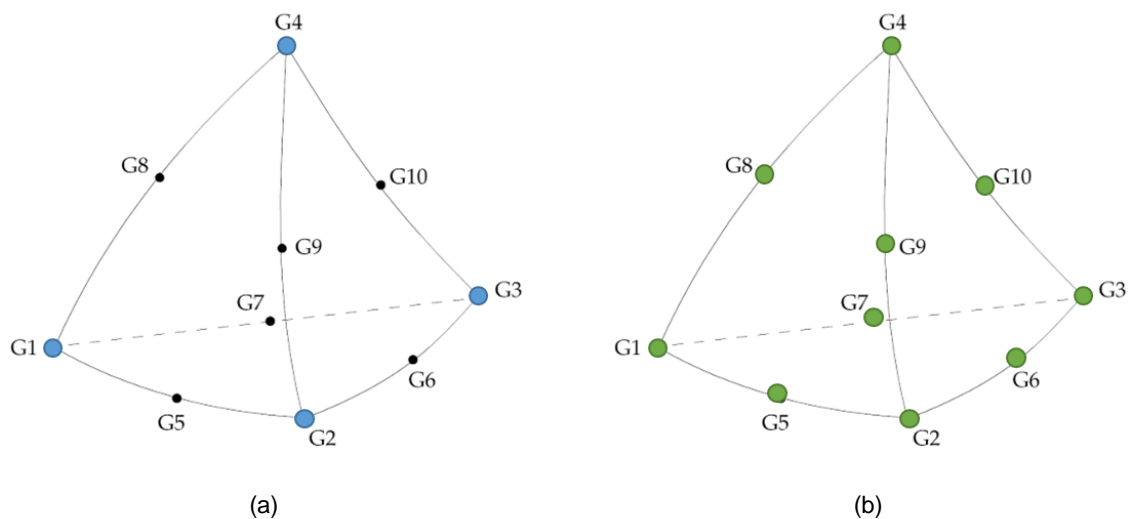


Figure 3.5 – CTETRA elements: (a) CTETRA4 and (b) CTETRA10 [110]

Two different meshes were generated for a C-0.57 (see section 3.2.2 for nomenclature) lattice structure with  $2 \times 2 \times 2$  cells, one using CTETRA4 elements and another using CTETRA10 elements, to compare the results obtained for the convergence analysis of the reaction force along the refinements.

For this analysis, the element size defined for both meshes was the same through all the meshes, resulting in the same number of elements, as can be seen in Table 3.3 and Table 3.4 shows the CTETRA10 mesh characteristics and computational solving times.

Table 3.4. This was due to the fact that their shape is the same – a tetrahedron – with the only difference being that CTETRA10 elements take into consideration six additional mid-side nodes on the edges of the polyhedron.

Table 3.3 shows the CTETRA4 mesh characteristics and computational solving times.

Table 3.3 – Mesh with CTETRA4 characteristics and solving computation time

Mesh	Element size [mm]	No. of elements	No. of nodes	Computation time
Mesh 1	1.00	2455	1115	3s
Mesh 2	0.60	2690	1209	3s
Mesh 3	0.50	5490	2244	7s
Mesh 4	0.30	17789	5750	54s
Mesh 5	0.25	28337	8686	2min25s

Table 3.4 shows the CTETRA10 mesh characteristics and computational solving times.

Table 3.4 – Mesh with CTETRA10 characteristics and solving computation time

Mesh	Element size [mm]	No. of elements	No. of nodes	Computation time
Mesh 1	1.00	2455	5864	9s
Mesh 2	0.60	2690	6358	9s
Mesh 3	0.50	5490	12256	18s
Mesh 4	0.30	17789	34236	1min29s
Mesh 5	0.25	28337	52291	4min49s

The convergence of the reaction force-displacement curves of the mesh with CTETRA4 elements can be seen in Figure 3.6.

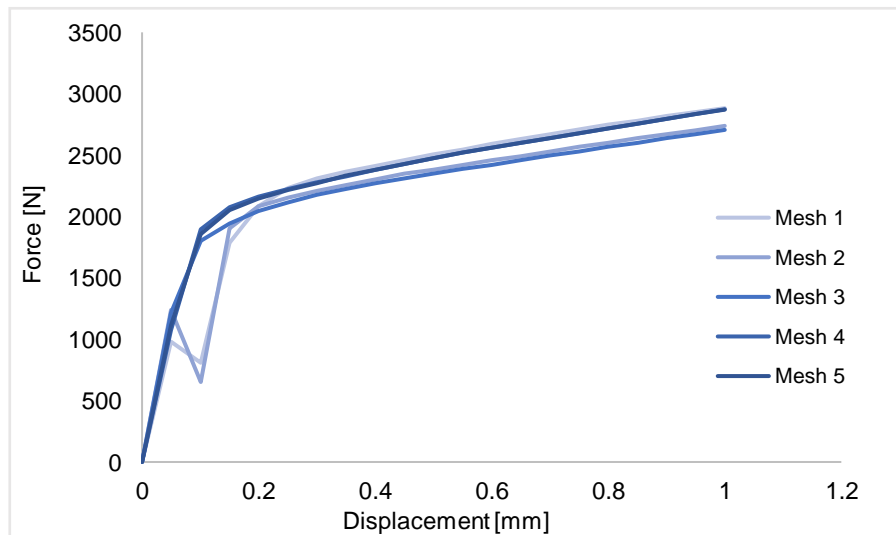


Figure 3.6 – Reaction force convergence analysis of the mesh with CTETRA4 elements

The convergence of the reaction force-displacement curves of the mesh with CTETRA10 elements can be seen in Figure 3.7.



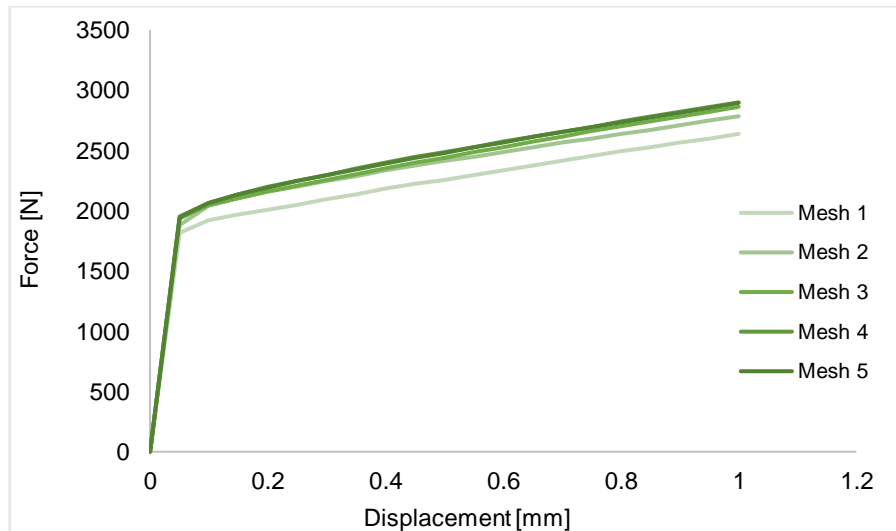


Figure 3.7 – Reaction force convergence analysis of the mesh with CTETRA10 elements

From the analysis of both Figure 3.6 and Figure 3.7, one can see that the second mesh generated with CTETRA10 elements showed a more consistent convergence than the first with CTETRA4. Also, it may appear that the curves with CTETRA10 elements show a “faster” convergence than with CTETRA4, but it should be noted that Mesh 2 from CTETRA10 elements already has more nodes than Mesh 4 from the previous element type, so that statement would not be entirely correct. Furthermore, CTETRA4 elements are tetrahedral first-order elements that are usually overly stiff for structural simulations, as for solving for displacement and stress, therefore CTETRA10 elements shall be used instead [110,111]. So, for this reason, and although simulations may take more computational time, CTETRA10 elements were chosen for all further simulations due to their better performance.

### 3.2.2. Relative density analysis

Initially, a relative density analysis was done to 3 cubic (C) lattice structures which consisted of  $2 \times 2 \times 2$  cells, with relative densities of 25%, 30% and 35% (shown in Figure 3.8), in order to find the one with the closest mechanical properties to those of bone and decide on what will be the relative density for the remaining topologies, accordingly.

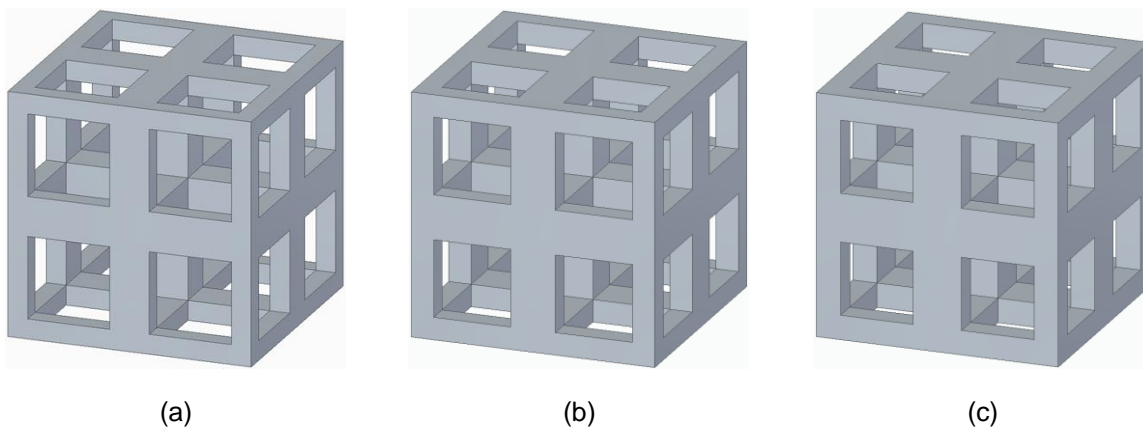


Figure 3.8 – Lattice structures used in the relative density analysis: (a) C-0.57; (b) C-0.64; (c) C-0.70

The unit cell parameters for each lattice are shown in Table 3.5, as well as its relative density and total model dimensions. The nomenclature that will be further used when referring to a particular topology is *topology abbreviation-strut size* (in mm), as can be observed in the same table.

Table 3.5 – Cubic unit cells and model characteristics for the preliminary relative density analysis

Geometry	Unit cell parameters			Model characteristics	
	Size (mm)	Strut (mm)	Pore (mm)	Total size (mm)	Relative density, $\rho$ (%)
C-0.57	3.50	0.57	2.36	7.00	24.92
C-0.64		0.64	2.22		30.34
C-0.70		0.70	2.10		35.20

The finite element analysis (FEA) implemented in this analysis consisted of a compression test with a total enforced displacement of 1 mm, as explained in the beginning of the section 3.2, and was performed on the mentioned laptop.

The characteristics of the successive meshes generated for the C-0.57 lattice structure and computation times are presented in Table 3.6.

Table 3.6 – C-0.57 mesh characteristics and solving computation time

Mesh	Element size [mm]	No. of elements	No. of nodes	Computation time
Mesh 1	1.00	2454	5863	7s
Mesh 2	0.50	5491	12250	18s
Mesh 3	0.30	17850	34315	1min3s
Mesh 4	0.25	28347	52927	4min5s
Mesh 5	0.23	42756	76898	8min24s

The characteristics of the successive meshes generated for the C-0.64 lattice structure and computation times are presented in Table 3.7.

Table 3.7 – C-0.64 mesh characteristics and solving computation time

Mesh	Element size [mm]	No. of elements	No. of nodes	Computation time
Mesh 1	1.00	2723	6476	9s
Mesh 2	0.50	5100	11183	17s
Mesh 3	0.30	20874	39173	2min51s
Mesh 4	0.25	38842	69434	8min56s
Mesh 5	0.23	47209	82715	11min47s

The characteristics of the successive meshes generated for the C-0.70 lattice structure and computation times are presented in Table 3.8.

Table 3.8 – C-0.70 mesh characteristics and computation solving time

Mesh	Element size [mm]	No. of elements	No. of nodes	Computation time
Mesh 1	1.00	2047	4836	7s
Mesh 2	0.50	6191	12988	20s
Mesh 3	0.30	29056	52657	4min45s
Mesh 4	0.25	38430	67829	7min53s
Mesh 5	0.23	58199	99599	16min59s

Following the methodology described in the beginning of section 3.2., the same situation was verified for all the structures, in the sense that no further refinement was needed beyond the Mesh 3, as these results showed the best balance between accuracy and computational cost, because there was enough evidence showing that they had converged.

Table 3.9 summarizes the characteristics of the Mesh 3 of each topology and associated computation time.

Table 3.9 – Comparison between Mesh 3 of each cubic topology

Topology	Element size [mm]	No. of elements	No. of nodes	Computation time
C-0.57	0.30	17850	34315	1min3s
C-0.64	0.30	20874	39173	2min51s
C-0.70	0.30	29056	52657	4min45s

The comparison between the engineering curves from the Mesh 3 of each lattice structure with the corresponding relative density and two different apparent densities of trabecular bone, that were presented in section 2.2.1, is shown in Figure 3.9. The area considered to obtain the engineering curves is always going to be the projected area of the models.

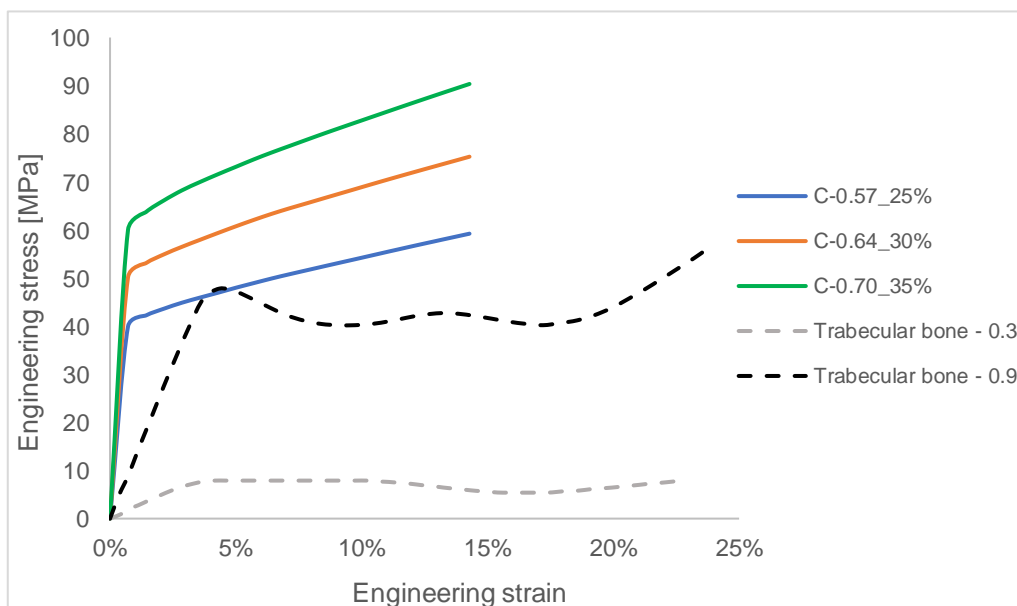


Figure 3.9 – Relative density analysis compared to trabecular bone properties

From the analysis of Figure 3.9, one can understand that the lattice structure that has the stress-strain values closest to any of the apparent densities of the trabecular bone is the C-0.57. For this reason, it was decided that every topology would have a relative density close to 25%.

**3.2.3. Topology analysis**

After defining 25% as the approximate relative density for every topology, a preliminary sensitivity analysis was done on every unit cell topology on smaller lattice structures, consisting of 2 x 2 x 2 cells and shown in Figure 3.10. These smaller scale analyses were performed so that the computational cost would be mitigated as much as possible, by trying to obtain the element size of the meshes that showed the best balance between accuracy of results and computational cost. This analysis will be extrapolated for the full models.

In this way and in accordance with the methodology described and exemplified in the beginning of section 3.2, an enforced displacement of 1 mm was imposed on the top face of each lattice and the convergence analysis was performed. Most of these simulations were conducted on the laptop but for some of the later refinements of the more complex lattices (namely, TO, RCO and RTCO topologies), it was resorted to the desktop PC. The computation times will be highlighted when it was resorted to the desktop PC.

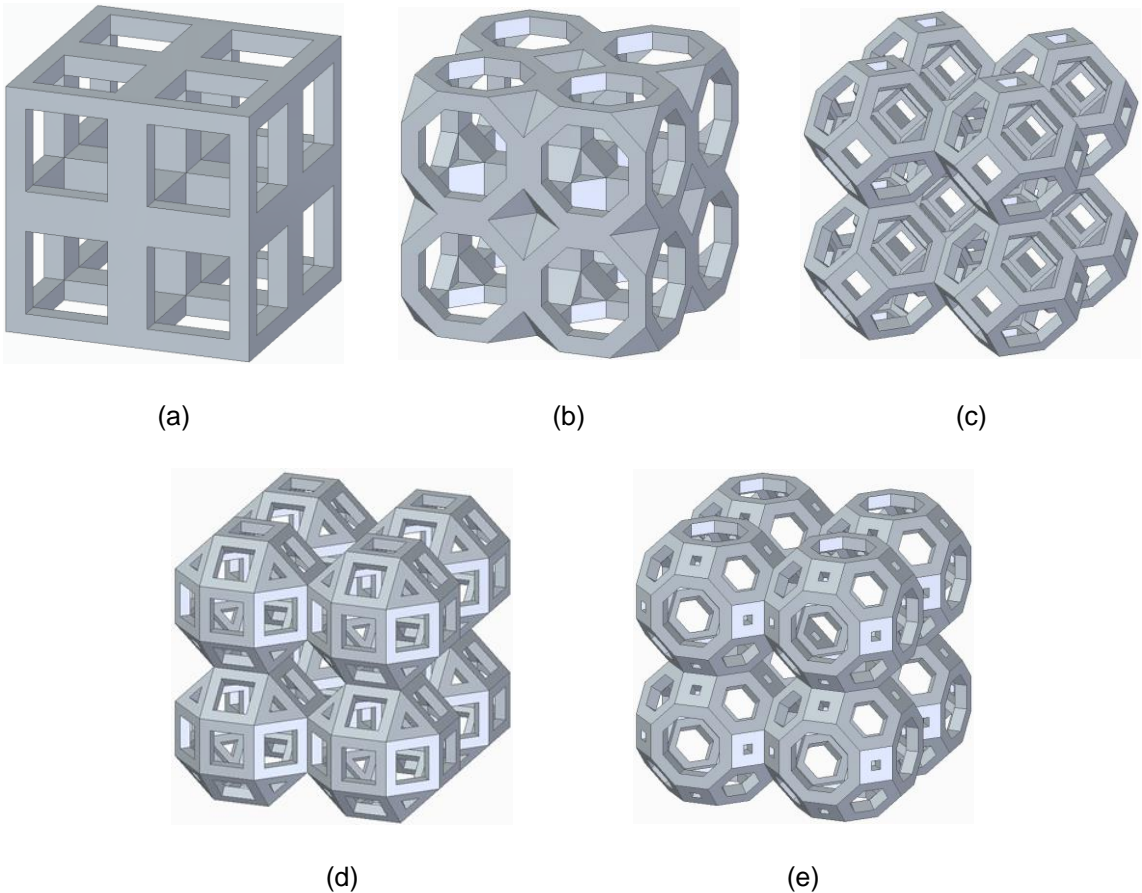


Figure 3.10 – Lattice structures 2 x 2 x 2: (a) C-0.57; (b) TC-0.50; (c) TO-0.33; (d) RCO-0.28; (e) RTCO-0.33

The unit cell parameters for each lattice structure are shown in Table 3.10, as well as the relative density and total model dimensions.

Table 3.10 – Unit cells and model characteristics for the preliminary topology analysis

Topology	Unit cell parameters		Model characteristics	
	Size (mm)	Strut (mm)	Total size (mm)	Relative density, $\rho$ (%)
C-0.57	3.50	0.57	7.00	24.92
TC-0.50		0.50		24.81
TO-0.33		0.33		24.35
RCO-0.28		0.28		24.58
RTCO-0.33		0.33		25.32

The characteristics of the successive meshes generated for the C-0.57 lattice structure and computation times were already presented in Table 3.6, in section 3.2.2. As it was already mentioned as well, the Mesh 3 was the chosen for this topology, with an element size of 0.30 mm. Figure 3.11 shows the results of the effective strain in the elements of the chosen mesh.

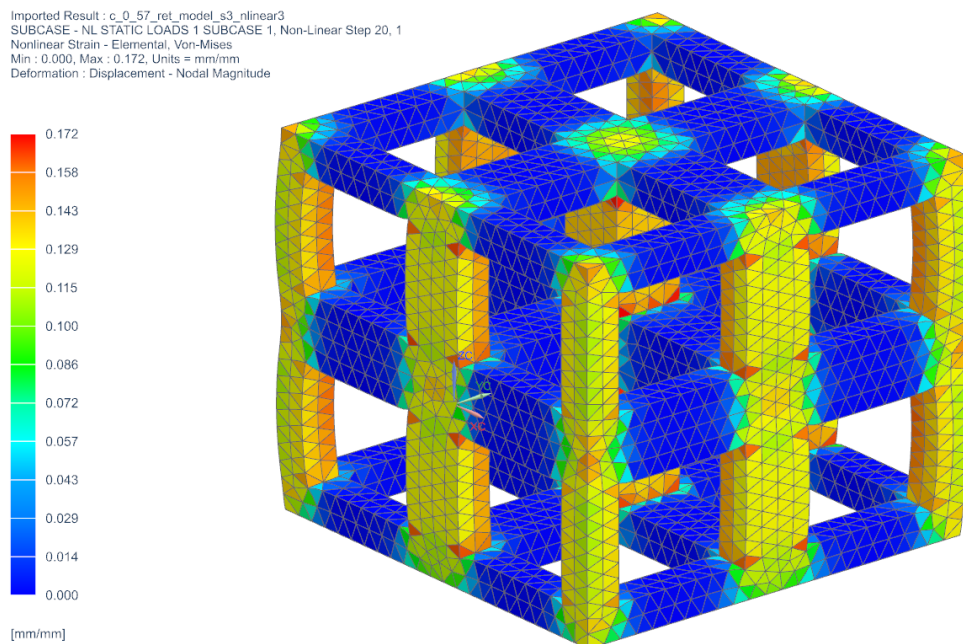


Figure 3.11 – Effective strain in the elements of the Mesh 3 of C-0.57

The characteristics of the successive meshes generated for the TC-0.50 lattice structure and computation times are presented in Table 3.11.

Table 3.11 – TC-0.50 mesh characteristics and computation solving time

Mesh	Element size [mm]	No. of elements	No. of nodes	Computation time
Mesh 1	1.00	3146	7412	11s
Mesh 2	0.50	4844	10523	15s
Mesh 3	0.30	23345	44579	2min44s
Mesh 4	0.20	57466	102670	11min50s

For the topology TC-0.50, Mesh 3 was chosen, with an element size of 0.30 mm. Figure 3.12 shows the results of the effective strain in the elements of the chosen mesh for the TC-0.50 topology.

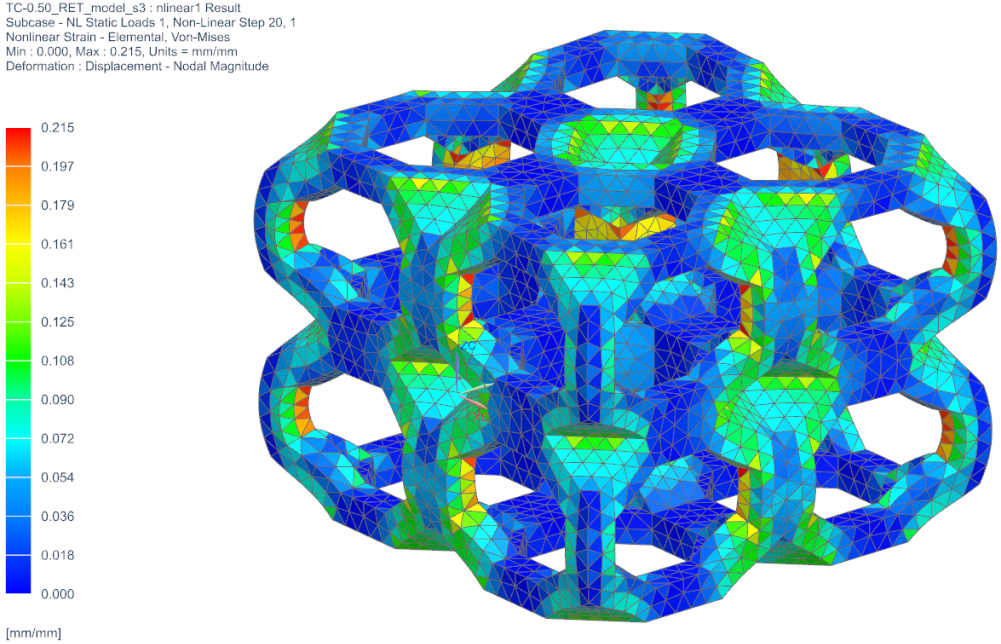


Figure 3.12 – Effective strain in the elements of the Mesh 3 of TC-0.50

The characteristics of the successive meshes generated for the TO-0.33 lattice structure and computation times are presented in Table 3.12.

Table 3.12 – TO-0.33 mesh characteristics and computation solving time, (\*) indicates solving times of simulations performed on the desktop PC

Mesh	Element size [mm]	No. of elements	No. of nodes	Computation time
Mesh 1	1.00	8075	17364	29s
Mesh 2	0.50	18639	36366	1min19s
Mesh 3	0.30	30663	58211	5min17s
Mesh 4	0.25	58252	103000	13min26s
Mesh 5	0.20	109143	184137	44min53s
Mesh 6	0.15	223669	357994	11min58s*
Mesh 7	0.12	369922	575817	20min48s*
Mesh 8	0.10	676909	1022954	1h24min*
Mesh 9	0.08	1232392	1822671	4h5min*

For the topology TO-0.33, Mesh 7 was chosen, with an element size of 0.12 mm. Figure 3.13 shows the results of the effective strain in the elements of the chosen mesh for TO-0.33 topology.



TO-0.33\_RET\_model\_s7 : nlinear7 Result  
 Subcase - NL Static Loads 1, Non-Linear Step 20, 1  
 Nonlinear Strain - Elemental, Von-Mises  
 Min : 0.000, Max : 0.259, Units = mm/mm  
 Deformation : Displacement - Nodal Magnitude

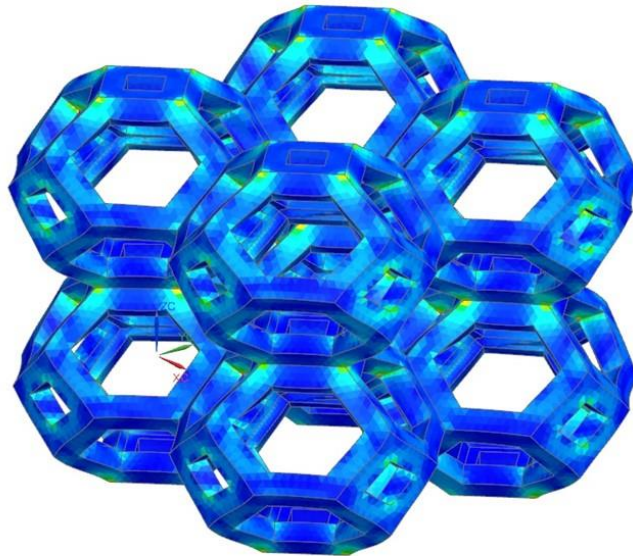


Figure 3.13 – Effective strain in the elements of the Mesh 7 of TO-0.33

The characteristics of the successive meshes generated for the RCO-0.28 lattice structure and computation times are presented in Table 3.13.

Table 3.13 – RCO-0.28 mesh characteristics and computation solving time, (\*) indicates solving times of simulations performed on the desktop PC

Mesh	Element size [mm]	No. of elements	No. of nodes	Computation time
Mesh 1	1.00	10184	23867	37s
Mesh 2	0.40	16584	37899	1min1s
Mesh 3	0.25	26933	58283	4min10s
Mesh 4	0.20	52723	105426	11min40s
Mesh 5	0.15	93123	175045	29min37s
Mesh 6	0.12	215660	378790	11min49s*
Mesh 7	0.10	365052	622316	21min23s*
Mesh 8	0.08	607775	999102	1h3min*

For the topology RCO-0.28, Mesh 7 was chosen, with an element size of 0.10 mm. Figure 3.14 shows the results of the effective strain in the elements of the chosen mesh for the RCO-0.28 topology.

RCO-0.28\_RET\_model\_s7 : nlinear7 Result  
 Subcase - NL Static Loads 1, Non-Linear Step 20, 1  
 Nonlinear Strain - Elemental, Von-Mises  
 Min : 0.000, Max : 0.405, Units = mm/mm  
 Deformation : Displacement - Nodal Magnitude

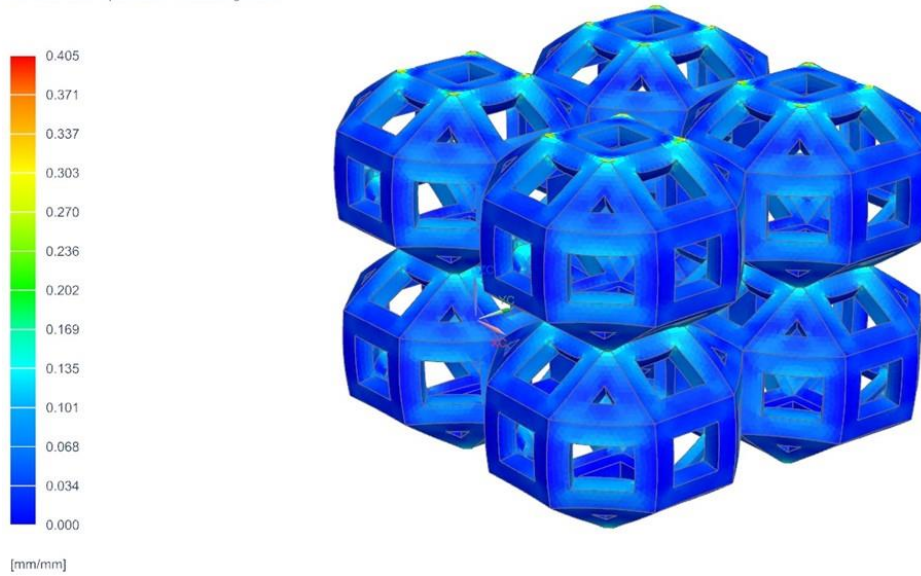


Figure 3.14 – Effective strain in the elements of the Mesh 7 of RCO-0.28

The characteristics of the successive meshes generated for the RTCO-0.33 lattice structure and computation times are presented in Table 3.14.

Table 3.14 – RTCO-0.33 mesh characteristics and computation solving time, (\*) indicates solving times of simulations performed on the desktop PC

Mesh	Element size [mm]	No. of elements	No. of nodes	Computation time
Mesh 1	1.00	13451	30164	47s
Mesh 2	0.28	23413	51670	3min38s
Mesh 3	0.24	42976	86847	11min30s
Mesh 4	0.20	56626	111446	14min30s
Mesh 5	0.15	94117	179085	38min22s
Mesh 6	0.12	190142	333805	10min37s*
Mesh 7	0.10	349319	593614	22min*
Mesh 8	0.08	667415	1090673	1h20min*
Mesh 9	0.06	1407810	2212903	7h*
Mesh 10	0.05	2414926	3722573	15h24min*

For the topology RTCO-0.33, Mesh 8 was chosen, with an element size of 0.08 mm. Figure 3.15 shows the results of the effective strain in the elements of the chosen mesh for the RTCO-0.33 topology.



RTCO-0.33\_RET\_model\_s8 : nlinear8 Result  
 Subcase - NL Static Loads 1, Non-Linear Step 20, 1  
 Nonlinear Strain - Elemental, Von-Mises  
 Min : 0.000, Max : 0.241, Units = mm/mm  
 Deformation : Displacement - Nodal Magnitude

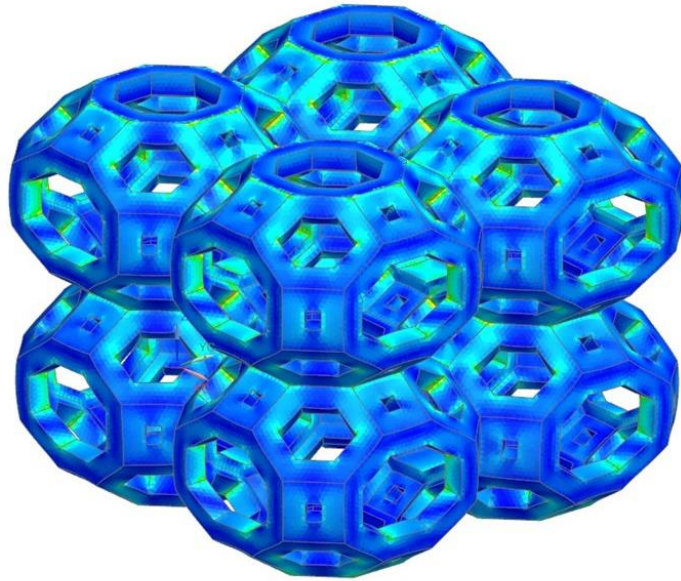


Figure 3.15 – Effective strain in the elements of the Mesh 8 of RTCO-0.33

Table 3.15 summarizes the characteristics of the meshes chosen for each topology and associated computation time, from which the element size is the most important value to retain for the analyses of the full models.

Table 3.15 – Summary of the chosen mesh characteristics for each topology and computation solving times, (\*) indicates solving times of simulations performed on the desktop PC

Topology	Element size [mm]	No. of elements	No. of nodes	Computation time
C-0.57	0.30	17850	34315	1min3s
TC-0.50	0.30	23345	44579	2min44s
TO-0.33	0.12	369922	575817	20min48s*
RCO-0.28	0.10	365052	622316	21min23s*
RTCO-0.33	0.08	667415	1090673	1h20min*

### 3.3. Experimental work

Experimental work was performed on the cubic (C) and truncated cube (TC) topologies, in order to validate the numerical models.

The International Standard ISO 13314:2011 [112], on *Compression test for porous and cellular metals*, was used for this purpose, as it is indicated for the mechanical testing of porous and cellular metallic materials with a porosity of 50% or more, even though it is not specifically designated for lattice structures produced by AM [89].

The prescribed geometry for the test specimens from this standard can be seen in Figure 3.16, wherein all spatial dimensions ( $W_0$  and  $D_0$ ) shall be at least 10 times the average pore size,  $d_a$ , and less than 10 mm, so as to minimize edge effects. Besides, the sample length to diameter ratio ( $H_0:D_0$ ) or sample length to edge length ratio ( $H_0:W_0$ ) should be between 1 and 2. So, in order to comply with the

standard, it was chosen that the final models to be analysed would have a lattice structure of 10 x 10 x 10 cells, for the different topologies.

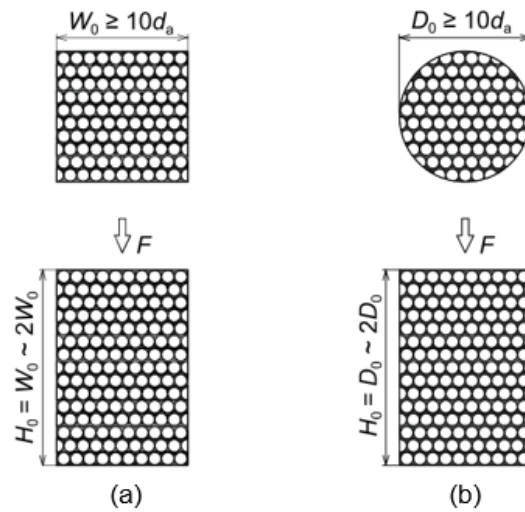


Figure 3.16 – Schematic illustration of a test specimen, according to ISO 13314:2011: (a) rectangular specimen and (b) cylindrical specimen [112]

The specimens were manufactured by laser powder bed fusion (L-PBF) in the company Erofio, located in Batalha, in a X Line 2000R from General Electrics, presented in Figure 3.17.



Figure 3.17 – X Line 2000R from General Electrics [113]

A summary of the main characteristics of this L-PBF machine are presented in Table 3.16, below.

Table 3.16 – Main characteristics of the X Line 2000R from General Electrics [113]

Characteristic	Dimensions
Build volume	800 x 400 x 500 mm
Layer thickness	30 – 150 $\mu\text{m}$
Production speed	up to 120 $\text{cm}^3/\text{h}$
Laser power	2 x 1000 W
Max scanning speed	7 m/s
Focus diameter	Approx. 100 – 500 $\mu\text{m}$

The material available in the company Erofio for the manufacturing of the specimens was the 316 stainless steel. Due to this limitation, the specimens for the experimental work were manufactured in this material for the lattice structures with the cubic (C) and truncated cube (TC) unit cells. For this reason, additional numerical simulations for this new material were also performed.

The mechanical properties of the 316 stainless steel that were further considered for the numerical simulations were obtained from Kweon et al. [114], who found that the true stress and true strain curve equation that best correlates with experimental data is:

$$\bar{\sigma} = 1617 - 948.3 \exp(-1.441 \bar{\epsilon}^{0.229}) \text{ MPa} \quad (3.8)$$

The manufacturing parameters used for the fabrication of the specimens are presented in Table 3.17.

Table 3.17 – Manufacturing parameters for the specimens [113]

Parameter	
Atmosphere	nitrogen
Layer thickness	50 $\mu\text{m}$
Build rate	19.9 $\text{cm}^3/\text{h}$
Melting rate per laser	23.4 $\text{cm}^3/\text{h}$

In total, six specimens were fabricated and later tested: 3 specimens with the cubic (C) unit cell and 3 specimens with the truncated cube (TC) unit cell.

### 3.3.1. Compression tests

Compression tests were performed at room temperature on the hydraulic testing machine presented in Figure 3.18, which is an *Instron SATEC 1200* that has a load cell of 1200 kN. The test was conducted at constant speed of 2.5 mm/min, following the standard ISO 13314:2011 [112], and *Bluehill Software* was used for both data interpretation and recording. Teflon sheets with a thickness of 0.5 mm were used on top and at the bottom of the specimens with lubrication purposes so that very low friction between the specimen and the compression plates is guaranteed.

The three specimens from each topology were compressed. Two from each topology were only tested until the displacement was close to the 5 mm that were considered for the numerical simulations, reaching to a total engineering strain of 14.29%, while the remaining specimen from each of the topologies was compressed beyond this point.



Figure 3.18 – Hydraulic testing machine *Instron SATEC 1200*

The structure of the compression machine is very tall and the shaft that produces the compression of the specimens is also very long. Due to this, even though this shaft should be rigid, it may suffer some elastic deformation while compressing the specimens, which can compromise the results obtained for the displacement. For this reason, a dry-run test was performed, without any specimen between the planes of the setup, to register the mentioned behaviour. After this procedure, it was possible to correct the displacement values in the force-displacement curves, as is shown in Appendix A – Correction of the force-displacement experimental curves.

## 4. Results and discussion

Following the methodology described in section 3.2, an element size was selected for each topology, which was diligently summarized in Table 3.15. As already mentioned, the full models consist of 10 x 10 x 10 cells and the characteristics of these models are summarized in Table 4.1. The meshes generated to discretize the model of each topology were defined to have the selected element size.

Table 4.1 – Unit cells and model characteristics for the full model analysis

Topology	Unit cell parameters		Model characteristics	
	Size (mm)	Strut (mm)	Total size (mm)	Relative density, $\rho$ (%)
C-0.57	3.50	0.57	35.00	24.92
TC-0.50		0.50		24.81
TO-0.33		0.33		24.35
RCO-0.28		0.28		24.58
RTCO-0.33		0.33		25.32

For these simulations, the total engineering strain of 14.29% obtained in the preliminary analyses (section 3.2) was kept constant, so that the results could be compared. For this, an enforced displacement of 5 mm was imposed, divided in 20 iterations of 0.25 mm.

This chapter presents the results obtained in the numerical simulations of the full models, the results of the experimental tests performed on the specimens manufactured by L-PBF that were presented in 3.3, and the experimental assessment of the numerical models.

### 4.1. Numerical analysis of the full models

The FEA of the full models revealed to have an excessive computational cost, as the meshes generated with the element size selected in section 3.2 had a number of elements and nodes that was very high (more than 3.5M nodes just for the cubic topology, which is the least complex geometry). So, in order to perform the analyses, a simplification of the numerical model was needed.

The solution found was to impose symmetry boundary conditions (BCs) where it was possible, so that there were less elements and nodes in the mesh, resulting in less computational time.

The numerical model of the compression tests has two mid-planes that show symmetry and could pose as the location of the intended BCs, see Figure 4.1. Considering both symmetric conditions, it is possible to reduce the model to a quarter of the full model, which will decrease quite significantly the computation time required to solve the FEA.

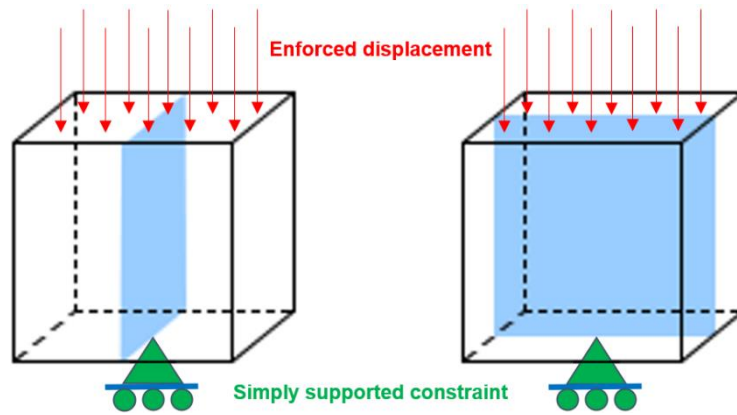


Figure 4.1 – Mid planes where symmetry boundary conditions can be imposed, adapted from [115]

To evaluate the feasibility of considering only a quarter of the numerical model in all the simulations, the C-0.57 topology was considered, and the numerical results for full, half and a quarter of the model were compared. Firstly, the full model of the lattice structure, Figure 4.2 (a), was analysed, followed by only half (using one symmetry BC), Figure 4.2 (b), and, later, a quarter of the model (using both symmetry BCs), Figure 4.2 (c).

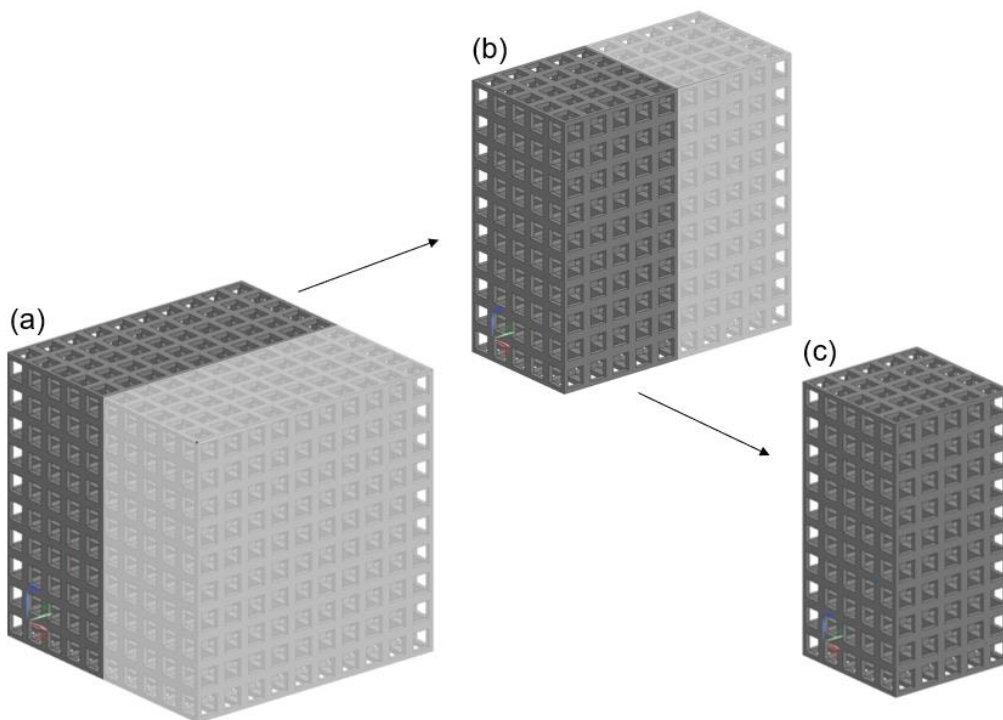


Figure 4.2 – Illustration of the C-0.57 structures analysed: (a) full model; (b) half model; (c) quarter of a model

The mesh generated for each of the numerical models was designed to have an element size of 0.3 mm, just as selected in section 3.2. Table 4.2 summarizes the mesh characteristics for the full, half and quarter of the model, along with the associated computation times.

Table 4.2 – Mesh characteristics and computation solving time for the full, half and quarter of model, (\*) indicates solving times of simulations performed on the desktop PC

C-0.57	Element size [mm]	No. of elements	No. of nodes	Computation time
Full model	0.30	2180040	3794685	12h28min*
Half model		1091789	1917436	2h44min*
Quarter of model		545477	966991	54min15s*

As can be seen in Table 4.2, the introduction of the symmetry BCs significantly reduces the number of elements and consequent nodes in the mesh, which culminates in a very significant reduction in the computation times.

Furthermore, the force-displacement curves of each model were plotted in Figure 4.3, so that they could be compared. The values obtained for the half model and quarter of the model had to be corrected, in order to be comparable to the full model results, by multiplying their values of force by 2 and 4, respectively. It can also be observed that the curves of the three models are completely overlapped, which means that the results simulating a quarter of the model and imposing the symmetric constraints in the symmetry planes considered allows to achieve accurate results, with significantly lower computational cost.

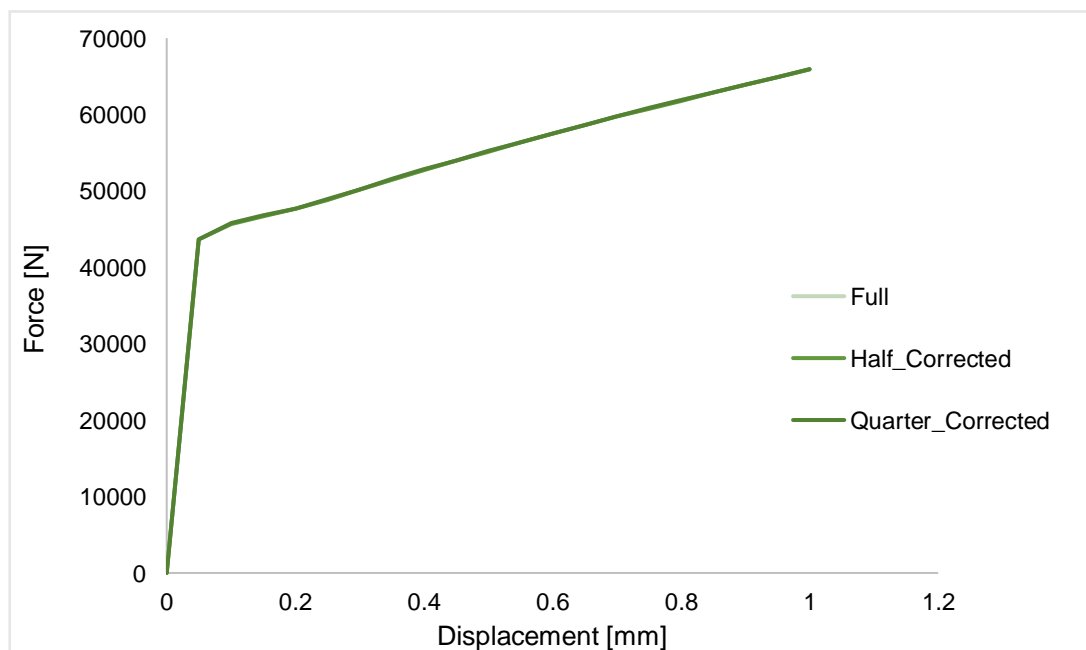


Figure 4.3 – Reaction force-displacement curves obtained from the full, half and quarter of a model

Besides the simplification done in the models by introducing symmetric constraints, which allowed to obtain the results for the full models at a much lower computational cost, a convergence analysis was performed on a quarter of the same topology, in order to validate the use of the element size previously determined in section 3.2. For this analysis, two more meshes were generated: Mesh 1, which was coarser than the initial one, with an element size of 0.5 mm; and Mesh 3, more refined, with an element size of 0.25 mm, just like the element sizes used before in section 3.2. Table 4.3 shows the characteristics and computation solving times of these meshes.

Table 4.3 – C-0.57 mesh characteristics and computation solving time, (\*) indicates solving times of simulations performed on the desktop PC

Mesh	Element size [mm]	No. of elements	No. of nodes	Computation time
Mesh 1	0.5	149579	308684	7min16s*
Mesh 2	0.3	545226	966687	55min24s*
Mesh 3	0.25	847901	1474117	1h49min*

This convergence analysis considered the convergence of the effective stress for a given node of the mesh through the refinements and the convergence of the reaction force response in the base of each lattice to the enforced displacement on the top face.

In Table 4.4 are presented the successive values obtained for the effective stress through the refinements in the selected node 308633 (which is always located in the same spot) along with the relative error.

Table 4.4 – Effective stress values obtained for the selected node 308633 through the refinements of the quarter of the full lattice structure C-0.57 and the associated relative error

Node ID - 308633	Element size [mm]	Effective stress [MPa]	Relative error [%]
Mesh 1	0.5	347.84	0.31%
Mesh 2	0.3	346.77	0.49%
Mesh 3	0.25	348.49	-

In Figure 4.4 is presented the convergence analysis of the effective stress, in regards to the chosen node 308633, along the successive refinements.

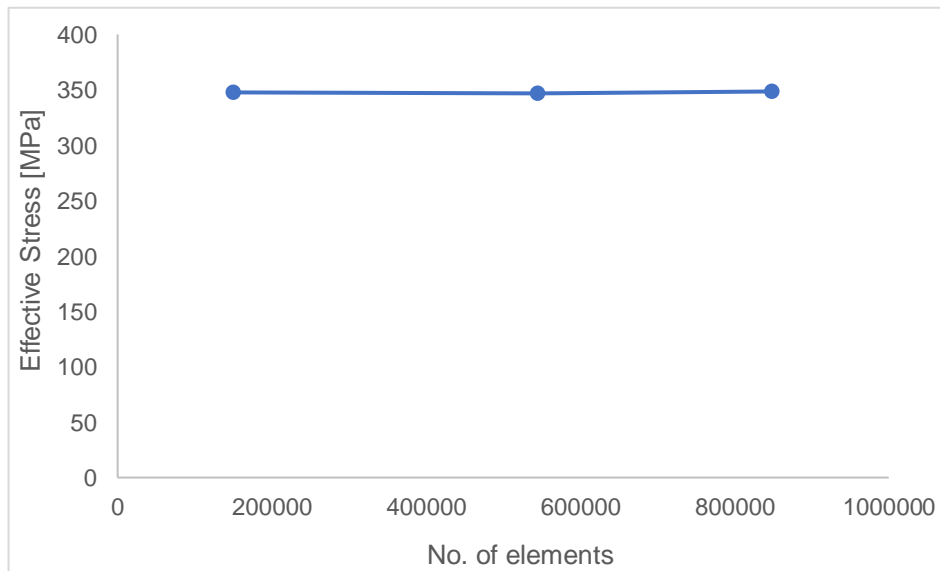


Figure 4.4 – Convergence analysis of the effective stress on node 308633 of C-0.57

As can be seen in both Table 4.4 and Figure 4.4, the variation of the result obtained from Mesh 1 to the Mesh 2 is 0.31% and from the Mesh 2 to the Mesh 3 is 0.49%, which are very negligible values that allow to say that the effective stress value on node 308633 has converged.



In Figure 4.5, the force-displacement curves obtained for the three meshes considered in this convergence analysis are presented. In this figure, it can be seen that although there is a slight noticeable variation in the transition from the elastic to the plastic regime for the curve of the Mesh 1, it should also be noted that the curves from Mesh 2 and 3 are completely overlapped.

Since both the effective stress and the reaction force values showed to have converged, it is fair to assume that the values obtained for the element size of every topology, in section 3.2, can be extrapolated for the generation of the mesh of the full models.

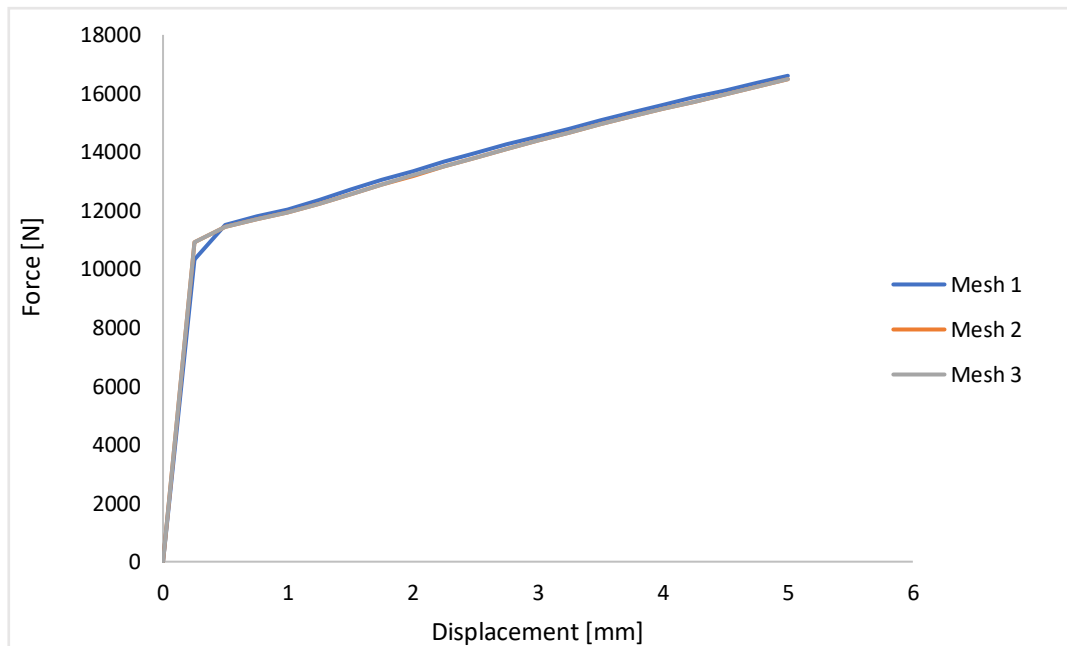


Figure 4.5 – Convergence analysis of the reaction force in the C-0.57 lattice structure

These results permit concluding that the analysis of a quarter of the full model can obtain accurate results when the mesh is generated using the element size selected in section 3.2, with a significative reduction of the computational time.

## 4.2. Numerical analysis of the topologies

The numerical results obtained in the simulations of the models from each topology are presented in this section. All simulations were performed in a quarter of the full model and it was intended that the size of the elements generated in every mesh would follow the results from section 3.2.

### 4.2.1. Cubic and Truncated Cube topologies

For cubic (C) and truncated cube (TC) topologies it was possible to obtain results for the meshes generated with the element size selected in section 3.2. The characteristics of the meshes and associated computation times of both topologies are presented in Table 4.5.

Table 4.5 – C-0.57 and TC-0.50 mesh characteristics and computation solving times, (\*) indicates solving times of simulations performed on the desktop PC

Topology	Element size [mm]	No. of elements	No. of nodes	Computation time
C-0.57	0.3	545226	966687	55min24s*
TC-0.50	0.3	727983	1303171	1h29min*

An illustration of the results obtained for the effective strain of both C-0.57 and TC-0.50 lattice structures is presented in Figure 4.6 (a) and (b), respectively.

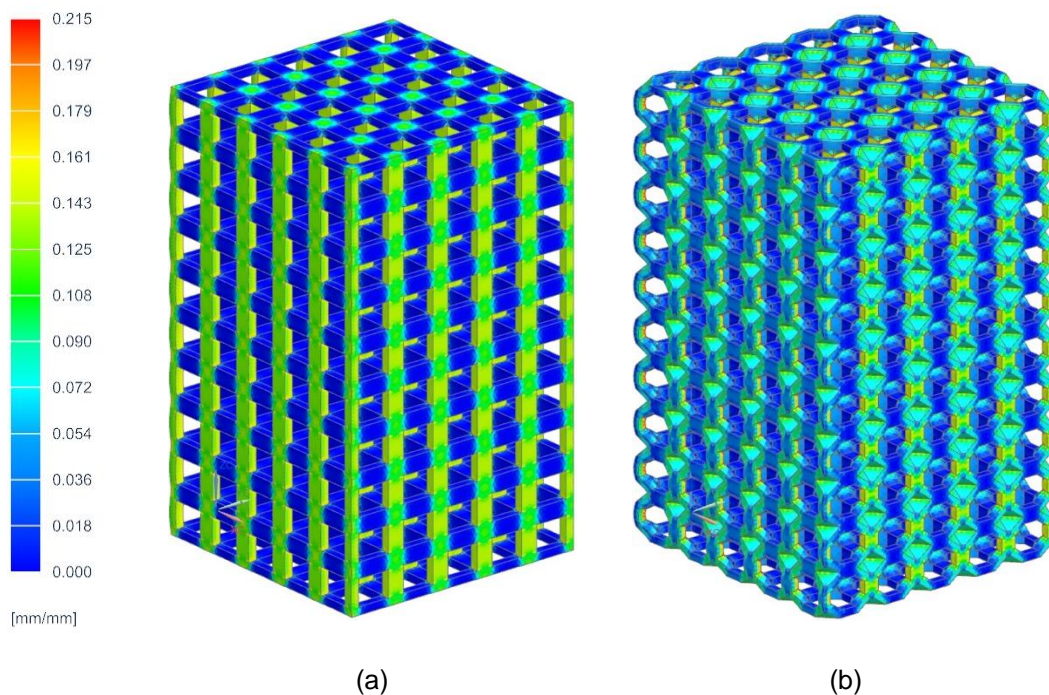


Figure 4.6 – Effective strain in the elements of the lattice structure: (a) C-0.57 and (b) TC-0.50

From observing the illustrations presented in Figure 4.6, one can tell that for the same situation and boundary conditions, the TC topology sustained higher levels of effective strain than those of C. In these results, the maximum value of effective strain sustained by the C-0.57 lattice was 0.172, while in the TC-0.50 the value of 0.209 was reached.

#### 4.2.2. Truncated Octahedron, Rhombicuboctahedron and Rhombitruncated Cuboctahedron topologies

For the truncated octahedron (TO), rhombicuboctahedron (RCO) and rhombitruncated cuboctahedron (RTCO) topologies, it was not possible to obtain results for the meshes generated with the element size selected in section 3.2, as the number of elements and nodes revealed to be too high to be computed. For example, for an element size of 0.14 mm, the mesh generated for the RTCO topology has more than 4.3 M elements and required more than 1.2 TB of memory in the disk (maximum space available) to solve the numerical simulation.

For this reason, the objective for this lattice structures was to obtain results for the most refined meshes as possible for each topology. The characteristics of the most refined meshes from which was possible to obtain results for each of these topologies and the associated computation times are presented in Table 4.6.

Table 4.6 – TO-0.33, RCO-0.28 and RTCO-0.33 mesh characteristics and computation solving times, (\*) indicates solving times of simulations performed on the desktop PC

Topology	Element size [mm]	No. of elements	No. of nodes	Computation time
TO-0.33	0.15	3747283	6807093	23h56min*
RCO-0.28	0.16	3839962	7168275	29h24min*
RTCO-0.33	0.15	2966889	5543400	22h1min*

An illustration of the results obtained for the effective strain of the TO-0.33, RCO-0.28 and RTCO-0.33 lattice structures is presented in Figure 4.7 (a), (b) and (c), respectively.

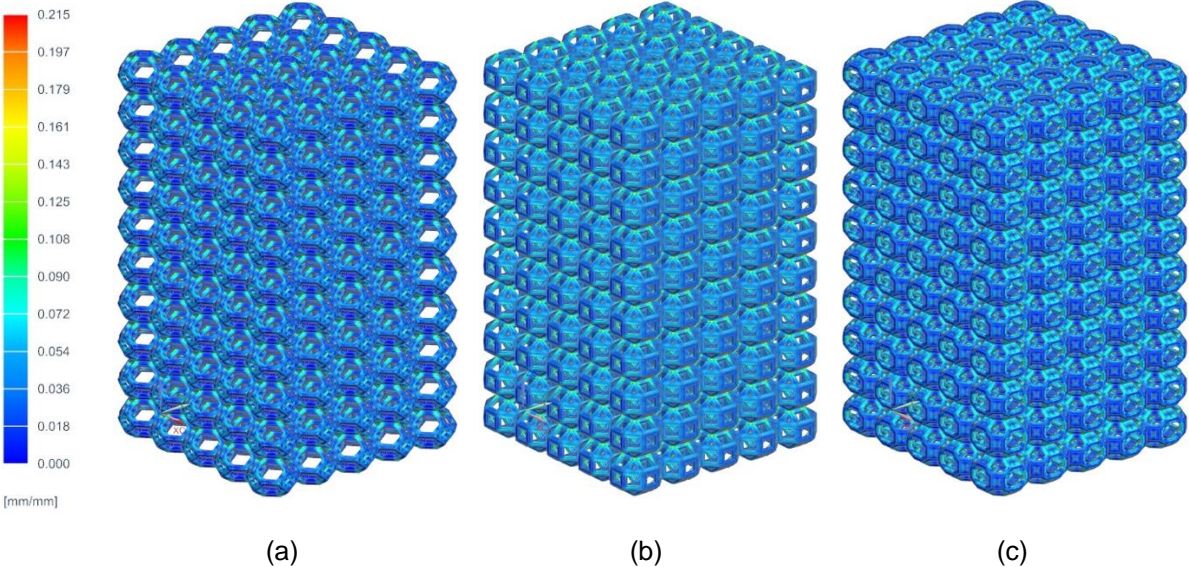


Figure 4.7 – Effective strain in the elements of the lattice structure: (a) TO-0.33, (b) RCO-0.28 and (b) RTCO-0.33

From the observation of the colour gradient in the illustrations presented in Figure 4.7, it is possible to say that the RCO topology is the one that sustains the largest levels of effective strain, contrarily to the RTCO which sustains the lowest, while subjected to the same boundary conditions as the other topologies. In these results, the maximum values of effective strain sustained were 0.210, 0.215 and 0.147, for the lattices TO-0.33, RCO-0.28 and RTCO-0.33, respectively.

Due to the fact that the element size defined to generate the meshes for these topologies did not reach the values selected in section 3.2, it is expected that the results here obtained are not as accurate as the ones reached for the C and TC topologies.

### 4.2.3. Comparison with the trabecular bone

The comparison between the engineering curves obtained from the numerical simulations for each topology and the trabecular bone, for two different values of apparent density presented in section 2.2.1, is shown in Figure 4.8.

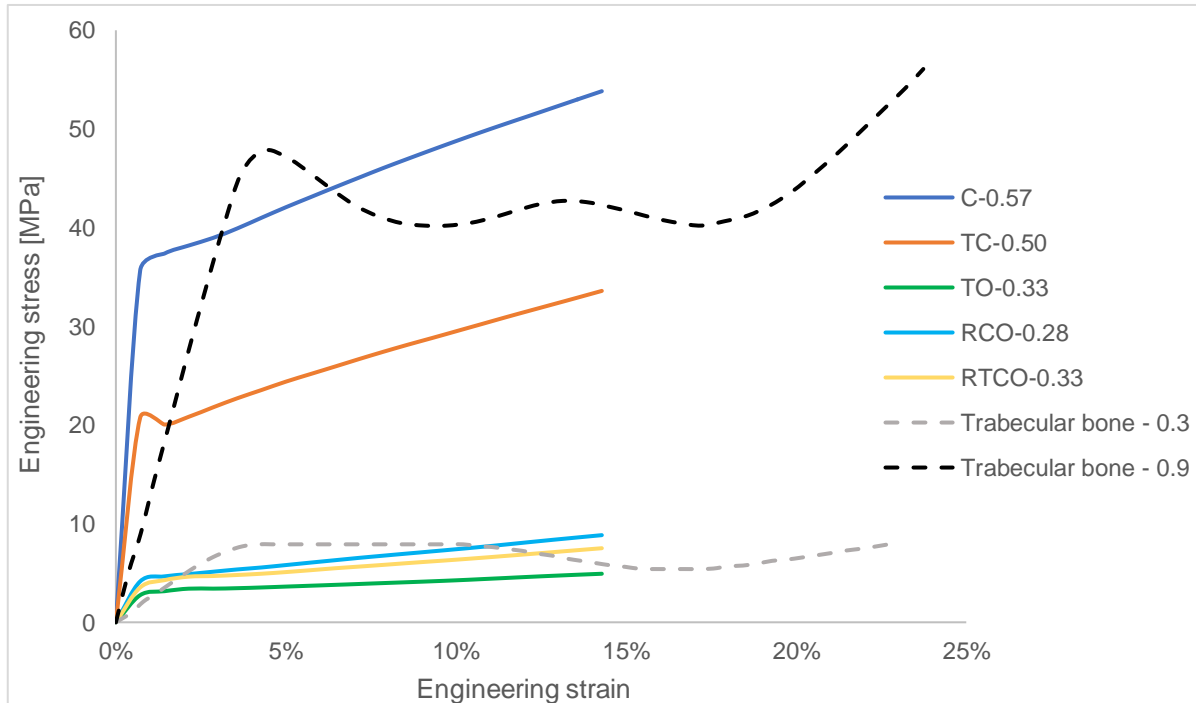


Figure 4.8 – Engineering curves from every topology compared to trabecular bone

In this figure, it is possible to observe that the C topology is the closest to the trabecular bone of  $0.9 \text{ g/cm}^3$ , the TO, RCO and RTCO topologies have their curves closer to the trabecular bone with an apparent density of  $0.3 \text{ g/cm}^3$ , while TC is positioned in between both curves of the trabecular bone. Even though the curves from TO, RCO and RTCO may be very close to the trabecular bone of  $0.3 \text{ g/cm}^3$ , they do not actually reach the maximum engineering stress that this trabecular bone experiences.

As there is a wide range of values that can be reached in the porosity of the trabecular bone (as mentioned in section 2.2.1), it is expected other engineering curves will be located in-between the ones illustrated in Figure 4.8. For this reason and due to the fact that the curves of TO, TCO and RTCO don't reach the maximum engineering stress of the weakest trabecular bone represented, it would make more reasonable to choose the C and TC topologies to be experimentally tested.

Besides, not only the numerical results obtained for the C and TC topologies are more accurate than those for the remaining topologies, but also the experimental tests were performed on specimens with a different material than the one used in these numerical models, so it would be wise to choose the least complex topologies that result in less computational time for the further simulations needed.

Consequently, the topologies chosen to perform the experimental tests were the cubic (C) and truncated cube (TC).

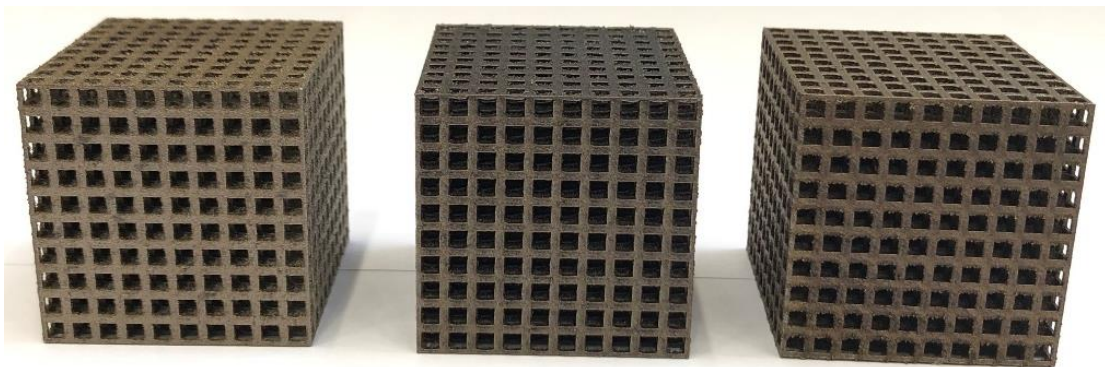


Unfortunately, no further comparisons with the bone will be performed, as the material in which the specimens were fabricated was not iron, and the experimental tests were only performed to validate the numerical models.

### 4.3. Experimental work results

In this section, the results from the experimental tests performed on the specimens manufactured by L-PBF as well as the experimental assessment of the numerical models will be presented and further explored.

As mentioned in section 3.3, six specimens in total were fabricated and tested: 3 specimens with the cubic (C) unit cell – C1, C2 and C3, shown in Figure 4.9 (a); and 3 specimens with the truncated cube (TC) unit cell – TC1, TC2 and TC3, shown in Figure 4.9 (b).



(a)



(b)

Figure 4.9 – Test specimens: (a) Cubic specimens C1, C2 and C3; (b) Truncated cube specimens TC1, TC2 and TC3

#### 4.3.1. Compression test specimens

After taking a closer look at each specimen, some irregularities on the specimens' external surfaces were visible, such as burrs and sharp edges, which are somewhat possible to see in both cubic (C) and truncated cube (TC) specimens showed in Figure 4.10 (a) and (b), respectively. For this reason, measurements of the external struts, of each specimen were taken using the measuring microscope

TM-500 from Mitutoyo. For each specimen, three measurements were taken at three measuring points in three different faces, and an average dimension of the strut,  $\bar{t}$ , was obtained for each of the topologies.

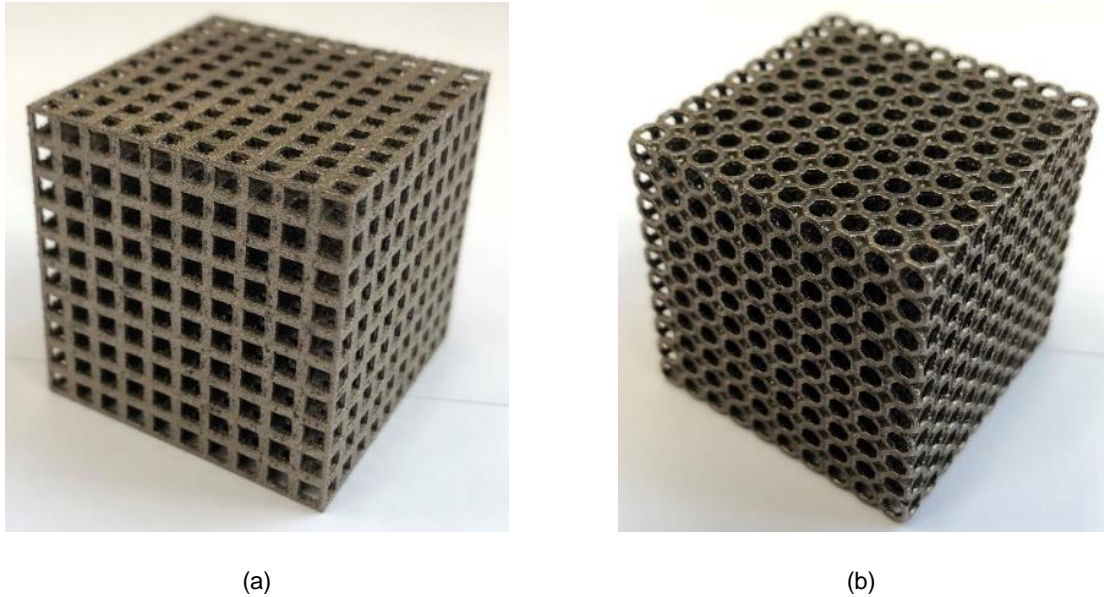


Figure 4.10 – Specimens from the topologies selected: (a) cubic and (b) truncated cube

Figure 4.11 (a) and (b) show some of the defects found in the specimens of the C and TC topologies, respectively.



Figure 4.11 – Defects found on the lattice structure of topology: (a) C and (b) TC; (c) shows the average strut size measured for each topology

In Table 4.7 is presented the designed strut dimensions and the average strut size measured in the specimens of each topology.

Table 4.7 – Comparison between designed strut dimensions and the struts from the specimens

Topology	Designed CAD strut	Average strut size, $\bar{t}$ [mm]
Cubic (C)	1.140	1.406
Truncated Cube (TC)	1.000	1.198

### 4.3.2. Compression tests results

As stated in section 3.3.1, two specimens from each topology were tested only until the displacement was close to 5 mm – C2, C3, TC1 and TC3, which was the value considered for the enforced displacement in the numerical simulations, while the remaining specimens – C1 and TC2 – were compressed further beyond this point. The true value of the displacements, meaning it was already corrected from the elastic deformation of the pressing tool, performed in each specimen are specified in Table 4.8.

Table 4.8 – Displacement performed in each of the specimens

Topology	Specimen	Displacement [mm]
C	C1	10.190
	C2	4.921
	C3	5.883
TC	TC1	5.271
	TC2	14.473
	TC3	5.164

In Figure 4.12 are shown the compression specimens after being tested. The white sheet present on the top face in some of them corresponds to Teflon sheets used during the compression tests with lubrication purposes, which was not possible to remove.

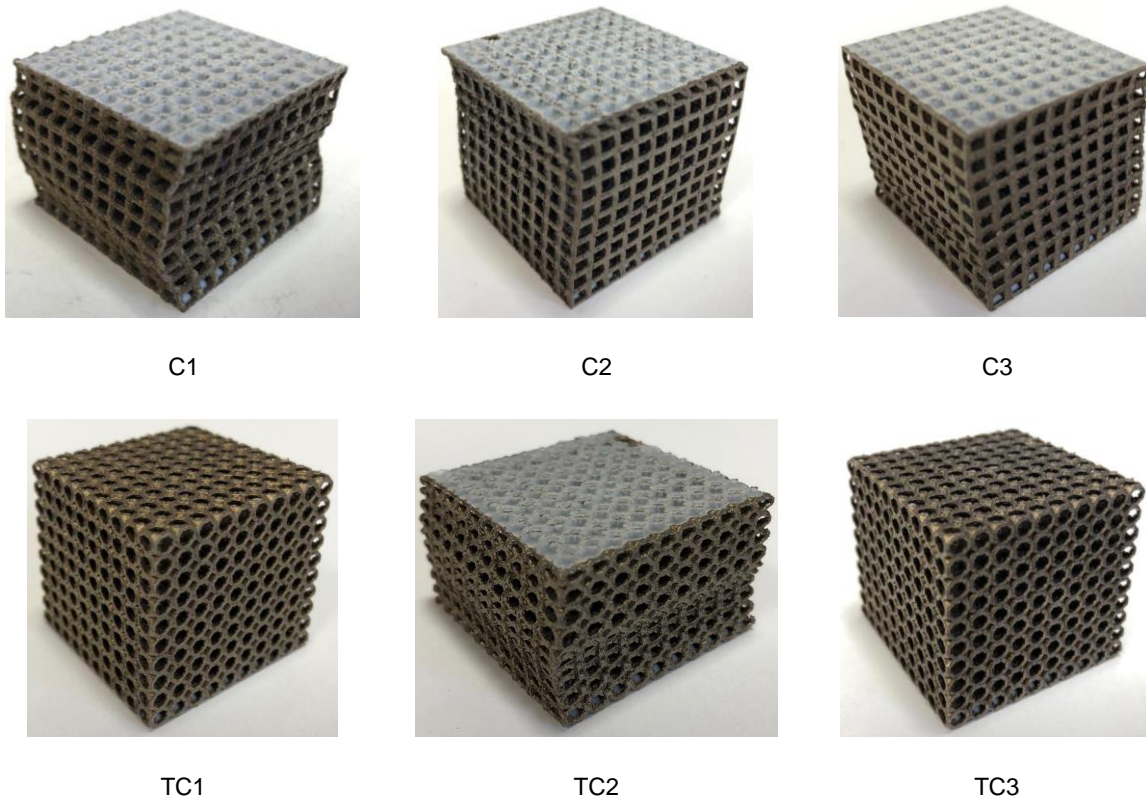


Figure 4.12 – Compression test specimens after being tested



The engineering stress-strain curves obtained for the specimens with the cubic topology and after being compensated for the elastic deformation of the pressing tool, are presented in Figure 4.13.

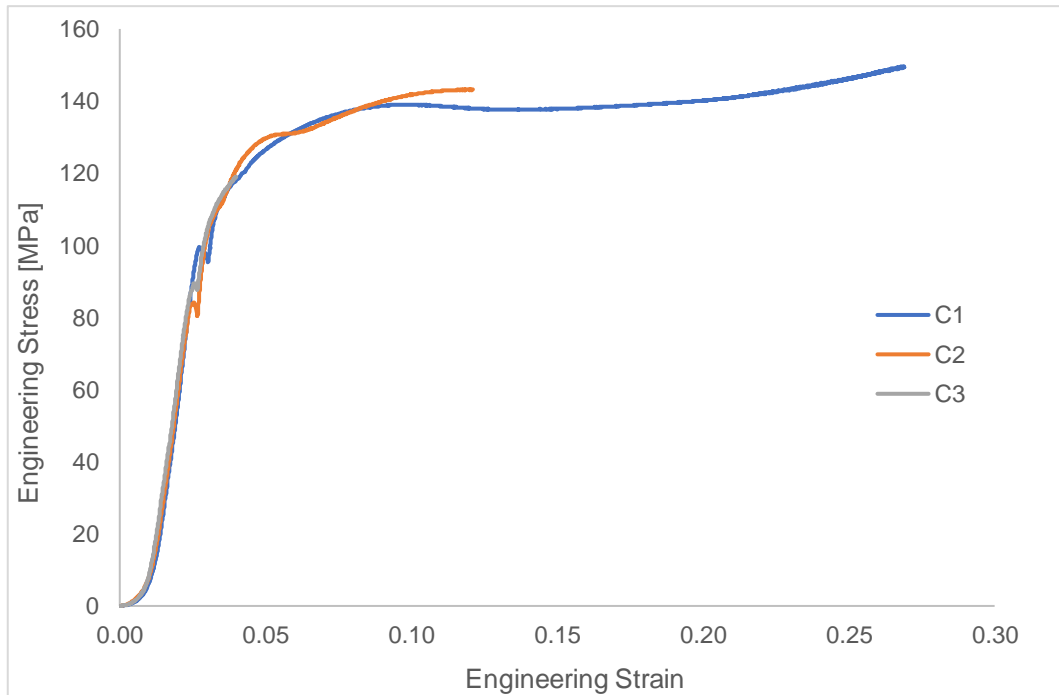


Figure 4.13 – Experimental results for the compression tests of the cubic (C) specimens

The engineering stress-strain curves obtained for the specimens with the truncated cube topology and after being compensated for the elastic deformation of the pressing tool, are presented in Figure 4.14.

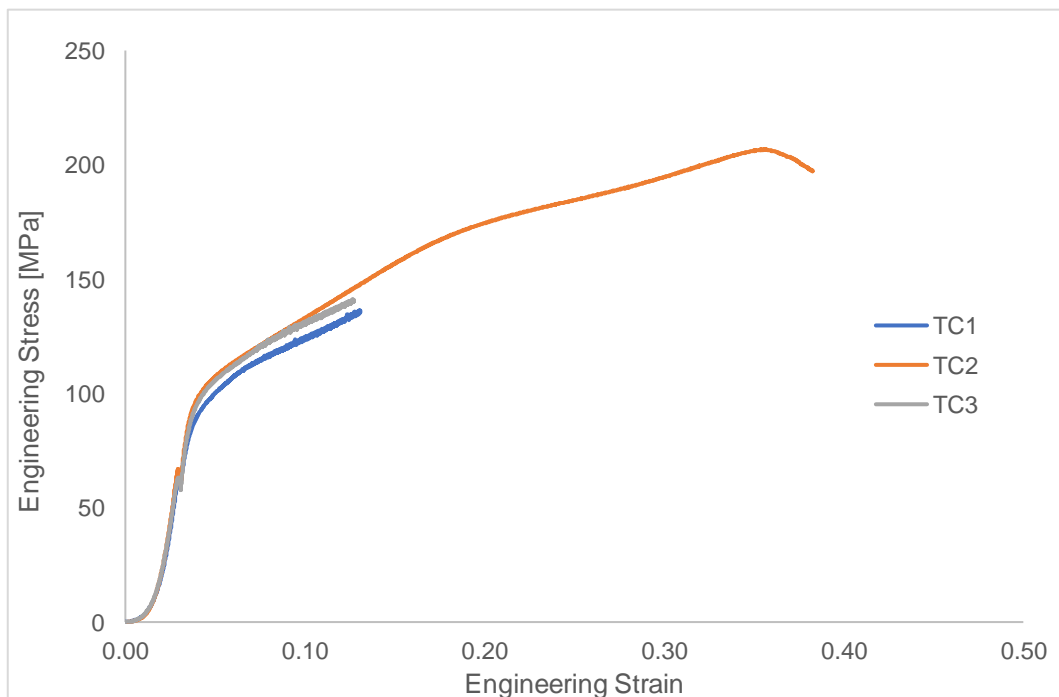


Figure 4.14 – Experimental results for the compression tests of the truncated cube (TC) specimens



From the inspection of both Figure 4.13 and Figure 4.14, it should be noted that for the same topology, the curves from the 3 specimens show a very good correlation. Besides, it can also be identified a discontinuity in the transition zone from elastic to plastic regime. This discontinuity may be due to the yield of some struts in the interior of the lattice, as it was not possible to identify in the exterior struts.

**4.3.3. Experimental and numerical assessment**

In order to validate the numerical models, new simulations were required since the material of which the specimens were made, 316 stainless steel, is different from the one used for the previous numerical simulations, pure iron.

The first numerical results were performed on coarser meshes than those previous selected in section 3.2, so that the computation solving times were lower, shown in Table 4.9.

Table 4.9 – Mesh characteristics and computation solving time for coarser meshes using 316 stainless steel, (\*) indicates solving times of simulations performed on the desktop PC

Topology	Element size [mm]	No. of elements	No. of nodes	Computation time
C-0.57	0.50	17850	34315	7min21s*
TC-0.50	0.50	149254	297933	17min32s*

In Figure 4.15, is shown the comparison between the results obtained for the coarser mesh of the C-0.57 lattice structure and the experimental results for the force-displacement curve of the C1 specimen. The curve from the numerical results was corrected in the displacement to match the experimental results on the elastic part.

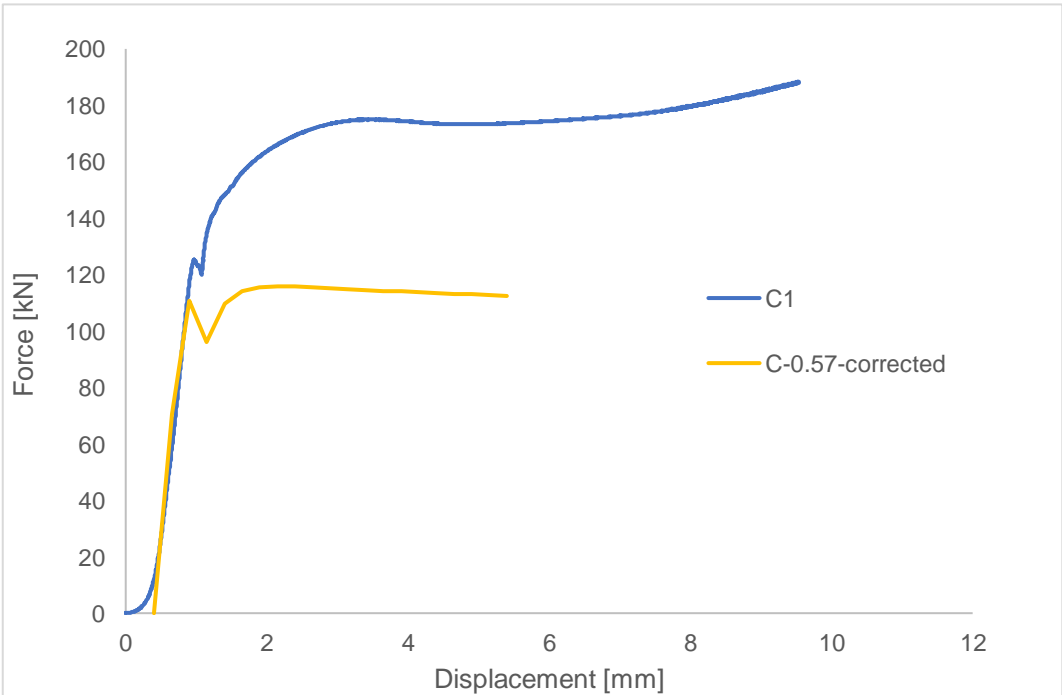


Figure 4.15 – Comparison between numerical and experimental results for the C-0.57 lattice structure

In Figure 4.16, is shown the comparison between the results obtained for the coarser mesh of the TC-0.50 lattice structure and the experimental results for the force-displacement curve of the TC1 specimen. The curve from the numerical results was corrected in the displacement to match the experimental results on the elastic part.

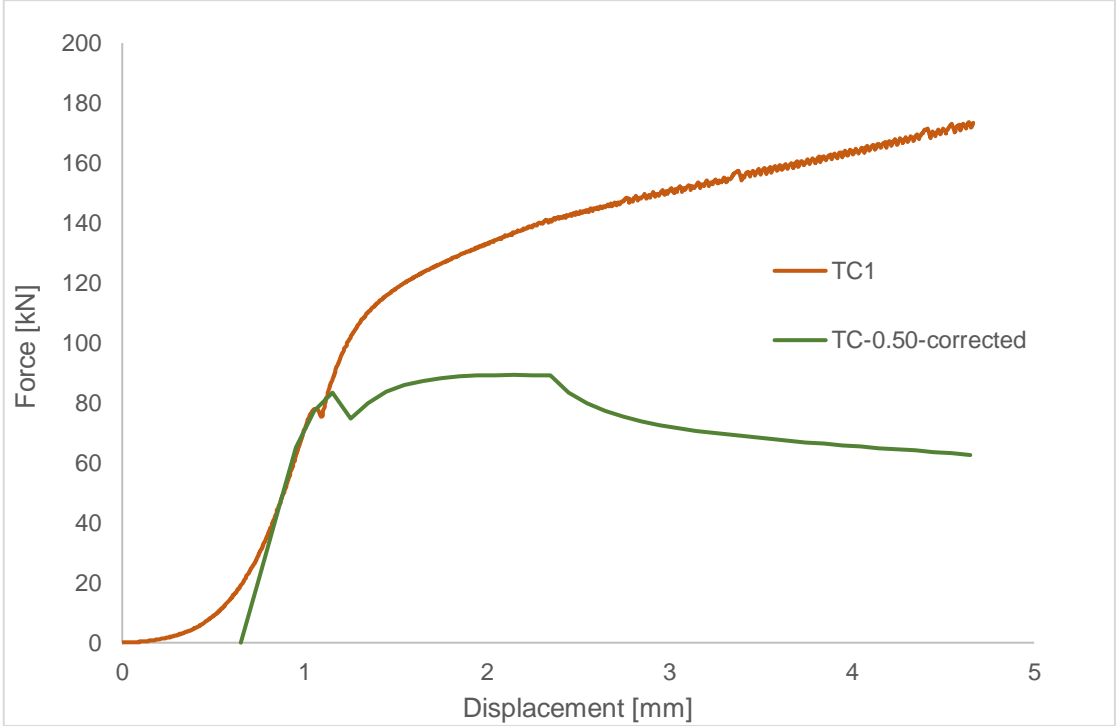


Figure 4.16 – Comparison between numerical and experimental results for the TC-0.50 lattice structure

From the inspection of both Figure 4.15 and Figure 4.16, one can see that the curves from the numerical simulations only show a good correlation in the elastic regime and beyond this point, they diverge significantly. The numerical results show that they can sustain much lower loads than the specimens that were tested.

One of the reasons for the lack of correlation in the plastic regime and the difference in the maximum load could be due to the fact that the dimensions of the specimens' struts were significantly larger than the lattice structures that were designed. For example, the C-0.57 was designed to have struts of 0.570 mm which resulted in struts of 1.140 mm when replicated in each direction, but the average value measured for the struts of these specimens was 1.409 mm – Figure 4.11 (c), due to the manufacturing process. These dimensions are closer to the C-0.70 lattice structure that was used in section 3.2.2 to perform the relative density analysis, which is designed to have struts of 0.700 mm, resulting in struts of 1.400 mm when replicated in each direction.

For this reason, numerical simulations were performed in this lattice structure, to evaluate its performance against the experimental results of the specimens, as it also corresponds to the topology that will take less computational solving time.

The first simulation was performed on a coarser mesh but, as it showed promising results, a refinement was made to match the element size of 0.3 mm, as previously selected in section 3.2.2 for this lattice structure.

Table 4.10 summarizes the characteristics of the meshes used to perform the FEA of the C-0.70 lattice structure.

Table 4.10 – C-0.70 mesh characteristics and computation solving time, (\*) indicates solving times of simulations performed on the desktop PC

C-0.70	Element size [mm]	No. of elements	No. of nodes	Computation time
Mesh 1	0.50	151498	299581	7min55s*
Mesh 2	0.30	890547	1501279	2h22min*

In Figure 4.17, is shown the comparison between the numerical results obtained for the Mesh 1 and Mesh 2 generated for the C-0.70 lattice structure with the experimental results for the force-displacement curve of the C1 specimen. Both curves from the numerical results were corrected in the displacement to match the experimental results on the elastic part.

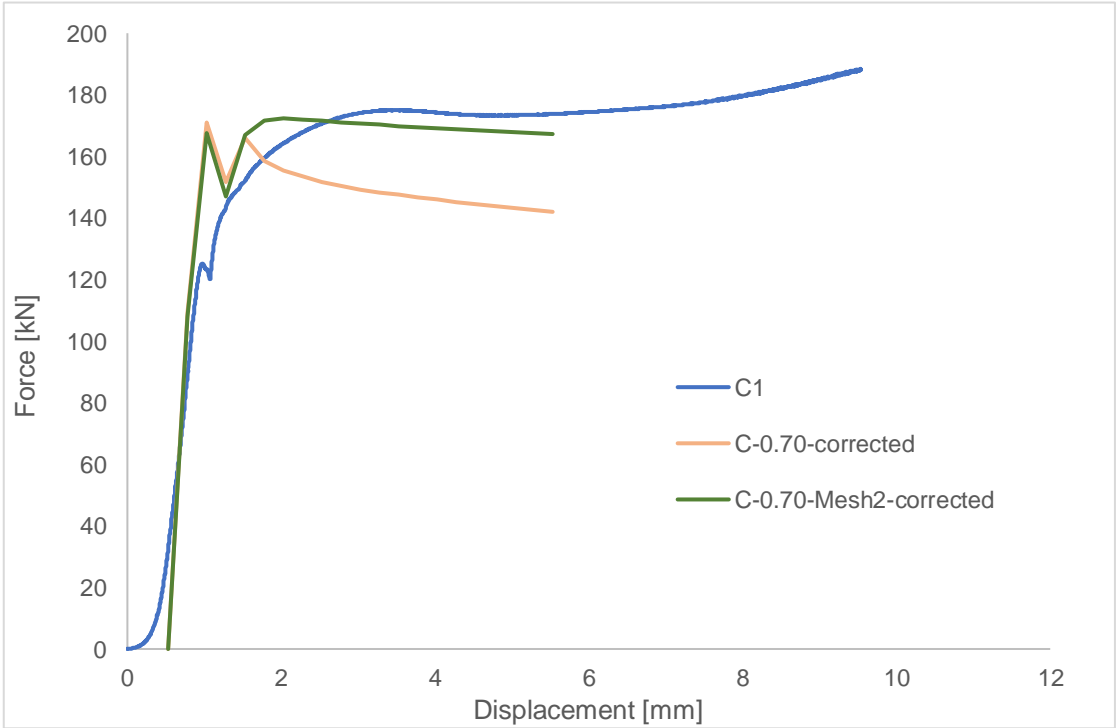


Figure 4.17 – Comparison between numerical and experimental results for the C-0.70 lattice structure

As can be seen from the inspection of Figure 4.17, the numerical results obtained for both meshes generated for the C-0.70 lattice structure showed a much better correlation to the experimental results when compared to the original designed C-0.57. The result obtained from refining the Mesh 1 and generating the Mesh 2, using the element size selected in section 3.2.2 for this topology, really brought the force-displacement numerical curve closer together to the experimental curve in the plastic regime, even replicating better its form.

There were other parameters that could have contributed to obtain a better correlation with the experimental results, such as increasing the number of increments in the numerical simulation, which were only 20, dividing to total displacement of 5 mm in increments of 0.25 mm and mechanically characterizing the stainless steel to obtain its true mechanical properties, instead of using the mechanical characteristics found in the literature [114].

It should also be noted that the average size of the strut obtained in section 4.3.1 only considered the external struts of the specimen, which may not be representative of the whole lattice structure. The structures should be cut open and the inside struts measured, to have a better overview of their dimensions, allowing to obtain a more accurate result for the average strut size.

Even though, taking into account all these limitations, the results obtained in the last analyses for the C-0.70 lattice structure allow concluding that the numerical models are validated.

Another thing to be noted is that the experimental stress-strain curves are very similar to those of bending dominated structures, as shown in Figure 2.6 (b), with a soft transition from the linear elastic regime to a long and flat plateau.

## 5. Conclusions and Further work

In this chapter, conclusions for this dissertation and further work perspectives are presented.

### 5.1. Conclusions

During the development of this dissertation, six open cell lattice structures were selected based on the previous work by Chantarapanich et al. [35], who chose them as the most suitable open cell unit cells for tissue engineering applications, out of 119 polyhedrons evaluated, and five of them were further explored, namely: cubic (C), truncated cube (TC), truncated octahedron (TO), rhombi-cuboctahedron (RCO) and rhombitruncated cuboctahedron (RTCO).

Numerical simulations were performed with the intention of finding the iron lattice structure with the mechanical properties closest to the trabecular bone. From the preliminary simulations of each topology, it was possible to conclude that:

- The type of element most suited to generate the several meshes is CTETRA10, which are tetrahedral elements with 10 nodes;
- A relative density of 25% was considered as the most suitable as it was the closest to the trabecular bone in terms of engineering stress-strain;
- The preliminary topology analysis performed on smaller scale lattices allowed to define the element size for the generation of the meshes for the full models. This element size was chosen based on the principle that the best balance between the convergence of both the effective stress on a given node and the reaction force at the base of the lattice;
- The simulation of only  $\frac{1}{4}$  of the full model by imposing symmetric constraints in the symmetry planes could achieve the same level of accuracy as simulating the full model, but on significantly much lower computational cost.

The numerical simulations of the full models, designed according to the International Standard ISO 13314:2011 [112], with meshes generated considering the previously determined element size for each topology, were successfully performed for the least complex topologies, C and TC. For the remaining topologies, TO, RCO and RTCO, even though the models were simplified by implementing symmetric constraints in the numerical model, it was not possible to obtain results for the previously determined element size, as it revealed to be too heavy for the computer to handle. For this reason, the results obtained for these topologies were obtained by extracting the results from the most refined mesh possible for each one of them.

The stress-strain engineering curves obtained from the simulations were plotted against the mechanical curves from the trabecular bone, at two different apparent densities. From this comparison, C and TC topologies were chosen as the best choice to perform the experimental tests, as not only were the most accurate results due to the element size being optimized, but also showed the most promising mechanical characteristics closer to the trabecular bone.

The numerical models were assessed experimentally by means of compression test of the C and TC topologies fabricated by L-PBF. The manufacturing of the specimens was performed in the

Portuguese company Erofió and they were manufactured in 316 stainless steel instead of iron, as initially pretended. Due to this fact, new simulations were required so that the numerical models could be assessed against the experimental results. The mechanical properties of the stainless steel were obtained from the literature [114] and the numerical simulations were performed.

When first examining the numerical results against the experimental data, there was almost no correlation beyond the elastic regime of the force-displacement curves, as the numerical models revealed to sustain a much lower load than the compression specimens. One of the reasons for this lack of correlation, was the dimensional variation between the designed lattice structures and the manufactured specimens, as the specimens had considerable larger struts than the ones designed, which could result in being able to sustain larger loads than the designed lattice.

To test this hypothesis, numerical simulations were performed on a lattice structure with the dimensions much closer to the average cubic specimen, the C-0.70. The numerical results obtained for this lattice structures revealed to be much closer to the experimental results. Even a refinement was performed to match the element size that had been selected in section 3.2.2 for this topology and the results improved more, with the shape of the curve being identical to the experimental results. This experimental – numerical assessment could be more improved if the mechanical properties of the material could be obtained experimentally and not from the literature.

Even though, taking into account the limitations mentioned above, the results obtained in the last analyses of the C-0.70 lattice structure may allow for the validation of the numerical models.

The work performed in this dissertation sets the ground basis for further investigation on the application of iron lattice structures fabricated by laser powder bed fusion (L-PBF) on biomedical implants. There is room for improvement, which we'll further be explored in the next section.

## **5.2. Further work**

As mentioned above, there is room for improvement on the work performed in this dissertation, starting with the fabrication of the specimens in the intended pure iron material. The fabrication of the lattice structures in iron would allow the experimental assessment of the numerical simulations performed in the first place. It could even make sense to mechanically characterize the material by fabricating specimens using the L-PBF process, as the mechanical properties of the specimens fabricated by fusing the powder material may very well be significantly different from the ones obtained by machining a rod of raw material.

Another area where there certainly is room for improvement is the optimization of the L-PBF process parameters for the material intended to be manufactured, in order to obtain specimens with dimensions closer to the ones designed.

As already mentioned, the measurements of the specimens' struts were only performed on the exterior struts, which may not be representative of the whole lattice structure. For this reason, some specimens should be cut open so that the interior struts would also be measured and a more accurate strut average size would be obtained.

The International Standard ISO 13314:2011 [112], on *Compression test for porous and cellular metals*, proposes cubic and cylinder specimens, but recommends the compression specimens to be cylindrical and to have a minimum of five specimens to be tested. So, as future work cylindrical compression specimens should be considered and a minimum of 5 specimens should be produced.

Lastly, there could be implemented some variations of the relative density in the specimens, to even better mimic the mechanical properties of the bone, as was done by Li et al [39].

It is in this way concluded that there is a considerable number of ways that could contribute to improve the numerical models developed in this dissertation, the manufacturing of the compression test specimens and also the experimental tests.

## References

- [1] Prasad A. State of art review on bioabsorbable polymeric scaffolds for bone tissue engineering. *Materials Today: Proceedings*. 2021;44:1391–1400.
- [2] Crotty M, Badley EM. An international comparison of the estimated effect of the aging of the population on the major cause of disablement, musculoskeletal disorders. *Journal of Rheumatology*. 1995;22:1934–1940.
- [3] Crowson CS, Matteson EL, III JMD, et al. Contribution of obesity to the rise in incidence of rheumatoid arthritis. *Arthritis Care & Research*. 2013;65:71–77.
- [4] Haines NM, Lack WD, Seymour RB, et al. Defining the Lower Limit of a “ Critical Bone Defect ” in Open Diaphyseal Tibial Fractures. *Journal of Orthopaedic Trauma*. 2016;30:158–163.
- [5] Roseti L, Parisi V, Petretta M, et al. Scaffolds for Bone Tissue Engineering : State of the art and new perspectives. *Materials Science & Engineering C*. 2017;78:1246–1262.
- [6] Bose S, Vahabzadeh S, Bandyopadhyay A. Bone tissue engineering using 3D printing. *Materials Today*. 2013;16:496–504.
- [7] Hermawan H. Updates on the research and development of absorbable metals for biomedical applications. *Progress in Biomaterials*. 2018;7:93–110.
- [8] Gorejová R, Haverová L, Orinakova R, et al. Recent advancements in Fe-based biodegradable materials for bone repair. *Journal of Materials Science*. 2019;54:1913–1947.
- [9] Arabnejad S, Johnston B, Tanzer M, et al. Fully Porous 3D Printed Titanium Femoral Stem to Reduce Stress-Shielding Following Total Hip Arthroplasty. *Journal of Orthopaedic Research*. 2017;35:1774–1783.
- [10] Tan XP, Tan YJ, Chow CSL, et al. Metallic powder-bed based 3D printing of cellular scaffolds for orthopaedic implants : A state-of-the-art review on manufacturing , topological design , mechanical properties and biocompatibility. *Materials Science & Engineering C*. 2017;76:1328–1343.
- [11] Yusop AH, Bakir AA, Shaharom NA, et al. Porous Biodegradable Metals for Hard Tissue Scaffolds : A Review. *International Journal of Biomaterials*. 2012;2012.
- [12] Sharma P, Pandey PM. Morphological and mechanical characterization of topologically ordered open cell porous iron foam fabricated using 3D printing and pressureless microwave sintering. *Materials and Design*. 2018;160:442–454.
- [13] Liverani E, Rogati G, Pagani S, et al. Mechanical interaction between additive-manufactured metal lattice structures and bone in compression: implications for stress shielding of orthopaedic implants. *Journal of the Mechanical Behavior of Biomedical Materials*. 2021;121:104608.
- [14] Kohn DH. 6.605 - Porous Coatings in Orthopedics. In: Ducheyne P, *Comprehensive Biomaterials*. Elsevier; 2011. p. 65–77.
- [15] Monteiro J. Design and Application of Lattice Structures on Sandwich Panels Core. Master Thesis. Instituto Superior Técnico; 2019.
- [16] Monteiro JG, Sardinha M, Alves F, et al. Evaluation of the effect of core lattice topology on the properties of sandwich panels produced by additive manufacturing. *Journal of Materials: Design and applications*. 2020;235:1312–1324.
- [17] Gibson LJ, Ashby MF. *Cellular Solids: Structure and Properties*. 2nd ed. Cambridge Solid State Science Series; 1997.
- [18] Ashby MF. The properties of foams and lattices. *Philosophical Transactions of the Royal Society A*. 2006;364:15–30.
- [19] Benedetti M, du Plessis A, Ritchie RO, et al. Architected cellular materials: A review on their mechanical properties towards fatigue-tolerant design and fabrication. *Materials Science and Engineering R: Reports*. 2021;144:100606.



- [20] Gibson LJ. Mechanical Behavior of Metallic Foams. *Annual Review of Materials Science*. 2000;30:191–227.
- [21] Gibson LJ. Lecture 3 - Structure of cellular solids [Internet]. [cited 2021 Sep 30]. Available from: <https://ocw.mit.edu/courses/materials-science-and-engineering/3-054-cellular-solids-structure-properties-and-applications-spring-2015/lecture-notes/>.
- [22] Maxwell JC. On the Calculation of the Equilibrium and Stiffness of Frames. *The London, Edinburgh, and Dublin Philosophical Magazine and Journal of Science*. 1864;27:294–299.
- [23] Wierzbicki T. Crushing analysis of metal honeycombs. *International Journal of Impact Engineering*. 1983;1:157–174.
- [24] Jinnapat A, Kennedy A. The Manufacture and Characterisation of Aluminium Foams Made by Investment Casting Using Dissolvable Spherical Sodium Chloride Bead Preforms. *Metals*. 2011;1:49–64.
- [25] Habib FN, Iovenitti P, Masood SH, et al. Fabrication of polymeric lattice structures for optimum energy absorption using Multi Jet Fusion technology. *Materials and Design*. 2018;155:86–98.
- [26] Leary M, Mazur M, Williams H, et al. Inconel 625 lattice structures manufactured by selective laser melting (SLM): Mechanical properties, deformation and failure modes. *Materials & Design*. 2018;157:179–199.
- [27] Kadkhodapour J, Montazerian H, Darabi AC, et al. Failure mechanisms of additively manufactured porous biomaterials: Effects of porosity and type of unit cell. *Journal of the Mechanical Behavior of Biomedical Materials*. 2015;50:180–191.
- [28] Abdulhadi HS, Mian A. Effect of strut length and orientation on elastic mechanical response of modified body-centered cubic lattice structures. *Proceedings of the Institution of Mechanical Engineers, Part L: Journal of Materials: Design and Applications*. 2019;233:2219–2233.
- [29] Xu Q, Czernuszka JT. Controlled release of amoxicillin from hydroxyapatite-coated poly (lactic-co-glycolic acid) microspheres. *Journal of Controlled Release*. 2008;127:146–153.
- [30] Mouriño V, Boccaccini AR. Bone tissue engineering therapeutics: controlled drug delivery in three-dimensional scaffolds. *Journal of The Royal Society Interface*. 2010;7:209–227.
- [31] Seitz H, Rieder W, Irsen S, et al. Three-Dimensional Printing of Porous Ceramic Scaffolds for Bone Tissue Engineering. *Journal of Biomedical Materials Research Part B: Applied Biomaterials*. 2005;74B:782–788.
- [32] Mauffrey C, Barlow BT, Smith W. Management of Segmental Bone Defects. *The Journal of the American Academy of Orthopaedic Surgeons*. 2015;23:143–153.
- [33] Dumas JE, Prieto EM, Zienkiewicz KJ, et al. Balancing the Rates of New Bone Formation and Polymer Degradation Enhances Healing of Weight-Bearing Allograft / Polyurethane Composites in Rabbit Femoral Defects. *Tissue Engineering Part A*. 2014;20:115–129.
- [34] Parthasarathy J. 3D modeling , custom implants and its future perspectives in craniofacial surgery. *Annals of Maxillofacial Surgery*. 2014;4:9–18.
- [35] Chantarapanich N, Puttawibul P, Sucharitpwatskul S, et al. Scaffold library for tissue engineering: A geometric evaluation. *Computational and Mathematical Methods in Medicine*. 2012;2012:1–14.
- [36] Agarwal R, García AJ. Biomaterial strategies for engineering implants for enhanced osseointegration and bone repair. *Advanced Drug Delivery Reviews*. 2015;94:53–62.
- [37] Gruskin E, Doll BA, Futrell FW, et al. Demineralized bone matrix in bone repair: History and use. *Advanced Drug Delivery Reviews*. 2012;64:1063–1077.
- [38] Alvarez K, Nakajima H. Metallic Scaffolds for Bone Regeneration. *Materials*. 2009;2:790–832.
- [39] Li Y, Jahr H, Pavanram P, et al. Additively manufactured functionally graded biodegradable porous iron. *Acta Biomaterialia*. 2019;96:646–661.

- [40] Marieb EN, Hoehn K. Human Anatomy Physiology. 11th ed. Pearson, United Kingdom; 2019.
- [41] Arshad R. Modelling of the inhomogeneities within the human intervertebral disc. Report No. 04-II-10. University of Stuttgart; 2004.
- [42] Mow VC, Hayes WC. Basic Orthopaedic Biomechanics. Raven Press; 1991.
- [43] Čapek J, Msallamová Š, Jablonská E, et al. A novel high-strength and highly corrosive biodegradable Fe-Pd alloy: Structural, mechanical and in vitro corrosion and cytotoxicity study. *Materials Science and Engineering C*. 2017;79:550–562.
- [44] Wang X, Xu S, Zhou S, et al. Topological design and additive manufacturing of porous metals for bone scaffolds and orthopaedic implants : A review. *Biomaterials*. 2016;83:127–141.
- [45] Li L, Yu F, Shi J, et al. In situ repair of bone and cartilage defects using 3D scanning and 3D printing. *Scientific Reports*. 2017;7:1–12.
- [46] Sumner DR. Long-term implant fixation and stress-shielding in total hip replacement. *Journal of Biomechanics*. 2015;48:797–800.
- [47] Shayesteh N, Mohsen M, Andani T, et al. Metals for bone implants: safety, design, and efficacy. *Biomanufacturing Reviews*. 2016;1.
- [48] Carluccio D, Xu C, Venezuela J, et al. Additively manufactured iron-manganese for biodegradable porous load-bearing bone scaffold applications. *Acta Biomaterialia*. 2020;103:346–360.
- [49] Wegener B, Sichler A, Milz S, et al. Development of a novel biodegradable porous iron-based implant for bone replacement. *Scientific Reports*. 2020;10:1–10.
- [50] Sheikh Z, Najeeb S, Khurshid Z, et al. Biodegradable Materials for Bone Repair and Tissue Engineering Applications. *materials*. 2015;8:5744–5794.
- [51] He J, Fang J, Wei P, et al. Cancellous bone-like porous Fe@Zn scaffolds with core-shell-structured skeletons for biodegradable bone implants. *Acta Biomaterialia*. 2021;121:665–681.
- [52] Williams DF. On the mechanisms of biocompatibility. *Biomaterials*. 2008;29:2941–2953.
- [53] Williams DF. There is no such thing as a biocompatible material. *Biomaterials*. 2014;35:10009–10014.
- [54] Koons GL, Diba M, Mikos AG. Materials design for bone-tissue engineering. *Nature Reviews Materials*. 2020;5:584–603.
- [55] Jin W, Chu PK. Orthopedic Implants. In: Narayan R, *Encyclopedia of Biomedical Engineering*. Elsevier; 2019. p. 425–439.
- [56] Kopp A, Derra T, Müther M, et al. Influence of design and postprocessing parameters on the degradation behavior and mechanical properties of additively manufactured magnesium scaffolds. *Acta Biomaterialia*. 2019;98:23–35.
- [57] Davachi SM, Kaffashi B. Polylactic Acid in Medicine. *Polymer-Plastics Technology and Materials*. 2015;59:72–82.
- [58] Chen Q, Thouas GA. Metallic implant biomaterials. *Materials Science & Engineering R*. 2015;87:1–57.
- [59] Yun Y, Dong Z, Lee N, et al. Revolutionizing biodegradable metals. *Materials Today*. 2009;12:22–32.
- [60] Li Y, Jahr H, Lietaert K, et al. Additively manufactured biodegradable porous iron. *Acta Biomaterialia*. 2018;77:380–393.
- [61] Basri H, Prakoso AT, Sulong MA, et al. Mechanical degradation model of porous magnesium scaffolds under dynamic immersion. 2019;0:1–11.
- [62] Santos C, Alves M, Montemor MF, et al. Bioresorbable metallic implants: surface

- functionalization with nanoparticles and nanostructures. In: Ahmad I, Sia P Di, Raza R, *Advanced Materials and their Applications: Micro to nano scale*. One Central Press; 2017.
- [63] Liu Y, Zheng Y, Chen X, et al. Fundamental Theory of Biodegradable Metals — Definition , Criteria , and Design. 2019;1805402:1–21.
- [64] Qin Y, Wen P, Guo H, et al. Additive manufacturing of biodegradable metals: Current research status and future perspectives. *Acta Biomaterialia*. 2019;98:3–22.
- [65] Zheng YF, Gu XN, Witte F. Biodegradable metals. 2014;77:1–34.
- [66] Buj-Corral I, Tejo-Otero A, Fenollosa-Artés F. Development of am technologies for metals in the sector of medical implants. *Metals*. 2020;10:686.
- [67] Elkaïam L, Hakimi O, Goldman J, et al. The Effect of Nd on Mechanical Properties and Corrosion Performance of Biodegradable Mg-5%Zn Alloy. *Metals*. 2018;8:438.
- [68] Cheng M, Wahafu T, Jiang G, et al. A novel open-porous magnesium scaffold with controllable microstructures and properties for bone regeneration. *Scientific Reports*. 2016;6:1–14.
- [69] Li H, Zheng Y, Qin L. Progress of biodegradable metals. *Progress in Natural Science: Materials International*. 2014;24:414–422.
- [70] Su Y, Cockerill I, Wang Y, et al. Zinc-Based Biomaterials for Regeneration and Therapy. *Trends in Biotechnology*. 2019;37:428–441.
- [71] Kim J, Oh S, Ki H. Effect of keyhole geometry and dynamics in zero-gap laser welding of zinc-coated steel sheets. *Journal of Materials Processing Tech*. 2016;232:131–141.
- [72] Salama MC, Rechená D, Reis L, et al. Effect of the topology on the mechanical properties of porous iron immersed in body fluids. *Proceedings of the Institution of Mechanical Engineers, Part L: Journal of Materials: Design and Applications*. 2021;235:1066–1076.
- [73] Liu B, Zheng YF. Effects of alloying elements (Mn, Co, Al, W, Sn, B, C and S) on biodegradability and in vitro biocompatibility of pure iron. *Acta Biomaterialia*. 2011;7:1407–1420.
- [74] Neves P. Finite element modelling of iron corrosion behavior. Master Thesis. Instituto Superior Técnico; 2021.
- [75] Roland Berger. Industry 4.0: The new industrial revolution, How Europe will succeed. THINK ACT. 2014;7–9.
- [76] Assunção E, Quintino L, Martina F, et al. LASIMM - AM production of large scale engineering structures. LASIMM project report.
- [77] ISO/ASTM 52900. Standard Terminology for Additive Manufacturing – General Principles – Terminology. ISO/ASTM International. 2015;1–9.
- [78] Martina F. Investigation of methods to manipulate geometry , microstructure and mechanical properties in titanium large scale Wire + Arc Additive Manufacturing. PhD Thesis. Cranfield University; 2014.
- [79] EPMA. Introduction to Additive Manufacturing Technology - A guide for Designers and Engineers [Internet]. 2019 [cited 2021 Sep 15]. Available from: <https://www.epma.com/epma-free-publications/product/introduction-to-additive-manufacturing-brochure>.
- [80] AMPOWER. Additive Manufacturing Market 2021 [Internet]. 2021 [cited 2021 Oct 12]. Available from: <https://additive-manufacturing-report.com/additive-manufacturing-market-2021/>.
- [81] Wohlers Associates. Wohlers Report 2017: 3D Printing and Additive Manufacturing State of the Industry [Internet]. 2017 [cited 2021 Sep 5]. Available from: <https://wohlersassociates.com/2017report.htm>.
- [82] Altıparmak SC, Xiao B. A market assessment of additive manufacturing potential for the aerospace industry. *Journal of Manufacturing Processes*. 2021;68:728–738.
- [83] Gibson I, Rosen DW, Stucker B. *Additive Manufacturing Technologies: Rapid Prototyping to*

Direct Digital Manufacturing. 1st ed. Springer; 2010.

- [84] Engineering Product Design. Additive manufacturing process steps [Internet]. [cited 2021 Oct 1]. Available from: <https://engineeringproductdesign.com/additive-manufacturing-process-steps/>.
- [85] mesago: formnext. The Additive Manufacturing process as a whole [Internet]. [cited 2021 Oct 12]. Available from: [https://formnext.mesago.com/frankfurt/en/themes-events/am-field-guide/process\\_in\\_general.html](https://formnext.mesago.com/frankfurt/en/themes-events/am-field-guide/process_in_general.html).
- [86] Hybrid Manufacturing Technologies. 7 families of 3D printing [Internet]. [cited 2021 Jun 16]. Available from: <https://hybridmanutech.com/resources/>.
- [87] ManufacturingGuide. Additive Manufacturing processes [Internet]. [cited 2021 Oct 23]. Available from: <https://www.manufacturingguide.com/en/additiv-tillverkning>.
- [88] Nazir A, Abate KM, Kumar A, et al. A state-of-the-art review on types, design, optimization, and additive manufacturing of cellular structures. *The International Journal of Advanced Manufacturing Technology*. 2019;104:3489–3510.
- [89] Sing SL, Miao Y, Wiria FE, et al. Manufacturability and mechanical testing considerations of metallic scaffolds fabricated using selective laser melting: a review. *Biomedical Science and Engineering*. 2016;2:18–24.
- [90] Gokuldoss PK, Kolla S, Eckert J. Additive Manufacturing Processes: Selective Laser Melting, Electron Beam Melting and Binder. *Materials*. 2017;10:672.
- [91] Körner C, Group F, Körner C. Additive manufacturing of metallic components by selective electron beam melting — a review. *International Materials Reviews*. 2016;61:361–377.
- [92] Poyraz Ö. Additive Manufacturing with Steels feedstock (excluding Stainless Steel) [Internet]. [cited 2021 Oct 21]. Available from: <https://www.epma.com/dm-industry-news/1051-cu027-lecture-05/file>.
- [93] Silbernagel C, Gargalis L, Ashcroft I, et al. Electrical resistivity of pure copper processed by medium-powered laser powder bed fusion additive manufacturing for use in electromagnetic applications. *Additive Manufacturing*. 2019;29.
- [94] Robinson JH, Robert I, Ashton T, et al. The effect of hatch angle rotation on parts manufactured using selective laser melting. *Rapid Prototyping Journal*. 2019;25:289–298.
- [95] Manfredi D, Calignano F, Krishnan M, et al. Additive Manufacturing of Al Alloys and Aluminium Matrix Composites (AMCs). In: Monteiro WA, Light Metal Alloys Applications. IntechOpen; 2014. p. 3–34.
- [96] Plocher J, Panesar A. Review on design and structural optimisation in additive manufacturing : Towards next-generation lightweight structures. *Materials & Design*. 2019;183.
- [97] Thijs L, Verhaeghe F, Craeghs T, et al. A study of the microstructural evolution during selective laser melting of Ti-6Al-4V. *Acta Materialia*. 2010;58:3303–3312.
- [98] Onuikie B, Bandyopadhyay A. Additive manufacturing in repair: Influence of processing parameters on properties of Inconel 718. *The International Journal of Advanced Manufacturing Technology*. 2019;103:1497–1507.
- [99] Jinoop AN, Paul CP, Bindra KS. Laser-assisted directed energy deposition of nickel super alloys: A review. *Proceedings of the Institution of Mechanical Engineers, Part L: Journal of Materials: Design and Applications*. 2019;233:2376–2400.
- [100] Qiu C, Yue S, Adkins NJE, et al. Influence of processing conditions on strut structure and compressive properties of cellular lattice structures fabricated by selective laser melting. *Materials Science & Engineering A*. 2015;628:188–197.
- [101] Fayazfar H, Salarian M, Rogalsky A, et al. A critical review of powder-based additive manufacturing of ferrous alloys: Process parameters, microstructure and mechanical properties. *Materials & Design*. 2018;144:98–128.

- [102] ManufacturingGuide. Hot Isostatic Pressure (HIP) [Internet]. [cited 2021 Oct 12]. Available from: <https://www.manufacturingguide.com/en/hot-isostatic-pressing-hip>.
- [103] Sing SL, An J, Yeong WY, et al. Laser and electron-beam powder-bed additive manufacturing of metallic implants: A review on processes, materials and designs. *Journal of Orthopaedic Research*. 2016;34:369–385.
- [104] Jardini AL, Larosa MA, Zavaglia C, et al. Customised titanium implant fabricated in additive manufacturing for craniomaxillofacial surgery. *Virtual and Physical Prototyping*. 2014;9:115–125.
- [105] Merkt S, Kleyer A, Hueber AJ. The Additive Manufacture of Patient-tailored Finger Implants - Feasibility study : implants based on XtremeCT technique. *Laser Technik Journal*. 2014;11:54–56.
- [106] Siemens Product Lifecycle Management Software Inc. NX Nastran: Handbook of Nonlinear Analysis (Solutions 106 and 129) [Internet]. 2014 [cited 2021 May 28]. Available from: [https://docs.plm.automation.siemens.com/data\\_services/resources/nxnastran/10/help/en\\_US/custom/nonlinear\\_106/nonlinear\\_106\\_NXN.pdf](https://docs.plm.automation.siemens.com/data_services/resources/nxnastran/10/help/en_US/custom/nonlinear_106/nonlinear_106_NXN.pdf).
- [107] Rodrigues J, Martins P. *Tecnologia Mecânica - Tecnologia da Deformação Plástica Vol I* (In Portuguese). 2nd ed. Escolar Editora, Portugal; 2010.
- [108] ASTM E8/E8M - 16a. Standard Test Methods for Tension Testing of Metallic Materials. *Annual Book of ASTM Standards*. 2016;1–30.
- [109] ASTM E9 – 19. Standard Test Methods of Compression Testing of Metallic Materials at Room Temperature. *Annual Book of ASTM Standards*. 2019;1–10.
- [110] Siemens Product Lifecycle Management Software Inc. Element Library Reference [Internet]. 2014 [cited 2021 May 20]. Available from: [https://docs.plm.automation.siemens.com/data\\_services/resources/nxnastran/10/help/en\\_US/docExt/pdf/element.pdf](https://docs.plm.automation.siemens.com/data_services/resources/nxnastran/10/help/en_US/docExt/pdf/element.pdf).
- [111] Bäker M. How to get meaningful and correct results from your finite element model. *Technische Universität Braunschweig*; 2018.
- [112] ISO 13314. Mechanical testing of metals – Ductility testing – Compression test for porous and cellular metals. *International Organization for Standardization*. 2011;1–7.
- [113] GE Additive. Concept Laser X Line 2000R [Internet]. 2021 [cited 2021 Oct 19]. Available from: <https://www.ge.com/additive/additive-manufacturing/machines/x-line-2000r>.
- [114] Kweon H Do, Kim JW, Song O, et al. Determination of true stress-strain curve of type 304 and 316 stainless steels using a typical tensile test and finite element analysis. *Nuclear Engineering and Technology*. 2021;53:647–656.
- [115] Math.net. Planes of symmetry in a cube [Internet]. [cited 2021 Oct 30]. Available from: <https://www.math.net/plane-symmetry>.

### Appendix A – Correction of the force-displacement experimental curves

The force-displacement curve of the dry-run test is presented in Figure A.1, along with the trend line function and the coefficient of determination,  $R^2$ , of this plot.

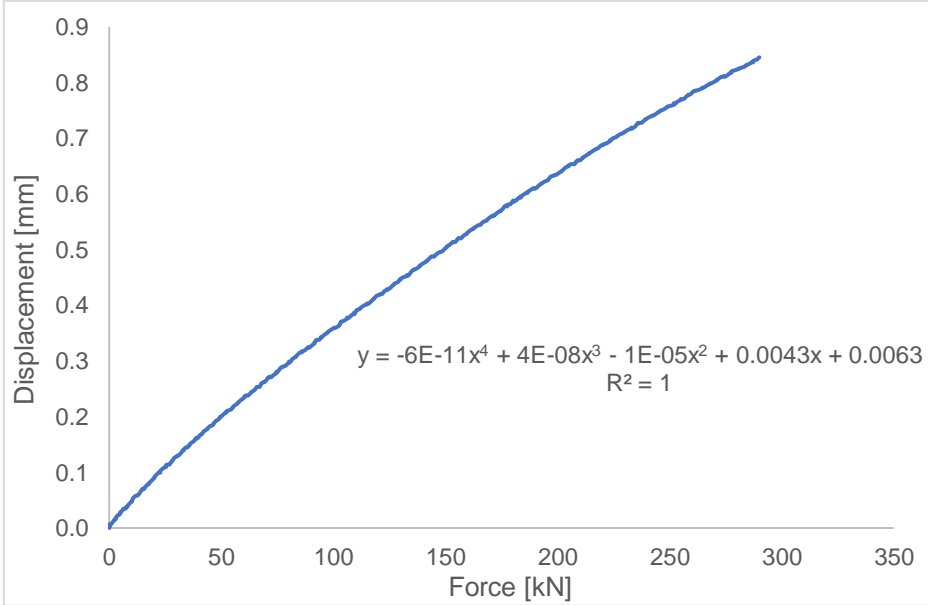


Figure A.1 – Displacement-force curve of the dry-run test

Using the trend line function, a correction factor for the displacement values is computed through the force values, and after the displacement value and the correction factor are added, the result is the true displacement value. Figure A.2 shows how the elastic recovery of the shaft influences the true displacement of the specimens and the resulting force-displacement curve.

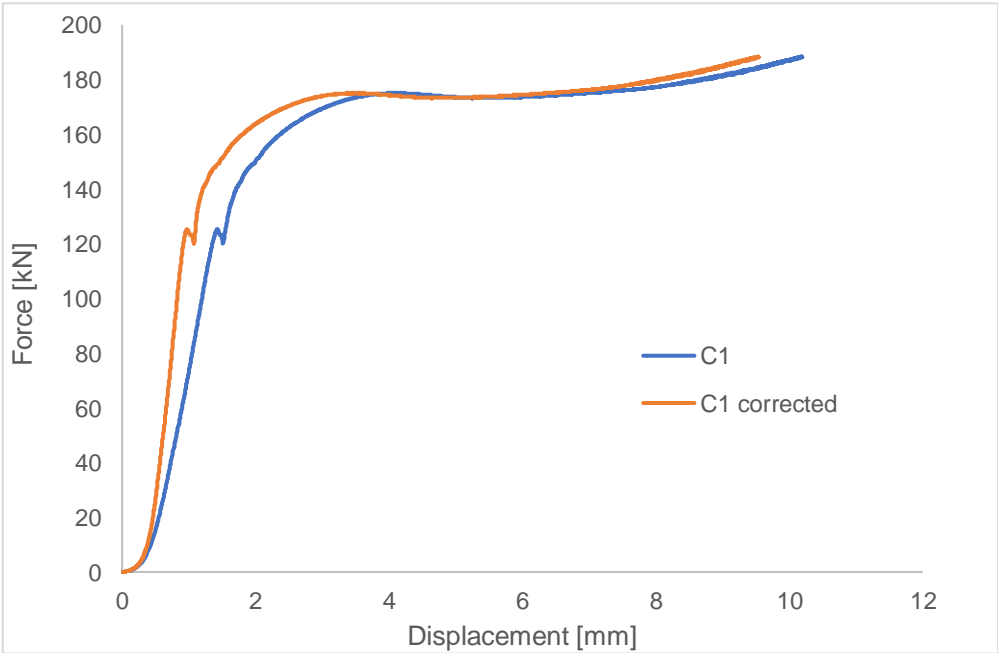


Figure A.2 – Force-displacement curve for specimen C1, with and without the correction of the displacement